# Mechanistic modelling of gross primary production from sun-induced fluorescence measurements on a wheat canopy in Belgium

**Auteur :** Pezzetti, Natacha
**Promoteur(s) :** Longdoz, Bernard; Beauclaire, Quentin
**Faculté :** Gembloux Agro-Bio Tech (GxABT)
**Diplôme :** Master en bioingénieur : sciences et technologies de l'environnement, à finalité spécialisée
**Année académique :** 2021-2022
**URI/URL :** http://hdl.handle.net/2268.2/15704

LIÈGE université
Gembloux
Agro-Bio Tech

# Mechanistic modelling of gross primary production from sun-induced fluorescence measurements on a wheat canopy in Belgium

NATACHA PEZZETTI

Thesis submitted for the degree of Master in Bioengineer specialised in Environmental Sciences and Technologies

ACADEMIC YEAR 2021-2022

CO-PROMOTERS: Pr. Bernard LONGDOZ & Quentin BEAUCLAIRE

LIÈGE université
Gembloux
Agro-Bio Tech

# Mechanistic modelling of gross primary production from sun-induced fluorescence measurements on a wheat canopy in Belgium

NATACHA PEZZETTI

Thesis submitted for the degree of Master in Bioengineer specialised in Environmental Sciences and Technologies

ACADEMIC YEAR 2021-2022

CO-PROMOTERS: Pr. Bernard LONGDOZ & Quentin BEAUCLAIRE

This present master thesis has been conducted within the Biosystems Dynamics and Exchanges (BIODYNE) department of Gembloux Agro-Bio Tech (Liège University).


## Acknowlegdments

First of all, I would like to thank Quentin Beauclaire, PhD student in the BIODYNE department, for his valuable contribution to this work, for his availability, his advice and for sharing his experience as a scientific researcher. I would like to thank Professor Bernard Longdoz for his wise observations and advice. I would particularly like to thank Le Thien Kim Marie Hoang, classmate and friend, and Laura Delhez, PhD student in the BIODYNE department, for sharing their data on plant biomass. Finally, I would like to thank my brother David, for his advice and help, and my family and friends for their support.

## Abstract

In the context of global climate change, extreme weather events are expected to intensify, threatening agricultural systems. Meanwhile, food demand is likely to grow due to increasing human population. Accordingly, being able to assess and predict dynamic behaviours of crops under changing climatic conditions is crucial to ensure food security. For that purpose, photosynthesis is the key process to characterise. According to the literature, sun-induced fluorescence (SIF) represents a potential indicator of photosynthesis. Recently, the mechanistic light response model (MLR) estimating gross primary production (GPP) from SIF has been established. Firstly, this study aims to assess the relationship between SIF and GPP from the MLR model perspective for a winter wheat canopy in Belgium. Secondly, the dynamics of the main model parameters depending on environmental conditions have been studied. Continuous measurements of micro-meteorological, flux and SIF data have been carried out for five months by an ICOS station. Moreover, leaf-level gas exchange and fluorescence parameters have been measured manually using a portable photosynthesis system. Similar temporal evolutions of SIF and GPP in response to light have been observed, supporting the use of SIF as an indicator of photosynthesis. The model provides a relatively moderate performance at half-hourly scale which improved at daily scale. In particular, the model seems to correctly reproduce the SIF-GPP relationship only under low light intensities and high soil moisture which is in agreement with the main model assumption. Overall, these results point out the need for more accurate characterization of the model underlying processes and parameters dynamics regarding environmental conditions.


**Keywords.** Photosynthesis, Sun-Induced Fluorescence, Gross Primary Production, Winter Wheat, Edaphic Drought.



## Résumé

Dans un contexte de changement climatique mondial, on s'attend à ce que les phénomènes météorologiques extrêmes s'intensifient, ce qui représente une menace pour les systèmes agricoles. Parallèlement, la demande alimentaire devrait augmenter en raison de l'accroissement de la population humaine. Par conséquent, il est crucial de pouvoir évaluer et prédire les comportements dynamiques des cultures dans des conditions climatiques changeantes pour garantir la sécurité alimentaire. À cette fin, la photosynthèse est le processus clé à caractériser. Selon la littérature, la fluorescence induite par le soleil (SIF) représente un indicateur potentiel de la photosynthèse. Récemment, le modèle mécaniste de réponse à la lumière (MLR) estimant la production primaire brute (GPP) à partir de la SIF a été établi. Premièrement, cette étude vise à évaluer la relation entre SIF et GPP du point de vue du modèle MLR pour une culture de blé d'hiver en Belgique. Deuxièmement, la dynamique des principaux paramètres du modèle en fonction des conditions environnementales a été étudiée. Des mesures continues de données micro-météorologiques, de flux et de SIF ont été effectuées pendant cinq mois par une station ICOS. De plus, les paramètres d'échange gazeux et de fluorescence à l'échelle de la feuille ont été mesurés manuellement à l'aide d'un système de mesure de la photosynthèse portatif. Des évolutions temporelles similaires de SIF et GPP en réponse à la lumière ont été observées, ce qui soutient l'utilisation de la SIF comme indicateur de la photosynthèse. Le modèle fourni une performance relativement modérée à l'échelle de la demi-heure et une performance meilleure à l'échelle journalière. En particulier, le modèle semble reproduire correctement la relation entre SIF et GPP uniquement sous de faibles intensités lumineuses et une humidité du sol élevée, ce qui est en accord avec l'hypothèse principale du modèle. Globalement, ces résultats soulignent la nécessité d'une caractérisation plus précise des processus sous-jacents du modèle et de la dynamique des paramètres en fonction des conditions environnementales.


**Mots-clés.** Photosynthèse, Fluorescence Induite par le Soleil, Production Primaire Brute, Blé d'Hiver, Sécheresse Édaphique.

# Contents

# List of Figures

# List of Tables

## Preface : student contribution

I carried out the bibliographical research for the understanding of the subject and the interpretation of the results and I implemented the model used in this study with the Python computer language. I interpreted and analysed the results. Quentin Beauclaire collaborated considerably with me on the overall understanding of the subject, the analysis of the data and the interpretation of the results through our multiple interactions. He also carried out all the manual measurements in Lonzée, twice a week from April to June 2022. The solar-induced fluorescence measurements were performed and processed by Simon De Cannière, PhD student at the Catholic University of Leuven. The micro-meteorological data were collected and processed by the ICOS team and the technicians of the BIODYNE department. Finally, the biomass data were collected and processed by Le Thien Kim Marie Hoang and Laura Delhez, respectively Master and PhD student at Gembloux Agro-Bio Tech.

# Chapter 1

# Introduction

## 1.1 Contextualisation

Nowadays, there is no doubt that human activities have caused an unprecedented increase in greenhouse gases concentration since the Industrial revolution, increasing the global surface temperature. As a result, the atmosphere as well as lands and oceans have warmed up in the last decades. The impacts of these climate changes are already visible in many regions of the world and are susceptible to get worse in future decades. Under those circumstances, it is expected that extremes weather events will be more frequent and intense. Indeed, heavier precipitation events are predicted by models across northern America and Europe as well as longer and more intense drought events (Fischer and Knutti, 2015). These changes represent a serious threat to agricultural systems, and thus to food security overall, with complex and varying effects across regions and time (Schmidhuber and Tubiello, 2007; FAO, 2021). Moreover, the worldwide human population is expected to increase to over 9 billion by 2050, especially in the developing countries. Therefore, the food demand will grow, leading to a need for more efficient production if the current type of diet is maintained, especially for cereal crops which represent a large part of human food production (FORUM, 2009; United Nations Department of Economic and Social Affairs, 2022). More precisely, the Food and Agriculture Organization of the United Nations (FAO) predicts that the overall food production must increase by 70 % by 2050 to respond efficiently to the growing food demand (FORUM, 2009; United Nations Department of Economic and Social Affairs, 2022). Being able to grow local crops, such as winter wheat, and understand their behaviour under a large range of environmental conditions is therefore crucial, especially since climate events will generate great variations in local crop yield and food supplies (Schmidhuber and Tubiello, 2007).

To ensure food security and provide steady local and global food supplies, dynamic behaviours of croplands linked to water cycle, carbon cycle and nutrient cycles under changing climatic conditions must be assessed, understood and predicted. To reach this goal, it is essential to accurately describe the process of photosynthesis, by which plants use solar energy and carbon dioxide ($CO_2$) to synthesise photoassimilates. At large space scales, the photosynthesis corresponds to the carbon exchanges between the biosphere and the atmosphere. Since the impacts of global warming on the overall carbon sink are still partially unknown, it is all the more important to be able to characterise photosynthesis under changing climatic conditions (Hall and Rao, 1999; Rogers et al., 2017; Porcar-Castell et al., 2021). This is thus the key process studied in this study by the way of the transfer of carbon from the atmosphere to cropland plants. Because it is the combination of diverse factors and reactions, it is crucial to understand which ones are the most sensitive to the upcoming climate events in order to prevent their potential impacts on crop production.

Besides, this study focuses on winter wheat. In temperate regions, this is a dominant cultivated crop that provides food for human and livestock consumption (Shewry, 2009). For instance, in 2020 in Belgium, the cultivated area for winter wheat accounted for 60 % of the total cultivated area for cereal grain crops and in 2021, this number increased by 6.2 % (Statbel, 2022). Moreover, winter wheat production is expected to increase in the future by 1.5 % each year (FAO, 2022). Consequently, it is crucial to understand and predict the impacts of climate change on such crop yields.

## 1.2 Photosynthesis and related processes

The reactions that make up the process of photosynthesis are divided into two major groups: the light and the dark reactions (Porcar-Castell et al., 2014). First, the light reactions occur during daytime (Taiz et al., 2015). They consist of the absorption of light energy leading to the synthesis of energy-carrying molecules. Those are ATP (adenosine triphosphate) and NADPH (nicotinamide adenine dinucleotide phosphate) which will be used afterwards as inputs

into the dark reactions, occurring during both daytime and nighttime. Specifically, they are reassembled in the Calvin cycle which reduces carbon dioxide to photoassimilates (Porcar-Castell et al., 2014; Jonard et al., 2020). The absorption of light is achieved by chlorophyll molecules, located in leaf cells. Their absorption spectrum ranges from 400 and 700 nm, known as the photosynthetically active radiation (PAR). These pigment molecules are reassembled as what is called "light harvesting complex" and are linked to proteins named photosystems. In particular, there are two photosystems controlling photosynthesis, namely PSI and PSII (Porcar-Castell et al., 2014; Taiz et al., 2015). Photosystems contain reaction centers which collect the excited energy and provide it to chemical reactions (Taiz et al., 2015). Finally, two types of photosynthesis exist among plants. In the case of wheat, their photosynthesis is characterised as "C3" which means that the first carbohydrate synthesising contains three atoms of carbon compared to photosynthesis "C4" where this sugar contains four atoms of carbon (Moene and Dam, 2014).

Climate changes and the related extreme events are to provoke many perturbations within the photosynthesis processes whose effects are still unclear. First, the rise of temperature can have multiple and contradictory effects. On one hand, high leaf temperature is likely to limit plant growth and thus crop yield. On the other hand, when there are no limitations in water supply, plants are able to adapt their growth functions to high temperatures, especially C3 species. Hence, the yield of photosynthesis can be favored, except if temperature reaches extreme values above the optimum for photosynthesis which is for now not the case (Sage and Kubien, 2007; Yamori et al., 2014). Secondly, under high temperature, aridity is predicted to increase and drought events might become more pronounced, leading to a strong limitation of plant growth and a lowering of photosynthetic rates (Ahmad, 2016; Fakhet et al., 2021). Then, regarding the increasing atmospheric $CO_2$ concentration, the photosynthesis of C3 plants is more likely to be stimulated. Nonetheless, the impacts of rising temperatures on plant metabolism are expected to feed back on carbon processes. Overall, those combined effects on C3 plants remain unclear (Kirschbaum, 2004; Taiz et al., 2015; Dusenge et al., 2019). As a consequence, predicting how abiotic factors affect photosynthesis in a climate change context is critical. Fluorescence is one of the methods which can be used to understand how these impacts are induced.

### 1.2.1 Link between Photosynthesis and Fluorescence

#### Theoretical background

After absorbing a light particle, the pigment molecule is said to be "excited" (Baker, 2008; Taiz et al., 2015; Gu et al., 2019). In this state, the chlorophyll is highly unstable and will directly lose some energy in the form of heat. From this point, the remaining excitation energy can be dissipated in three modes through molecular interactions. This is the concept of "quenching" leading to the de-excitation of the chlorophyll molecule (Kasajima et al., 2009; Taiz et al., 2015). The first one, called photochemical quenching (PQ), uses most of the incoming radiation to fuel chemical reactions (Porcar-Castell et al., 2014; Frankenberg and Berry, 2017; Jonard et al., 2020; Taiz et al., 2015). More precisely, this amount of energy will generate an electron transport taking place from PSII to PSI, contributing to the synthesis of ATP and NADPH (Baker, 2008; Porcar-Castell et al., 2014; Gu et al., 2019). In fact, this electron transport represents an instantaneous and a quantifiable link between the light and the dark reactions (Gu et al., 2019). The second quenching consists in the dissipation of the excitation energy in the form of heat by different physiological processes, of which mainly are gathered under the term non-photochemical quenching, or regulated disspation (NPQ). This is the predominant defense mechanism utilised by plants to prevent damage to the photosynthetic machinery when the radiation absorbed is very important (Yamori et al., 2014; Yamamoto et al., 1999; Meroni et al., 2009; Porcar-Castell et al., 2014; Mohammed et al., 2019; Jonard et al., 2020). Next, there is a dissipation of energy through the emission of chlorophyll-$\alpha$ fluorescence (ChlF), which

means that a part of the energy initially absorbed is reemitted as light. Its emission wavelength ranges from 640 to 850 nm, which corresponds to the red and far-red part of the spectrum, with two peaks reaching approximately 685 and 740 nm (Aasen et al., 2019; Gu et al., 2019; Jonard et al., 2020; Liu et al., 2022). These main three possible modes of excitation energy quenching are in direct competition (Meroni et al., 2009; Gu et al., 2019). That is to say that if the rate of one of them changes, then the rate of the two other processes will be inversely impacted (Baker, 2008; Cendrero-Mateo et al., 2015). For this reason, fluorescence is quantitatively connected to photosynthesis and thus is an interesting proxy to estimate it as it, as pointed out by many studies (Baker, 2008; Meroni et al., 2009; Frankenberg and Berry, 2017; Gu et al., 2019; Li et al., 2020; Porcar-Castell et al., 2014). In reality, models estimating photosynthesis from fluorescence had already been established in the past (Li et al., 2020; Porcar-Castell et al., 2021).

Over the last decades, there has been rapid development of fluorescence measurement methods through different spatial and temporal scales (Aasen et al., 2019; Jonard et al., 2020; Li et al., 2020; Porcar-Castell et al., 2021). Thereupon, concrete improvements in understanding and predicting photosynthesis dynamics have been achieved (Aasen et al., 2019; Gu et al., 2019). Currently, two main methods of measurement exist, each using a different light source to stimulate pigment molecules. The first one uses artificial light and is thus characterised as "active", such as the leaf-level pulse-modulated (PAM) fluorescence. It allows the study of photosynthesis at the leaf level *in situ* as artificial light cannot be used at large scales (Goulas et al., 2017; Aasen et al., 2019; Porcar-Castell et al., 2021). In contrast, the second method uses natural light, sunlight, and is thus called "passive" method (Gu et al., 2019; Jonard et al., 2020; Porcar-Castell et al., 2021). Concerning the latter, commonly referred to as "Sun-induced fluorescence" (SIF), it has been shown to be a good indicator, not only of photosynthesis across different spatial scales, but also of transpiration and ecosystem productivity in general, even though its measurement still contains a lot of unknowns (Jonard et al., 2020; Li et al., 2020; Feng et al., 2021). Likewise, it represents an interesting tool to detect plant stress at large time and spatial scales (Damm et al., 2010). Indeed, it can be used to predict drought events effects on photosynthesis at the first stages of stress, better than common vegetation indices that are not directly linked to the plant photosynthesis functioning (Zhang et al., 2016; Jonard et al., 2020; Shen et al., 2022). As shown by many studies, during the last two decades, various SIF sensors have been used on towers, satellites or aircrafts with resolutions from the leaf to the landscape level (Zhang et al., 2016; Jonard et al., 2020; Porcar-Castell et al., 2021). Regarding remote sensing instruments, their spatial resolution is becoming higher and many protocols have been standardised (Aasen et al., 2019).

Since the fluorescence signal is added to the global reflected spectra of the vegetation, different methods exist to retrieve SIF from the background reflected radiation. The main ones are the Fraunhofer line depth method (FLD) and the Spectral fitting methods (SFMs). Broadly speaking, the sensor scans some areas of the solar spectrum (Fraunhofer lines) and/or the Earth's atmosphere (telluric lines), in which the solar irradiance is attenuated due to the absorption by gas. The main bands used are the oxygen A and B bands, with maximum absorption at respectively 760 and 687 nm. Those are "filled" with fluorescence radiation emitted by leaves at similar wavelengths. As a matter of fact, there is an amplification of the fluorescence signal within these lines (Moya et al., 2004; Porcar-Castell et al., 2014; Frankenberg and Berry, 2017; Aasen et al., 2019; Mohammed et al., 2019).

From space, records have been performed with devices initially used to measure atmospheric gases, which makes them not optimal (Jonard et al., 2020; Porcar-Castell et al., 2021). Now, there also exists tropospheric instruments to monitor SIF with high spatial and temporal resolutions (Li and Xiao, 2022). As an illustration, the first satellite mission that will specifically focus on SIF monitoring, called the *Fluorescence Explorer (FLEX) mission*, will be launched in 2024 by the European Space Agency and will provide spatially continuous SIF data (Moreno et al., 2006; Jonard et al., 2020; Porcar-Castell et al., 2021).

**Modelling photosynthesis from fluorescence**

An important concept derived from photosynthesis, commonly used in studies, is the gross primary production (GPP). It represents the part of the carbon biomass produced by plants that is not used for respiration per unit of time. In other words, it accounts for the rate of uptake of atmospheric $CO_2$ by plants to fuel photosynthesis. Generally speaking, it characterises the largest carbon flux from the atmosphere to terrestrial ecosystems (Beer et al., 2010; Zhang et al., 2016; Gu et al., 2019).

Gross primary production is commonly estimated from $CO_2$ flux measurements performed at the atmosphere-ecosystem interface (on a flux tower), by using the Eddy-covariance (EC) technique (Aubinet et al., 2012). Typically, a common method used to estimate GPP from SIF measurements is to perform statistical regressions between tower-based GPP and remote-sensed SIF for diverse plant types or ecosystems as similar patterns between GPP from SIF and tower-based GPP are observed (Gu et al., 2019). Afterwards, the regressions are used to estimate GPP at large scales from SIF satellite measurements (Liu et al., 2022). Although this method relies on significant relationships between the two variables of interest, its robustness in terms of physiological interpretation can be questioned, because it is not always supported by physiological and structural explanations (Liu et al., 2022). The validity of these relationships is then questionable when ecosystem or environmental conditions are not in the exact scope of the measurements on which they are based. Moreover, the measurements of photosynthetic $CO_2$ assimilation from the EC method at the plot level represent only a part of the spatial information that SIF imaging methods can better provide (Porcar-Castell et al., 2021). Consequently, estimating GPP directly from a mechanistic relationship from SIF measurements seems to be an alternative at large scale since it is directly linked to photosynthesis processes intensity.

Models describing light and dark reactions have existed for decades. However, the ones pertaining dark reactions are more detailed and documented, such as the Farquhar, von Caemmerer and Berry (FvCB) model (Farquhar et al., 1980; Gu et al., 2019). This robust mechanistic model is largely used to estimate gross primary production in terrestrial biosphere models (TBMs) for C3 and C4 species (Rogers et al., 2017). Furthermore, with respect to dark reactions, the light use efficiency (LUE) model is traditionally used to determine GPP from remote sensing data, such as the incoming photosynthetically active radiation (PAR), considering GPP proportional to the efficiency at which the absorbed radiation is used in photosynthesis processes (Porcar-Castell et al., 2014; Gonsamo and Chen, 2018; Liang and Wang, 2020). Because the emission of fluorescence is competing for the same excitation energy as photosynthesis, SIF can be related to the LUE concept and even combined with this model to estimate GPP (Damm et al., 2010; Guanter et al., 2014; Porcar-Castell et al., 2014; Yang et al., 2015; Guanter et al., 2014). However, LUE is a concept which simplifies photosynthesis by relying on different assumptions (Liang and Wang, 2020). In reality, it is composed of complex processes varying with environmental conditions. These underlying mechanisms are for a large part still unknown and the variations were usually taken into account by the use of empirical functions (Frankenberg and Berry, 2017; Gu et al., 2019). Besides, it is important to note that this empirical model only represents the potential amount of photosynthesis performed by the plants Chen et al. (2021b). Indeed, it can lead to underestimations of the vegetation productivity at large scales, or overestimations at low levels of incoming PAR (Turner et al., 2003; Liang and Wang, 2020).

In the last few years, new models have been developed, notably with regards to light reactions. By contrast with empirical models, these new ones are mechanistic, which means that their parameters are based on reliable and concrete physiological and physical information. Gu et al. (2019) developed the mechanistic light response model (MLR) considering the key mechanisms linking ChlF emissions and photosynthesis for C3 and C4 plants from the concept of light use efficiency (LUE), later modified by Liu et al. (2022). Their results showed that the modeled GPP obtained from SIF quantifies the photosynthesis of the vegetation canopy with good accuracy at both half-hourly and daily scales when compared to the EC tower-based one

(Liu et al., 2022). Both models use modelled parameters from environmental conditions at the canopy scale (Gu et al., 2019; Liu et al., 2022). The determination of these parameters is key for the quality of the GPP simulated. They can be estimated through manual fluorescence measurements in the field, which thus is likely to enhance the robustness of the model.

## 1.3 Objectives

Passive fluorescence measurements (SIF) represent a powerful tool to estimate GPP because it contains information on the electron transport taking place between the two photosystems (Baker, 2008; Gu et al., 2019; Kramer et al., 2004). However, there are still an important number of unknowns and challenges to overcome when modelling photosynthesis from fluorescence measurements. Their relationship indeed depends on many environmental and physiological factors and varies between vegetation types and species (Meroni et al., 2009; Goulas et al., 2017; Gu et al., 2019; Feng et al., 2021; Porcar-Castell et al., 2021). For instance, incoming radiation, phenology stages of the plant and even temperature can affect the relationship between SIF and GPP (Zhang et al., 2016; Goulas et al., 2017; Li et al., 2020; Shen et al., 2022). More importantly, stress, notably drought events, can considerably impact the relationship by decoupling the dynamic of the two variables and thus make SIF less convenient to monitor photosynthesis (Damm et al., 2010; Wohlfahrt et al., 2018; Jonard et al., 2020; Porcar-Castell et al., 2021; Martini et al., 2022; Shen et al., 2022). Accordingly, the dependence of the parameters intervening in the model with regards to environmental conditions is an essential aspect to take into account when it comes to modelling photosynthesis over multiple and varying ecosystems (Kramer et al., 2004; Cendrero-Mateo et al., 2015; Gu et al., 2019).
Against this background, the aim of this thesis is twofold:

1. assessing the relationship between SIF and GPP from the perspective of the MLR model for a winter wheat canopy,

2. characterising the dynamics of the model parameters with regards to environmental conditions.

# Chapter 2

# Material and Methods

## 2.1 Study site

### 2.1.1 Description

The study was conducted on a site located in Lonzée, in the province of Namur, at about 50 km SE of Brussels in Belgium (50°33'05.7"N 4°44'46.1"E, 167 m asl). This location is equipped with a meteorological station, recording data since 2004, and an Eddy covariance (EC) system. In 2017, the station was integrated into the European Integrated Carbon Observation System (ICOS) network and is labelled as Class 2 station since then (ICOS).

The studied plot is a cultivated area of approximately 12 ha. It is a rather flat zone with a maximum slope of 1.2 % oriented WSW. The climate of this region is temperate maritime, corresponding to the Cfb class in the Köppen classification (Köppen, 1884) and the mean precipitation and temperature are respectively of 743 mm and 10.2°C (ICOS). Dominant wind directions are coming from the NE and SW directions with a fetch of 200 and 240 m. The soil of the plot on which fluorescence measurements were conducted, in the SE direction from the ICOS station, is a Luvisol (FAO classification) divided into three major horizons whose edaphic properties are referred to in Table 2.1 (Buysse et al., 2017).

Table 2.1: Edaphic properties of the soil horizons in the plot located in the SE direction from the ICOS station in Lonzée, based on measurements carried out in 2017.

| Depth (cm) | Organic matter ($g.kg^{-1}$) | Clay (%) | Sand (%) | Silt (%) | $\theta_{fc}$ (%) | $\theta_{wp}$ (%) | Bulk density ($g.cm^{-3}$) |
|---|---|---|---|---|---|---|---|
| 0 - 40 | 18.65 | 11.12 | 8.38 | 80.50 | 38.10 | 12.10 | 1.40 |
| 40 - 80 | 6.85 | 16.70 | 6.60 | 76.70 | 44.00 | 16.40 | 1.44 |
| 80 - 120 | 3.12 | 19.70 | 5.60 | 74.70 | 48.50 | 22.20 | 1.49 |

### 2.1.2 Crop management

The site has been cultivated for more than 75 years. For at least two decades, the agricultural practice applied has been a 4-year rotation composed successively with sugar beet (*Beta vulgaris* L.), winter wheat (*Triticum aestivum* L.), potato (*Solanum tuberosum* L.) and winter wheat (*Triticum aestivum* L.) again (Aubinet et al., 2009; Belgium). Concerning this present study, the winter wheat crop (*Triticum aestivum* L. *var* LG skyscraper) was sown on October $10^{\text{th}}$ 2021 and harvested the week of July $18^{\text{th}}$ 2022. For the purposes of the study, the wheat canopy has been considered as a single canopy layer. At the moment, data referring to agricultural treatments are not available.

## 2.2 Micro-meteorological and biomass measurements

### 2.2.1 Micro-meteorological data and carbon fluxes

The majority of the measurements were performed by sensors implemented on the station in the center of the cropland (cf. Figure 2.2). Sensors collecting meteorological data as well as photosynthetic flux radiation are described in detail in (Buysse et al., 2017) except those measuring soil water content, soil temperature and Normalized Difference Vegetation Index (NDVI). First, soil profile of water content and temperature were measured at a sub-plot situated in the SE direction from the ICOS station, at about 10 m from the place where fluorescence has been measured. The soil conditions of these two locations were assumed similar. Soil water content was measured by a transistor and a capacitance sensor (EnviroSCAN Probe, Sentek Sensor and Stepney, SA, AU) at five different depths: 5, 15, 25, 55 and 85 cm. Aberrant

Figure 2.1: The Fluorescence Box (FloX) located in the SE direction from the ICOS station in Lonzée.

Figure 2.2: The ICOS station located in the centre of the winter wheat crop in Lonzée.

fluctuations, potentially caused by temperature effects, have been corrected by considering only the maximal soil water content for each concerned day (Campbell Scientific, 2016). Likewise, soil temperature was measured by a platinum resistance thermometer (Temperature Profile Probe MTPP and PT100D Digital Thermometer, MicroStep spol. s r.o, Bratislava, SK) at six depths: 1, 5, 15, 25, 55 and 85 cm. Then, NDVI was measured by a NDVI sensor situated at 2.15 m high (Labo ESE Unif Paris). All data were averaged with a 30-minute timestamp and UTC+1 time reference has been used in the data files after treatment.

### 2.2.2 Biomass data

Twelve campaigns of plant biomass measurements were performed at the Lonzée site. Soil samples were taken close to the ICOS station with the random sampling method according to two modality: on seeding lines and midway between them. For both, from five to six cores were collected, totalling around ten cores per sampling day. Each core has been divided into samples corresponding to the following layers: 0-15, 15-30, 30-45, 45-60, 60-80 and 80-100 cm. Afterwards, soil samples were left for setting in salted water for one hour in order to be able to separate clay from tissues and to retrieve living roots. After collecting the roots, they were placed in a heat chamber (65°C) for at least three hours and weighed. These dry weight measurements were used to compute the root biomass ($g.m^{-2}$) present in each sample by dividing them by the soil sample surface, equivalent to the auger cross section. After that, the specific root biomass was determined for the following depths: 15, 30, 60, 80 and 100 cm by means of a fitted sigmoid function between the depth and the cumulative root biomass from the surface. Subsequently, these values were used to parameterize cubic curves reprensenting the temporal evolution of the proportion of root biomass for 10cm-deep soil layers (cf. Figure 2.3) These transformations are required to compute relative extractable water over the studied period (see section 2.2.3).

### 2.2.3 Quantification of soil relative extractable water

The relative extractable water (REW) was determined for each time step (30-minute interval) over the studied period from the following equation:

$$REW_t = \frac{EW}{AW} = \frac{\Sigma\alpha_i(\theta_{t,i} - \theta_{wp,i})}{\Sigma\alpha_i(\theta_{fc,i} - \theta_{wp,i})} \tag{2.1}$$

where $EW$ is the amount of extractable water (mm), $AW$ the potential maximum amount of available water (mm), $i$ the soil layer index, $\alpha$ the proportion of root biomass compared to the total one, $\Theta_{wp}$ and $\Theta_{fc}$ the soil water content at wilting point and field capacity and $\Theta_t$ the soil

water content (SWC). The underlying assumption of the method is that the water uptake is proportional to the root biomass. To compute $\alpha$, the mean proportion of root biomass for each day was computed for six soil layers (0-10, 10-20, 20-30, 30-40, 40-80, 80-120 cm) by using, and eventually summing, values of corresponding 10-cm depth layers from the temporal evolution of layer proportion of root biomass established previously (cf. Figure 2.3, section 2.2.2). The centres of these six layers correspond to the SWC measurements depths. Any data with negative

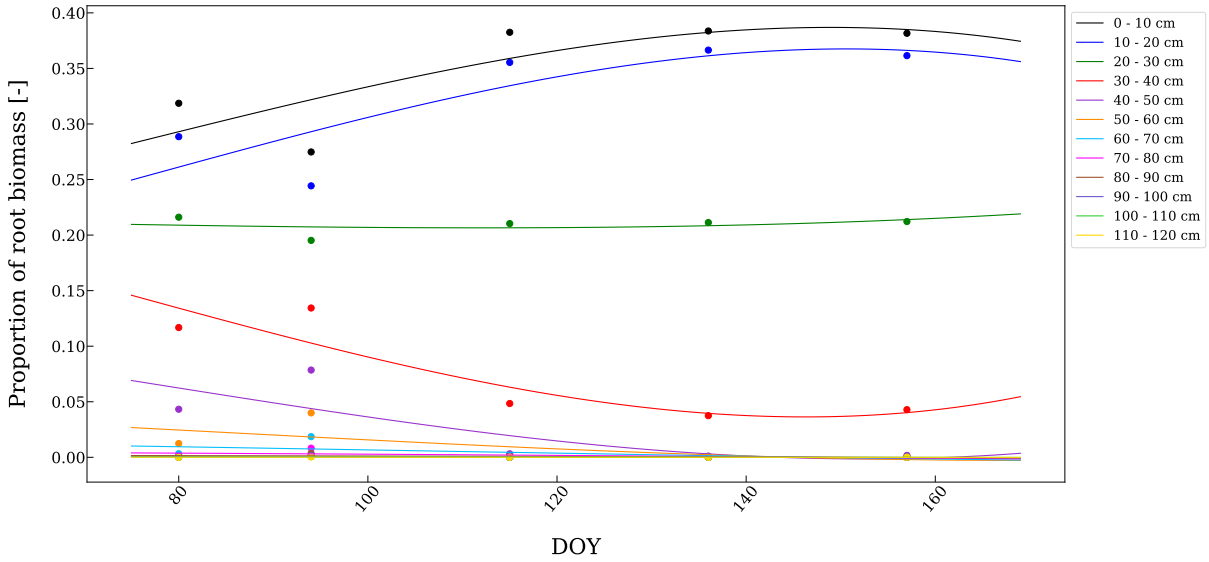


Figure 2.3: Evolution of the percentage of root biomass per soil layer from day of year (DOY) 75 to 170.

REW, probably caused by natural uncertainty on the determination of soil water content at field capacity and wilting point, has been set to 0 (3.451 % of the data set).

### 2.2.4 Quantification of vapor pressure deficit

Vapor pressure deficit (VPD, kPa) has been computed for each time step from the relative humidity (RH, %) and the air temperature ($T^{air}$, °C) with the following equations (Allan et al., 1998):

$$e_{sat}(T_{air}) = 0.61078 \times \exp\left(\frac{17.27 \cdot T_{air}}{237.7 + T_{air}}\right) \tag{2.2}$$

$$VPD = e_{sat}(T_{air}) \times (1 - \frac{RH}{100}) \tag{2.3}$$

$$\tag{2.4}$$

### 2.2.5 Monitoring to the winter wheat crop development

Green area index (GAI) was measured eight times throughout the study period, based on the basic ICOS procedure (Gielen et al., 2018). More precisely, the air bodies of around five to six randomly selected plants were collected on one-metre transects on the seed rows. After cleaning and weighing, the living leaves fraction was scanned by using the Digimizer software (version 5.7.2, MedCalc Software Ltd, Belgium) and GAI was estimated from it. Later, a sigmoid function has been fitted on GAI observations to obtain its temporal evolution in order to estimate it over the study period. The BBCH stages were estimated from the DAISY model (Hansen et al., 1991). The evolution of these stages and of the GAI for the cultivated winter wheat crop are illustrated in Figure 2.4.

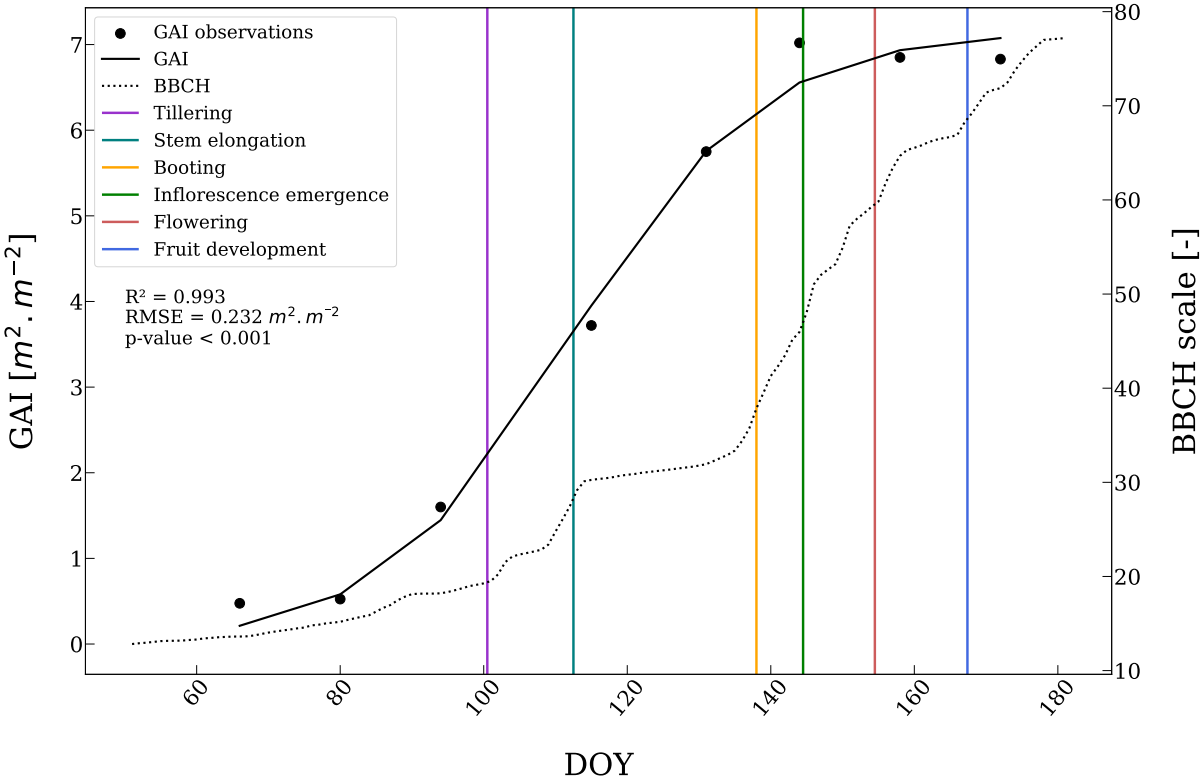


Figure 2.4: Evolution of the green area index (GAI) and the principal growth stages of the cultivated winter wheat according to the BBCH scale for cereal crops (Meier, 2018) from day of year (DOY) 51 to 181. Vertical lines indicate the beginning of each principal growth stage referenced.

## 2.3 Fluorescence measurements

### 2.3.1 Sun-induced fluorescence measurements

The Fluorescence Box (FloX) field spectrometer measures sun-induced fluorescence, upwelling and downwelling pohtosynthetically active radiation (PAR) together with upwelling and downwelling radiance by the means of optical fibres. Spectrally resolved reflectance at 750 and 760 nm and vegetation indices were obtained after raw data processing (JB hyperspectral devices, Düsseldorf, Germany). The FloX is equipped with two spectrometers (QE Pro, Ocean Optics, USA) focusing on different spectra. The first one (FLUO) has a spectral resolution of about 0.3 nm and performs measurements within the fluorescence spectrum, which ranges from 650 to 800 nm, covering the $O_2$A and $O_2$B bands (red and near-infrared zone). The second one (FULL) focuses on the visible and near-infrared zones and has a spectral resolution of 1.5 nm. They had a field of view upwards and downwards of about 180° and 20° (De Cannière et al., 2021; UG, 2022). The two devices were located at 2.10 m high and were performing measurements over a 4-$m^2$ area (cf. Figure 2.1). The device was set up on March 8$^{th}$ 2022 and dismantled on July 18$^{th}$ 2022.

### 2.3.2 Fluorescence measurements with the LI-6400XT Portable Photosynthesis System

Leaf level fluorescence and gas exchange measurements were conducted manually with the LI-6400XT Portable Photosynthesis System equipped with a 6400-40 Leaf Chamber Fluorometer (LI-COR Biosciences, Inc, Lincoln, Nebraska) from April 10$^{th}$ to around July 1$^{st}$ which corre-

Table 2.2: Principal parameters measured with the LI-6400XT Portable Photosynthesis System (Baker, 2008; LI-COR Biosciences, Inc, 2011).

| **Symbol** | **Corresponding measured fluorescence parameter** |
|---|---|
| $F'_o$ | Minimal fluorescence of a light-adapted leaf |
| $F_s$ | Steady-state fluorescence of a light-adapted leaf |
| $F_m$ | Maximal fluorescence during a saturating light flash on a dark-adapted leaf |
| $F_v$ | Variable fluorescence |
| $F_o$ | Minimal fluorescence of a dark-adapted leaf |
| $q_P$ | Photochemical quenching |
| $NPQ$ | Non-photochemical quenching |
| $\frac{F_v}{F_m}$ | Maximal quantum yield of PSII photochemistry $\Phi_{PSIImax}$ |
| $\Phi_{PSII}$ | PSII photochemical quantum yield |
| $C_i$ | Sub-stomatal $CO_2$ concentration ($\mu molCO_2.mol^{-1}$) |
| $A$ | Photosynthetic rate ($\mu molCO_2.m^{-2}.s^{-1}$) |
| $g_w$ | Conductance to $H_2O$ ($\mu molH_2O.m^{-2}.s^{-1}$) |
| $PAR_i$ | In-chamber photosynthetic active radiation ($\mu mol.m^{-2}.s^{-1}$) |

sponds approximately to fifteen days before the crop harvest. Between these two dates, measurements have been conducted on the field at least two days per week and with varying weather and environmental conditions. The chosen leaves for the measurements were the youngest and the most exposed ones. Those measured on the same day were to be of about the same colour and of the same anatomy in order to prevent other factors, such as different nitrogen contents, to impact fluorescence and gas exchange measurement. The preparation checklist was applied according to the device manual (LI-COR Biosciences, 2011) (page 4-2 to 4-4). Then, the calibration steps were applied as explained in details from page 4-4 to 4-6 in the device manual (LI-COR Biosciences, 2011). During measurements, the flow rate has been set to 500 $\mu mol.s^{-1}$, the reference $CO_2$ to 400 $\mu mol.mol^{-1}$ and the light source to the Track Ambient PAR mode in order to obtain incident PAR equivalent to ambient value. Concerning the air water vapour concentration, the relative humidity was set as close as possible to the ambient one by putting the dessicant on full bypass. The measured fluorescence and photosynthetic parameters are presented at Table 2.2. The handlings were divided in two phases : the dark and the light one. At first, the leaf was placed in the dark. After an adaptation time of at least 5 minutes, fluorescence parameters of dark-adapted leaves were measured following a non actinic saturation flash, which means that its intensity was not sufficient to launch photosynthesis. Then, the lamp was turned on and set on tracking the ambient PAR value. After a minimum of 20 min to reach a steady state fluorescence and gas exchange, a saturation flash followed by a dark pulse was imposed to the leaf and the rest of the fluorescence parameters could be measured. For every measured fluorescence and pohotsynthetic parameters, values outside 1.5 times the interquartile range over the whole dataset were considered outliers and removed. In addition, data corresponding to a negative ratio of carbon assimilation (A) on stomatal conductance ($g_s$), obtained from the leaf conductance to $H_2O$ ($g_w/1.6$), were also removed. Furthermore, the light response curve of photosynthetic rate (A) has been modelled by the Mitscherlich from incoming PAR ($PAR_i$) as follows:

$$A = a \times (1 - exp(-b \times (PAR_i - c))) \tag{2.5}$$

## 2.4 Gross primary production estimation from Eddy covariance measurements

Gross primary production (GPP) was estimated over the study period from flux-tower measurements by using the Eddy-covariance (EC) method (Wohlfahrt et al., 2012). The REddyProc package (Max Planck Institute for Biogeochemistry, Germany, `https://cran.r-project.org/package=REddyProc`) has been used to discard biased flux measurements corresponding to periods of low turbulent mixing by using the $u^*$ correction method ($u^* < 0.19895\ m.s^{-1}$), to gap fill data, to obtain the gross $CO_2$ assimilation (GPP) and the ecosystem respiration (Reco) thanks to flux partitioning. The flux data post-processing methods used in the REddyProc package are described in Wutzler et al. (2018). More precisely, post-processed data with quality flag of 0 or 1, corresponding respectively to the original data and to the most reliable data, were kept, while the rest was discarded. These quality flags were determined by the steady-state test (Mauder et al., 2021, Chapter 6). Similarly to Liu et al. (2020), only daytime data (PAR $> 20$ $\mu molPhoton.m^{-2}.s^{-1}$) and data corresponding to non-rainy days (Precipitation = 0 mm) have been used in the analysis.

## 2.5 Gross primary production modelling from Sun-induced fluorescence

### 2.5.1 Description of the model

Gross primary production has been modelled thanks to the mechanistic light response model (MLR) established by Gu et al. (2019). The rate of the linear electronic transport J ($\mu mol.m^{-2}.s^{-1}$) has been estimated from SIF and fluorescence parameters as follows (Gu et al., 2019; Liu et al., 2022):

$$J = q_L \times \frac{\Phi_{PSIImax}(1 + k_{DF})}{(1 - \Phi_{PSIImax})} \times SIF_{TOT\_FULL\_PSII} \tag{2.6}$$

where $q_L$ is the fraction of photosystem 2 (PSII) reaction centres that are open (-), $\Phi_{PSIImax}$ is the maximal photochemical quantum yield of PSII (-), $k_{DF}$ is a constant of de-excitation of the chlorophyll molecules (-) and $SIF_{TOT\_FULL\_PSII}$ is the sun-induced fluorescence emitted by all the leaves of the canopy over the full range of the fluorescence emission spectrum (from 640 to 850 nm) and comprising only the fluorescence emitted by PSII ($\mu mol.m^{-2}.s^{-1}$). One should note that $SIF_{TOT\_FULL\_PSII}$ does not correspond to the measured SIF ($SIF_{TOC\_760}$) and was determined from the latter by a method described in section 2.6. $k_{DF}$ has been computed as the ratio between $k_D$ and $k_F$. $k_D$ characterizes heat loss while $k_F$ represents the energy quenching via the fluorescence (Liu et al., 2022). Usually, these two parameters, considered as intrinsic properties of chlorophyll molecules, can be considered as constant under unstressed conditions (Porcar-Castell et al., 2014; Liu et al., 2022). Thus $k_{DF}$ has been assumed to be equal to 19, as in the MLR model version presented by (Gu et al., 2019). $\Phi_{PSIImax}$ represents the maximal PSII efficiency at which absorbed energy is used for photochemical reactions (Baker, 2008). It is assumed to be constant and conserved over all plant species under unstressed conditions (Porcar-Castell et al., 2014; Janka et al., 2015; Gu et al., 2019). When $J$ is obtained, GPP can be estimated by applying the FvCB model for C3 species (Farquhar et al., 1980; Gu and Sun, 2014):

$$GPP = \frac{C_i - \Gamma^*}{4C_i + 8\Gamma^*} \times J \tag{2.7}$$

where $C_i$ is the sub-stomatal $CO_2$ concentration ($\mu molCO_2.mol^{-1}$) and $\Gamma^*$ is the chloroplastic $CO_2$ compensation point ($\mu mol.mol^{-1}$). In this formulation of the MLR model, $C_i$ is considered equal to $C_c$ because the mesophyll conductance is assumed to be infinite. According to the $CO_2$

diffusion model based on Fick's law, $C_i$ is given by:

$$C_c \approx C_i = C_a - \frac{A}{g_s} \tag{2.8}$$

where $C_a$ is the atmospheric $CO_2$ concentration ($\mu molCO_2.mol^{-1}$), A is the $CO_2$ assimilation rate ($\mu molCO_2.m^{-2}.s^{-1}$) and $g_s$ is the stomatal conductance ($mol.m^{-2}.s^{-1}$). At a first attempt, $C_i$ has been estimated for each time step (30-minute interval) by a model depending only on air temperature. Indeed, $C_i$ and especially A and $g_s$ have been observed to vary with air and leaf temperature for different plant species (Weston and Bauerle, 2007; Janka et al., 2015; Urban et al., 2017; Huang et al., 2021).

Equation 2.7 is used to predict GPP when the photosynthesis is limited by the regeneration of the metabolite RuBP (ribulose-1,5-bisphosphate), in the specific case when NADPH is insufficient in the first stages of the Calvin cycle due to low incoming PAR intensity. In case of high incoming light, the electron transport chain becomes overloaded, leading to the saturation of the $CO_2$ assimilation rate. At this point, an increase of irradiance will not have any effect on photosynthesis, and only Rubisco (ribulose 1,5-bisphosphate carboxylase/oxygenase) can become a limiting factor (Farquhar et al., 1980; Sharkey et al., 2007; Gu and Sun, 2014).

### 2.5.2 Estimation of the parameters

#### Fraction of PSII open reaction centers

The reaction centres, located in the photosystems, are the location where the photochemical reactions take place after having received the excitation energy from the chlorophyll molecules (Reed, 1969). When a reaction centre is said to be "open", it means that it is able to reduce $CO_2$ by using the excitation energy. Hence, $q_L$ represents the number of reaction centers that are functional. In particular, this parameter is based on the lake model which considers that all reaction centers of PSII are encased in a matrix with the pigment proteins and that each of the fucntional ones is able to receive the excitation energy from the surrounding pigment molecules as well as to transfer it to other reaction centres (Baker, 2008; Gu et al., 2019; Porcar-Castell et al., 2021). $q_L$ has been estimated with the following formula (Kramer et al., 2004; Baker, 2008; Kasajima et al., 2009):

$$q_L = q_P \times \frac{F'_o}{F_s} \tag{2.9}$$

where $q_P$ is the photochemical quenching (-), $F'_o$ is the minimal fluorescence of a light-adapted leaf and $F_s$ is the steady-state fluorescence of a light-adapted leaf. All these variables were measured by the LI-6400XT Portable Photosynthesis System measurements. Unrealistic $q_L$ values (higher than 1) have been removed.

In the perspective of deducing directly GPP from SIF data, obtaining the $q_L$ value from very easy measurable parameters is essential. $q_L$ is mainly affected by the incoming PAR with a strong influence producing diurnal pattern (Baker, 2008; Zivcak et al., 2014; Janka et al., 2015; Cendrero-Mateo et al., 2015; Chang et al., 2021). Therefore, the setting of a model describing the evolution of $q_L$ with increasing PAR has been attempted in this work, based on leaf-level measurements, in order to be able to estimate $q_L$ for any PAR levels. Four models have been tested: a linear model, a cubic model, an exponential model proposed by Chang et al. (2021) and a power law model. The quality of each regression has been assessed by determining the determination coefficient ($R^2$), the corrected Akaike's Information Criterion ($AIC_c$), the relative mean square error (RMSE) and an F-test in order to check if the model generates a significantly better fit than the intercept-only model, considering a confidence level of 95 %.

#### Non-photochemical quenching

Non-photochemical quenching represents one of the thermal dissipation mechanisms which protect the photosynthetic machinery from the damages caused by an excess of absorbed energy when $CO_2$ assimilation saturates at high PAR levels (Yamamoto et al., 1999; Horton, 2013; Mohammed et al., 2019). Even though this parameter is not used in the MRL model proposed by Gu et al. (2019) to obtain GPP, it is used in the reworked version proposed by Liu et al. (2022) and is, all things considered, a noteworthy parameter to study given that it is involved in the energy partitioning of the plant as well as in its energetic regulatory mechanisms. So, there is a marked interest in being able to deduce its value from easily measurable parameters. Similar to $q_L$, NPQ is affected by environmental conditions (Cendrero-Mateo et al., 2015; Janka et al., 2015; Gu et al., 2019; Chang et al., 2021), and so, four models describing the evolution of NPQ with increasing PAR have been fitted in this work and compared to each other to find the most realistic one. The models tested are the linear model, the cubic model, a model of exponential saturation (Ritchie, 2008) and a model based on the Hill equation proposed by Serôdio and Lavaud (2011).

#### Chloroplastic $CO_2$ concentration point

The chloroplastic $CO_2$ compensation point is the chloroplastic $CO_2$ concentration when photosynthesis is compensated by photorespiration and no net assimilation occurs (Farquhar et al., 1980). $\Gamma^*$ is temperature-dependent and increases with rising temperature (Bernacchi et al., 2001). Its response to air temperature has been modeled with the following equation (Katul et al., 2010):

$$\Gamma^* = 36.9 + 1.18 \times (T_{air} - 25) + 0.036 \times (T_{air} - 25)^2 \tag{2.10}$$

where $T_{air}$ is the air temperature (°C). This parameterization has been validated for a very large number of plant species.

## 2.6 Downscaling from measured SIF to total broadband SIF

The SIF measured was the one retrieved by using the Spectral fitting method (SFM) from the oxygen ($O_2A$ band) absorption lines at 760 nm ($SIF_{TOC\_760}$, $mW.m^{-2}.nm^{-1}.sr^{-1}$). Only far-red SIF has been used because it has been observed to be more closely related to GPP than red SIF and it potentially contains information associated with both the top of the canopy and the lower layers (Goulas et al., 2017; Jonard et al., 2020). Moreover, in the red region, SIF is more subject to re-absorption (Liu et al., 2016a; Chang et al., 2021). This measurement corresponds to a fluorescence emission per surface of land area ($m^2$) composed of bare soil and vegetation. In order to model J and GPP through equations 2.6 and 2.7, the broadband SIF emitted from all the leaves within the footprint area and by considering only the PSII contribution ($SIF_{TOT\_FULL\_PSII}$, $\mu mol.m^{-2}.s^{-1}$) has been estimated from the SIF measurements ($SIF_{TOC\_760}$). The different steps to establish this correspondence are described in the following sections and are similar to the method described by (Liu et al., 2022).

### 2.6.1 Retrieval of the contribution of photosystem II from the SIF measured at the top of the the canopy

Far-red SIF is composed of fluorescence emitted from PSII and PSI (Mohammed et al., 2019; Liu et al., 2016a). Nevertheless, the link between fluorescence and photochemistry is the actual rate of the electron transport $J$ originating from PSII to PSI (Baker, 2008; Kasajima et al., 2009; Frankenberg and Berry, 2017; Gu et al., 2019; Porcar-Castell et al., 2021). Therefore, the contribution of PSII to SIF at 760 nm at the top of the canopy ($SIF_{TOC\_760\_PSII}$, $mW.m^{-2}.nm^{-1}.sr^{-1}$)

has been estimated as follows:

$$SIF_{TOC\_760\_PSII} = SIF_{TOC\_760} \times f_{PSII} \tag{2.11}$$

where $f_{PSII}$ (%) is the contribution of the PSII fluorescence to the measured signal at the top of the canopy:

$$f_{PSII} = \frac{m_2 \times \epsilon}{m_1 + m_2 \times \epsilon} \tag{2.12}$$

The parameters $m_1$ and $m_2$ were taken equal to 0.00561 and 0.00917 similarly to Liu et al. (2022). Then, $\epsilon$, a factor controlling the fluorescence emission from PSII, has been estimated from the ratio of the maximal ($F_m$) and the minimal fluorescence ($F_0$) of a dark-adapted leaf measured manually by the LI-6400XT Portable Photosynthesis System (Liu et al., 2022):

$$\epsilon = \frac{\Phi_F}{\Phi_{F0}} \tag{2.13}$$

### 2.6.2 Estimation of the total SIF emitted from PSII at 760 nm

To obtain the SIF flux density emitted by PSII from all the leaves at 760 nm ($\mathrm{SIF_{TOT\_760\_PSII}}$, $mW.m^{-2}.nm^{-1}$), $\mathrm{SIF_{TOC\_760\_PSII}}$ has been downscaled from the top of the canopy to the photosystem level by:

$$SIF_{TOT\_760\_PSII} = \pi \times \frac{SIF_{TOC\_760\_PSII}}{f_{esc\_PC}} \tag{2.14}$$

where $\mathrm{f_{esc\_PC}}$ is the probability of SIF photons to escape from PSII up to the top of the canopy at 760 nm and $\pi$ which permitted to integrate $\mathrm{SIF_{TOC\_760\_PSII}}$ over the hemispherical space (Liu et al., 2022). $\mathrm{f_{esc\_PC}}$ has been computed from the multiplication of the leaf escape probability of SIF photons at 760 nm ($\mathrm{f_{esc\_PL}}$) by the leaf albedo (0.9) considered quite stable in the NIR region (cf. Equation 2.16). $\mathrm{f_{esc\_PC}}$ allowed the conversion of the SIF measurement done at the top of the canopy to a value of SIF per area of leaves. Indeed, $\mathrm{f_{esc\_PC}}$ represents, in a sense, the proportion of the canopy within the footprint of the SIF sensor. In fact, a low value of $\mathrm{f_{esc\_PC}}$ means that the canopy is covering a small proportion of the land area while a value close to 1 corresponds to a highly developed canopy. In other words, the probability that a SIF photon escapes the canopy and reaches the sensor is maximum when the canopy is fully developed.

$$f_{esc\_LC} = \frac{NIRv}{f_{APAR}} \tag{2.15}$$

$$f_{esc\_PC} = 0.9 \times f_{esc\_LC} \tag{2.16}$$

$f_{esc\_LC}$ has been estimated from $\mathrm{f_{APAR}}$, accounting for the fraction of PAR radiation absorbed by the leaves, and NIRv, which is obtained by multiplying NDVI by the canopy reflectance in the NIR region, here taken at 760 nm (Equation 2.15). All values of NDVI outside the range expanding from 0 to 1 have been removed because values higher than 1 and lower than -1 don't have a physiological meaning and values lower than 0 generate a negative probability ($\mathrm{f_{esc\_LC}}$) which is impossible. $\mathrm{f_{APAR}}$ has been computed from the the wide dynamic range vegetation index (WDRVI), itself determined from NDVI (Liu et al., 2022):

$$WDRVI = \frac{(a+1) \cdot NDVI + (a-1)}{(a-1) \cdot NDVI + (a+1)} \tag{2.17}$$

$$f_{APAR} = \Psi \times (0.616 \cdot NDVI + 0.726) \tag{2.18}$$

with $a$ and $\Phi$ equal to 0.2 and 0.79 respectively.

### 2.6.3 Reconstitution of broadband SIF

The broadband SIF is obtained by integrating over the emission spectrum the dependance of SIF emission by PSII on wavelength. Then, the major step to reconstitute the broadband SIF was to determine SIF emitted by PSII from the whole canopy at a given wavelength ($SIF_{TOT\_\lambda\_PSII}$, $mW.m^{-2}.nm^{-1}$) from $SIF_{TOT\_760\_PSII}$. To convert $SIF_{TOT\_760\_PSII}$ into $SIF_{TOT\_\lambda\_PSII}$, a factor, called the "band conversion ratio" ($f_c(\lambda)$), has been estimated. For this purpose, a total of 6720 fluorescence spectra at photosystem level from 640 to 850 nm have been simulated by the Soil Canopy Observation of Photosynthesis and Energy model (SCOPE; version 1.73) (van der Tol et al., 2009).The different spectra correspond to different leaf structural and biochemical properties as well as distinct sun rays properties and canopy structures. The variation of these properties have been taken identical to those used by Liu et al. (2022). Moreover, the simulation took also into account the hemispherical integration and the reabsorption effect impacting chlorophyll fluorescence. Then, a basis spectrum describing the distribution of the SIF spectrum has been extracted from the simulated dataset using the SVD method (Zhao et al., 2014). This analysis showed that the first principal component (PC1) explained more than 99.99 % of the variation of the fluorescence spectra at photosystem level. In other words, the spectral shape of PSII fluorescence stayed stable to a certain extent with varying leaf and canopy structural properties. For this reason, the PSII full spectrum ($SIF_{TOT\_\lambda\_PSII}$) have been expressed as a linear combination of the first singular vector ($v_1$) corresponding to PC1 (Zhao et al., 2014):

$$SIF_{TOT\_\lambda\_PSII} = \frac{SIF_{TOT\_760\_PSII}}{v_1(760)} \times v_1(\lambda) \tag{2.19}$$

The ratio of $v_1$ and $v_1(760)$ is representing $f_c(\lambda)$ which has been used to weight the SIF measurements done at 760 nm ($SIF_{TOT\_760\_PSII}$) with respect to the full fluorescence spectrum (see Appendix A.1). The last step to obtain $SIF_{TOT\_FULL\_PSII}$ was to integrate this spectrum over the wavelength range of interest and to perform an unit conversion :

$$SIF_{TOT\_FULL\_PSII} = \int_{640}^{850} SIF_{TOT\_760\_PSII} \times f_c(\lambda) \times \frac{\lambda \cdot 10^6}{h \cdot c \cdot N_A \cdot 10^3 \cdot 10^9} \tag{2.20}$$

with $\lambda$ the wavelength (nm), h, the Planck constant ($6.63 \times 10^{-34}$ J.s), c, the speed of light ($3 \times 10^8$ $m.s^{-1}$), and $N_A$, the Avogadro number ($6.02 \times 10^{23}$ $\mu mol^{-1}$). Finally, outliers of the resulting SIF have been removed by using the interquartile range method.

## 2.7 Computer resources

All handling described and performed on data have been done using the computing language Python (Python 3.8.8). The main libraries used are Lmfit, Matplotlib, Numpy, Pandas, Sklearn and Scipy, especially the integrate and optimize packages for this latter.

# Chapter 3

# Results & Discussion

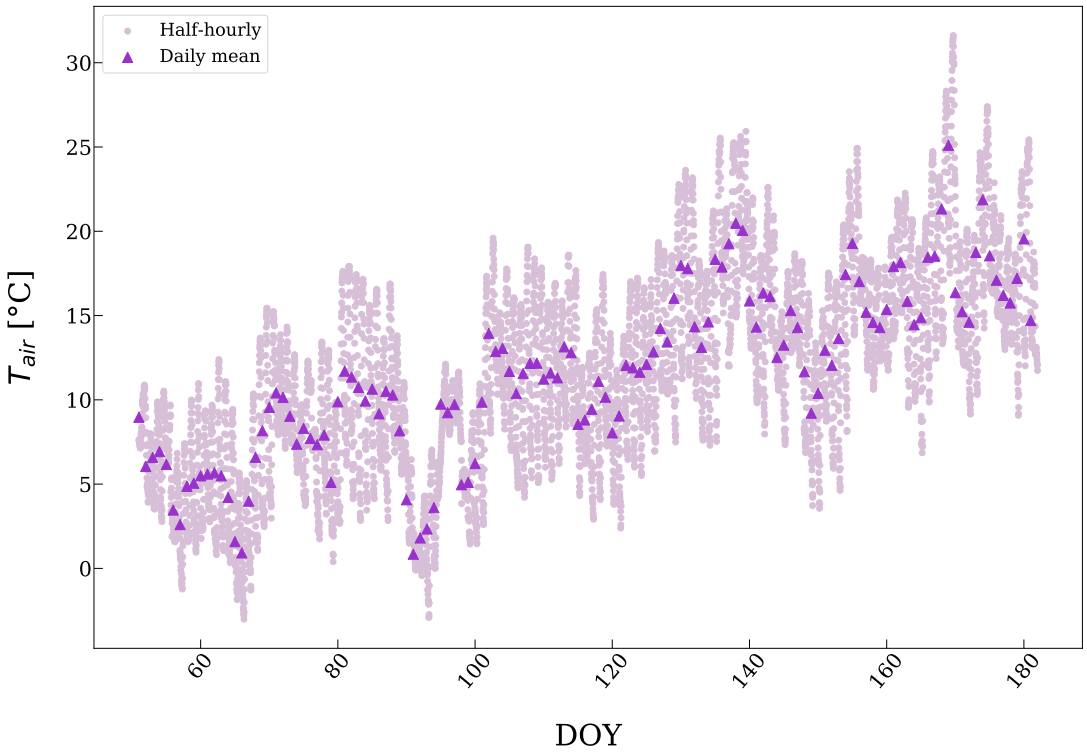


Figure 3.1: Evolution of the air temperature (T_air) from day of year (DOY) 51 to 181. Light pink points represent half-hourly observations while purple triangles indicate daily means.

## 3.1 Micro-meteorological and photosynthetic conditions over the course of the studied period

In this paper, the timescale will be further defined as day of year (DOY). As shown in Figure 3.1, $T_{air}$ has gradually increased over the studied period with minimal values close to 0°C found between DOY 51 and 100, a pronounced drop between DOY 90 and 100, and maximal values between DOY 160 and 181. Similarly, VPD is globally increasing throughout the study period as seen in Figure 3.2. Minimal values are found between DOY 51 and 100, in particular between DOY 80 and 100. Both $T_{air}$ and VPD reached a maximal value at DOY 169, respectively of 30.346 °C. and 2.630 kPa. Broadly speaking, an aerial drought stress can be considered happening when VPD reaches values above approximately 1.5 or 2 kPa (Urban et al., 2018; Paul-Limoges et al., 2018; Fakhet et al., 2021; Martini et al., 2022). This is the case for the fews pics located from DOY 120 to 181. In contrast, no heatwave has been detected according to the thresholds suggested by IRM (a) and Perkins and Alexander (2013). SWC dynamics over the measurement period, as well as the precipitation and REW evolutions, are shown at Figure 3.3. Over the whole study period (127 days), it rained a total of 161.85 mm, which is lower (∼30 %) than the mean value of 234.40 mm accounting for the same period over the years 1991-2020 (IRM, b). A maximal value of 8.16 mm has been reached at DOY 142. Regarding soil water content, it has globally declined over the study period. For SWC at 5, 15, 25 and 35 cm depth, this decrease was quite sharp since DOY 100 and was afterwards punctuated by sudden increases due to precipitation events. In deeper soil layers, this decrease is softened because root biomass is lower and thus, water collection is reduced. Moreover, SWC at 55 and 85 cm depth stabilised after precipitation events, probably because upper plant roots extracted the majority of the incoming water, preventing it from reaching deeper SWC sensors and reducing the need to collect water in deep layers. The REW, mainly driven by surface water contents, is following the same pattern. From about DOY 110, REW is plummeting to values below 0.4. With such

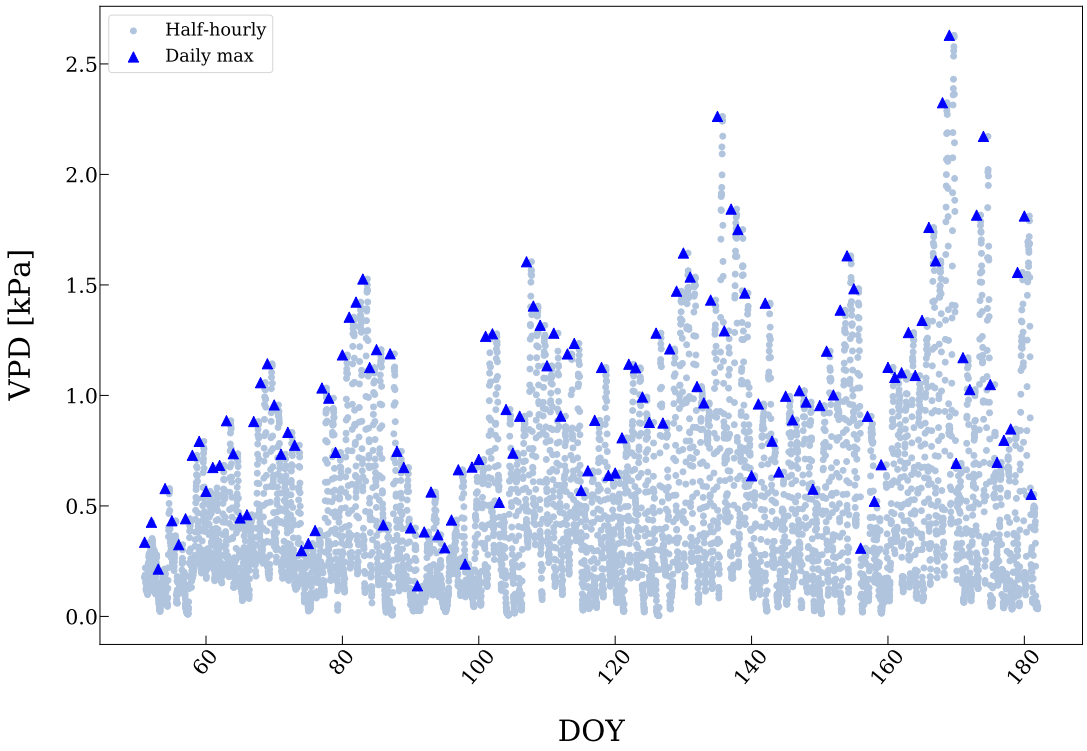


Figure 3.2: Evolution of the vapour pressure deficit (VPD) from day of year (DOY) 51 to 181. Light blue points represent half-hourly observations while dark blue triangles indicate daily means.

low REW, there are strong risks of edaphic drought, as already noted for European forest and maize (Jiang et al., 2018; Gourlez de la Motte et al., 2020). Afterwards, from DOY 140 to 181, REW, despite sudden increase caused by precipitation, reaches 0 several times and remains mostly below 0.4. This can be explained, as for soil water content by the potential important uptake of incoming water by roots in the first soil layers. Overall, these observations indicate a relative drought stress from DOY 120 to the end of the study period, especially for periods without precipitation events. The temporal evolution of incoming PAR, $GPP_{EC}$ and GAI is shown in Figure 3.4. Generally speaking, GPPEC has increased, reaching a maximal value of 18.714 gC.m-2.d-1 at DOY 133, then stabilised before finally slightly decreasing. Overall, the general GPP dynamic over the study period is synchronous with the evolution of PAR and GAI, indicating the surface where photosynthesis can take place. From Figure 2.4, three canopy development dynamics has been identified, comprising different phenological stages: from GAI 0 to 2, including plant germination and leaf development, then for GAI ranging from 2 to 6 which covers tillering and stem elongation and finally, GAI above 6, from booting to fruit development. These thresholds have been used in the following analysis (cf. section 3.4.5 on page 34). The light response curve of the photosynthetic rate (A) and its fit are represented at Figure 3.5. The photosynthetic rate increases with incoming radiation, before saturating at a value close to 20 $\mu molCO_2.m^{-2}.s^{-1}$. Prior to this value, A is assumed to be only limited by the regeneration of the metabolite RuBP (ribulose-1,5-bisphosphate), itself limited by insufficient ATP and NADPH in the first reactions of the Calvin cycle. During this period, most of the absorbed light energy is used by photochemical reactions and A is directly linked to the electron transport chain between photosystems II and I. In other words, this energy is dissipated through photochemical quenching. Subsequently, with the increase of PAR, the $CO_2$ assimilation rate gradually levels out due to more electrons saturating the electron transport chain. As a result, A value remains stable regardless of the increasing irradiance. On this part of the curve, A

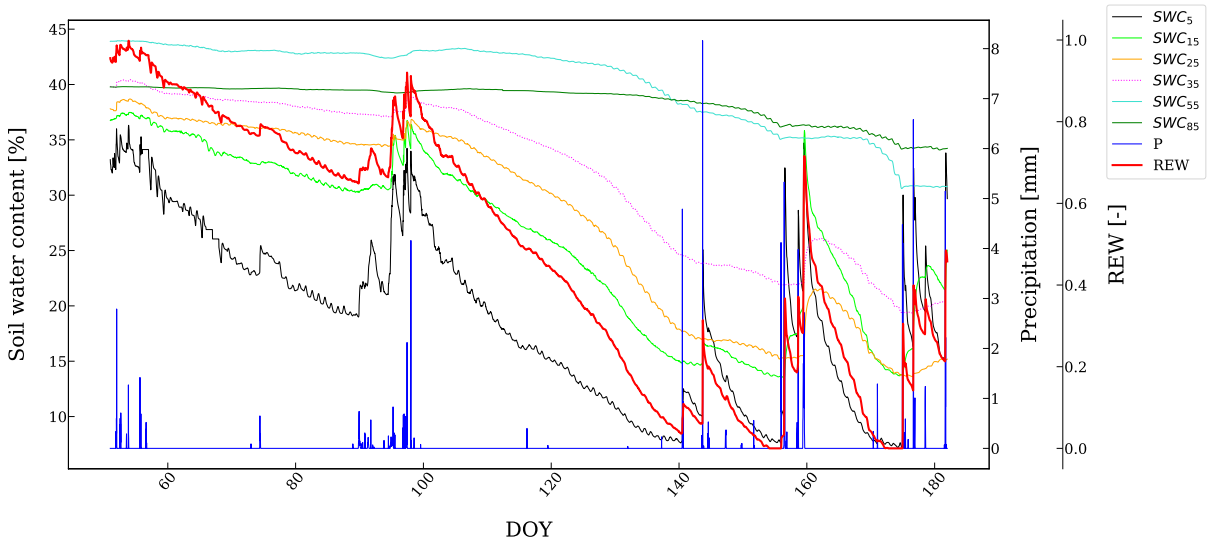


Figure 3.3: Evolution of the soil water content (SWC) from day of year (DOY) 51 to 181 at 5, 15, 25, 35, 55 and 85 cm depth. The evolutions of precipitation (P) and the relative extractable water (REW) are also represented. The soil water content at 35 cm has been linearly interpolated between $SWC_{25}$ and $SWC_{55}$ at each time step.

is limited by Rubisco which can be affected by stress conditions (Farquhar et al., 1980; Sage and Kubien, 2007; Sharkey et al., 2007; Galmés et al., 2013; Mathur et al., 2014; Porcar-Castell et al., 2014). The PAR threshold describing the beginning of the plateau has been estimated at 1350 $\mu molPhoton.m^{-2}.s^{-1}$. Because some uncertainties are associated with the determination of this curve, a range of ± 150 $\mu molPhoton.m^{-2}.s^{-1}$ has been considered when using the PAR threshold in the following analysis.

## 3.2 SIF dynamics

In figure 3.6, it can be observed that $SIF_{TOT\_FULL\_PSII}$ and GPPEC are exhibiting a relatively similar pattern of global increase until approximately DOY 130, before decreasing while oscillating. This is consistent with the rise of incoming PAR together with the development of the wheat canopy (cf. Figures 2.4 and 3.4). Such observations have already been done for different plant species including wheat (Mohammed et al., 2019; Yang et al., 2015; Goulas et al., 2017; Li et al., 2020; Pierrat et al., 2022). The fact that the narrowband (760 nm) measured SIF ($SIF_{TOC\_760}$) exhibits the same seasonal dynamic (data not shown) confirms the strong reliance of SIF on PAR (Chang et al., 2021). In the case of this study, the evolution of $SIF_{TOT\_FULL\_PSII}$ is also linked to the canopy development because it depends on $f_{esc\_PC}$, a parameter related to NDVI and $f_{APAR}$ (see section 2.6.2, page 16). On a diurnal scale, PAR is increasing, reaching a maximal value at midday, which induce GPP and SIF to grow during the first half of the day and then decline till the end of the day, as shown in Appendix A.2. Diurnal GPPEC and $SIF_{TOT\_FULL\_PSII}$ evolutions are strongly correlated (PCC = 0.923, see Appendix A.2) (Yang et al., 2015, 2018; Chang et al., 2021; Chen et al., 2021b). Indeed, GPP and SIF are driven by some common environmental variables, essentially the fraction of absorbed PAR (Yang et al., 2018; Gu et al., 2019; Chang et al., 2021; Chen et al., 2021b). As PAR is increasing, more energy becomes available for the plant carbon assimilation, which is the main pathway to dissipate energy when light is not-saturating, but also, to a lesser extent, for fluorescence emission and heat dissipation, as the three processes are complementary (Baker, 2008; Porcar-Castell et al., 2014; Cendrero-Mateo et al., 2015; Frankenberg and Berry, 2017; Gu et al., 2019; Jonard et al., 2020). Indeed, below typical high PAR levels, SIF is expected to be positively related to GPP,

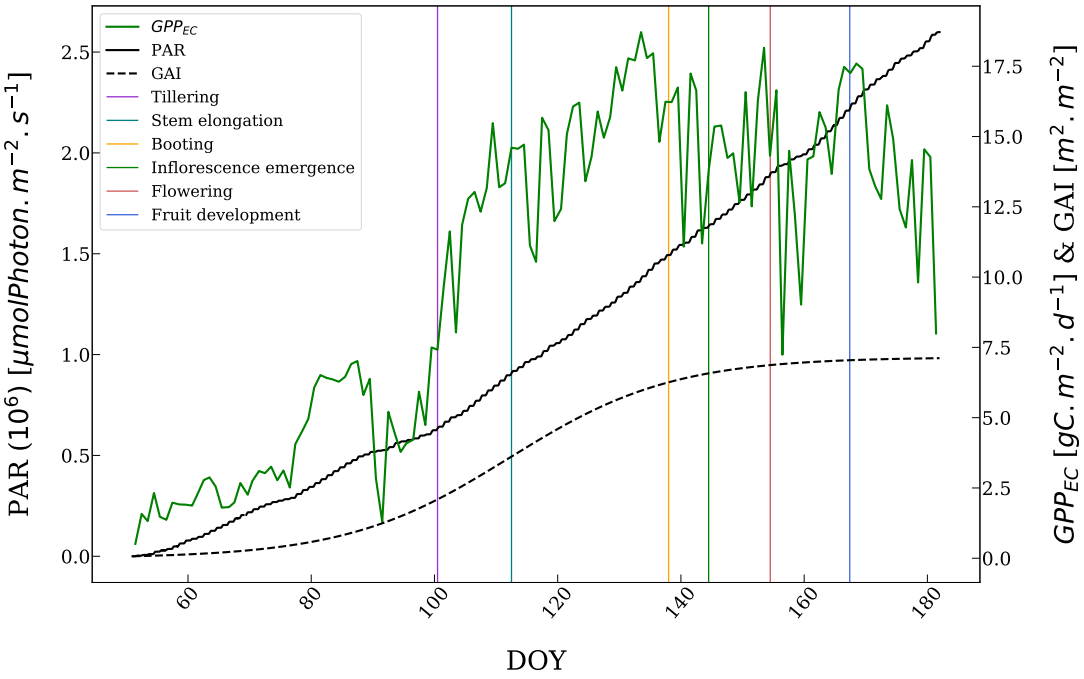


Figure 3.4: Evolution of cumulative incoming photosynthetically active radiation (PAR), the daily total gross primary production based on the Eddy-covariance technique (GPP_EC) and estimated green area index (GAI) from day of year (DOY) 51 to 181. Vertical lines indicate the beginning of each principal growth stage referenced.

driven by NPQ which dissipates the excessive energy. This might explain the positive seasonal correlation between GPP and SIF at the canopy scale (Porcar-Castell et al., 2021). Despite these commonalities, differences exist between $SIF_{TOT\_FULL\_PSII}$ and GPPEC. From DOY 51 to 70, SIF is relatively high compared to the GPP dynamic and this phenomenon is not observed with measured $SIF_{TOC\_760}$ (data not shown). This is explained by the fact that the canopy is not fully developed yet so $GPP_{EC}$ is low and is increased by small values of $f_{esc\_PC}$ accounting for the low vegetation proportion within the sensor footprint (see section 2.6.2 on page 16 and Figure 3.10). Accordingly, there is an increase of total emitted SIF ($SIF_{TOT\_760\_PSII}$) compared to what is emitted by the top of the canopy ($SIF_{TOC\_760}$) (cf. Equation 2.14, page 16). Then, around DOY 178 and 181, $SIF_{TOT\_FULL\_PSII}$ is unexpectedly very low for high GPP values. For this reason, these data have been considered as outliers and excluded from the analysis. Likewise, missing data between DOY 159 and 165 and at the end of the study period are due to sensor malfunctions.

## 3.3 Model parameters

### 3.3.1 Fraction of PSII open reaction centers and non-photochemical quenching

Continuous functions describing the fluctuations of the model parameters with environmental conditions are needed to model GPP from SIF measurements. Here, different parameterizations to estimate $q_L$ from incoming PAR are shown in Figure 3.7. All the models provide a significantly better fit the an intercept-only model and have close values of $AIC_c$, $R^2$ and RMSE (cf. Appendix A.1). Nevertheless, the model providing the smallest AICc, is the power law model. However, the use of this model can lead to extreme values of $q_L$ for low values of PAR. But since data corresponding to such situations are excluded (PAR $< 20\ \mu mol.m^{-2}.s^{-1}$), the issue does

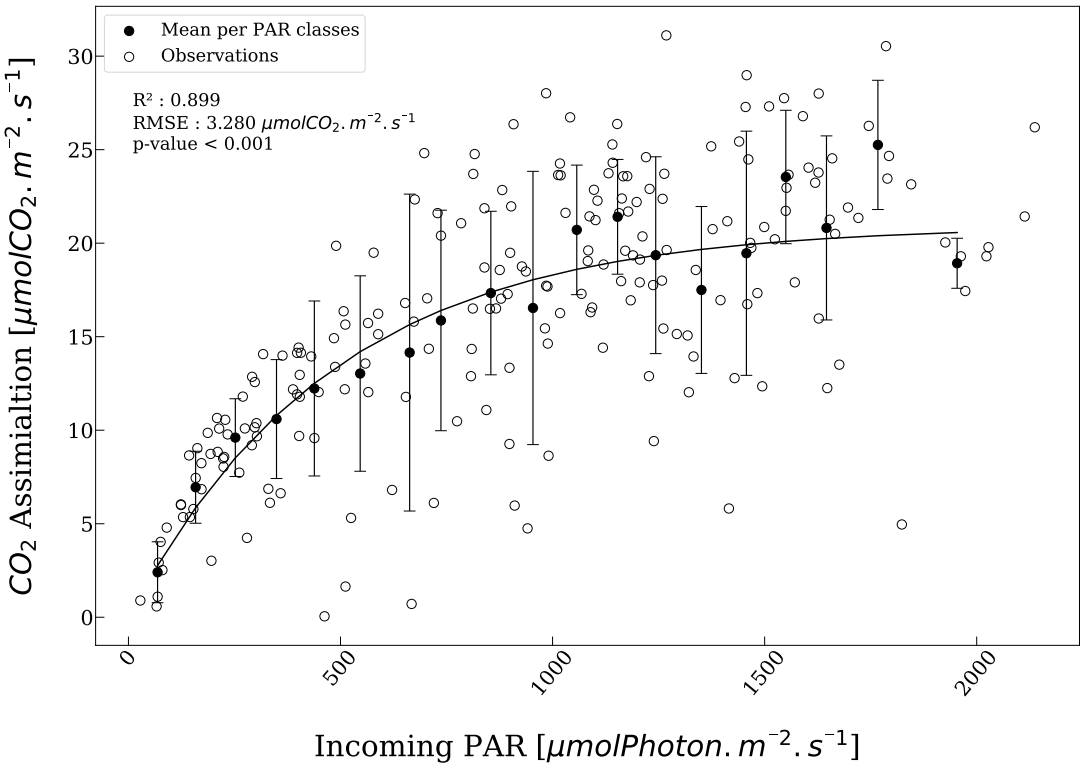


Figure 3.5: Light response curve of $CO_2$ assimilation rate (A) measured by the LI-6400XT Portable Photosynthesis System. The curve has been modelled using the Mitscherlich model fitted on the mean of A per PAR classes of 100 $\mu molPhoton.m^{-2}.s^{-1}$ width. The saturating value of PAR ($PAR_{sat}$) has been estimated from the asymptote (a) of the model and its standard deviation ($\sigma_a$) ($PAR_{sat} = \ln\left(\frac{\sigma_a}{a}\right) \times \left(\frac{-1}{b}\right) + c$), giving a $PAR_{sat}$ of 1350 $\mu molPhoton.m^{-2}.s^{-1}$.

not arise in this study. Besides, it provides a correct physiological dynamic of $q_L$. As shown in previous studies, $q_L$ decreases with incoming PAR and stabilises at high PAR values, a dynamic directly related to the evolution of $CO_2$ assimilation rate seen in Figure 3.5. In the dark, all reaction centres are considered open, which means that their electron acceptor is fully oxidised and ready to accept electrons. With increasing incoming PAR, more and more reaction centres are reduced because of the absorbed energy and hence, the fraction of open reaction centres declines until the PAR range corresponding to the carbon assimilation saturation, leading to a stabilisation of $q_L$ (Kramer et al., 2004; Baker, 2008; Gu et al., 2019). As seen in Figure 3.7, $q_L$ stabilises at approximately 0.4 for PAR values higher than approximately 1000 $\mu mol.m^{-2}.s^{-1}$. It means that the maximum percentage of reduced reaction centres is 60 %. In the model version coming from Gu et al. (2019) and used in this study, $q_L$ enables the estimation of J (cf. Equation 2.6, page 13) while in the revised version proposed by Liu et al. (2022), NPQ is used instead of $q_L$. For reasons already described previously (cf. section 2.5.2 on page 15), it is an interesting parameter to parametrize in order to understand the plant photosynthetic behaviour. Observed NPQ is linearly increasing with incoming PAR, as seen in the literature (Cendrero-Mateo et al., 2015; Janka et al., 2015; Gu et al., 2019; Chang et al., 2021). Five models have been tested to parametrize NPQ from incoming PAR (cf. Appendix A.3). Similarly to $q_L$, parameters assessing the quality of the regression are close (cf. Appendix A.1). However, the model characterised by the smallest $AIC_c$ is the exponential saturation model (Ritchie, 2008).

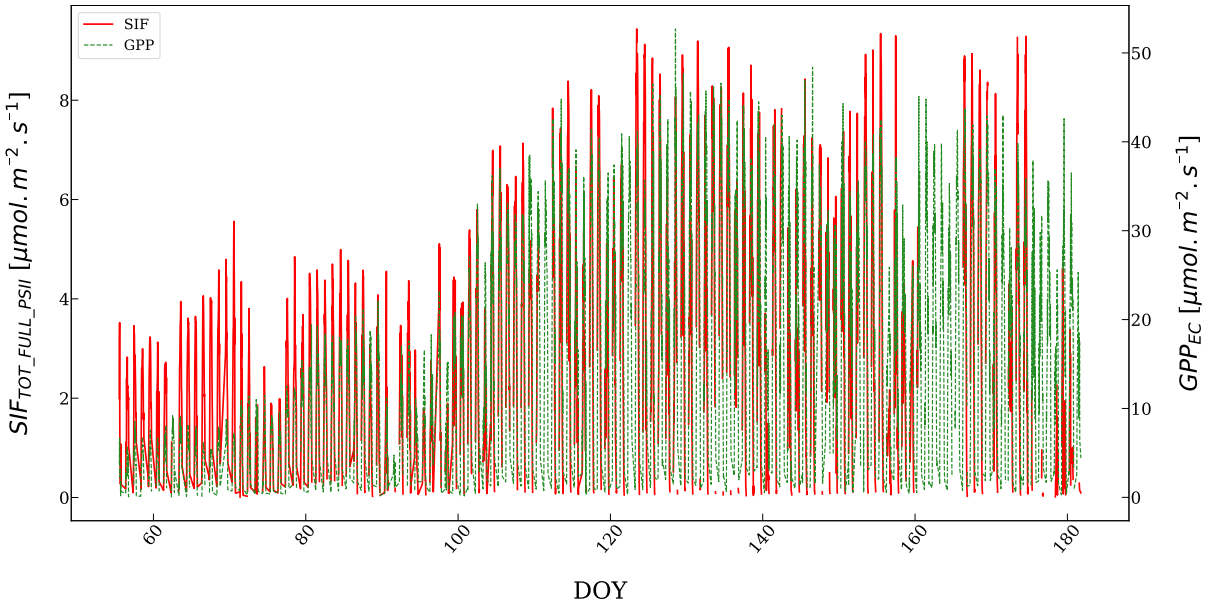


Figure 3.6: Evolution of half-hourly total broadband (640-850 nm) SIF emitted from PSII ($SIF_{TOT\_FULL\_PSII}$) and tower-based gross primary production ($GPP_{EC}$) from day of year (DOY) 51 to 181. Only values accounting for days of non-precipitation and incoming PAR higher than 20 $\mu molPhoton.m^{-2}.s^{-1}$ are shown.

### 3.3.2 Maximal photochemical PSII quantum yield

PSII photochemical quantum yield ($\Phi_{PSII}$) and maximal PSII photochemical quantum yield ($\Phi_{PSIImax}$) dynamics with respect to incoming PAR are shown at Figure 3.8. $\Phi_{PSII}$ decreases with incoming PAR. Indeed, as light energy is absorbed by the plant, more and more energy is allocated to photochemical reactions, until the saturation of the electron in the transport chain. From this point on, excess energy is dissipated either as heat or fluorescence (Baker, 2008; Meroni et al., 2009; Endo et al., 2014; Zha et al., 2017; Gu et al., 2019). In our case, $\Phi_{PSIImax}$ varies within a narrow range between 0.7 and 0.85 which is consistent with values found in the literature (Yamasaki et al., 2002; Baker, 2008; Dongsansuk et al., 2013; Janka et al., 2015; Zha et al., 2017; Urban et al., 2018). As a result, the mean of the observed values has been used in the MLR model (0.762).

### 3.3.3 Sub-stomatal concentration of $CO_2$

Figure 3.9 illustrates the variation of sub-stomatal $CO_2$ concentration ($C_i$) of the wheat leaves with respect to $T_{air}$. Firstly, as $T_{air}$ increases from low values up to around 22°C, $C_i$ seems to stabilise around 225 $\mu mol.mol^{-1}$. Then, $C_i$ rises to over 300 $\mu mol.mol^{-1}$ when $T_{air}$ decreases below 22°C. Low temperatures are mainly observed in the morning with the major part at relatively low values of incoming PAR. During these periods, photosynthesis (A) is weak and the stomatal conductance ($g_s$) relatively stable. Thus, the ratio $A/g_s$ is low and, according to Equation 2.8 (page 14), leads to high $C_i$ . Similar behaviours have been observed in different genotypes of rice and wheat (Huang et al., 2021). A general increase of $C_i$ is also observed when PAR decreases (data not shown) confirming the reasoning presented. On the contrary, greater values of temperatures are usually observed during mid-daytime, and correspond to high values of incoming PAR, when A stays high and stomata are steadily largely open. Hence, $A/g_s$ is changeless, leading to the stabilisation of $C_i$. Overall, the range in which $T_{air}$ is varying, with an isolated minimal value at 131 $\mu mol.mol^{-1}$ and a maximum at 375 $\mu mol.mol^{-1}$, remains relatively small. Some other studies have shown similar outputs with intercellular $CO_2$ con-

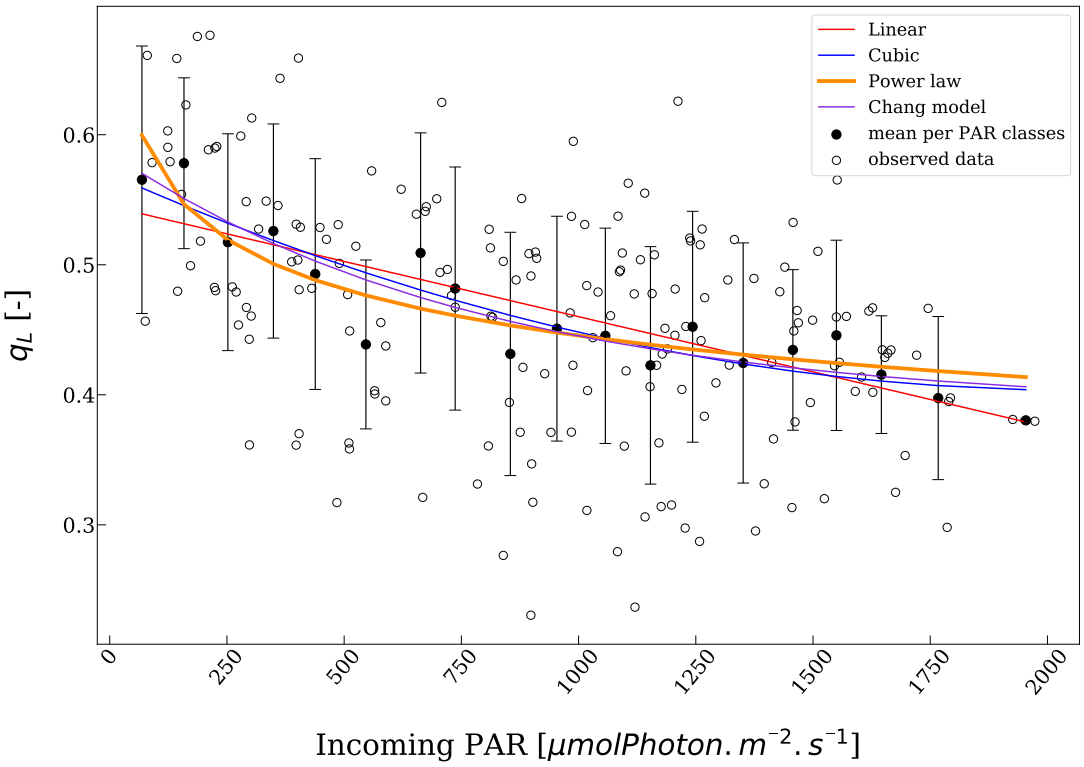


Figure 3.7: Evolution of $q_L$ with the incoming PAR. Empty dots represent punctual measurements and black dots are $q_L$ averages per PAR classes, with twelve classes of 100 $\mu molPhoton.m^{-2}.s^{-1}$ width. Linear, cubic, power law models are shown as well as the exponential model proposed by Chang et al. (2021). $R^2$ and p-values are mentioned in Appendix A.1.

centration varying slightly or increasing under stress, but still remaining in a certain range, expanding from about 150 to 300 $\mu mol.mol^{-1}$ for spring and winter wheat (Liu et al., 2016a; Chen et al., 2022). The response of $C_i$ to air temperature over the studied period has been modelled by a two-segment function: a linear $C_i$ decrease when $T_{air}$ rises from low values followed by a constant plateau for high temperatures, assumed to be equal to average $C_i$ above the breaking point temperature.

### 3.3.4 Temporal variations of factors used in the model and to estimate $SIF_{TOT\_FULL\_PSII}$

The temporal evolution of the model parameters and those used for $SIF_{TOT\_FULL\_PSII}$ estimation over the studied period is shown at Figure 3.10 and 3.11. To begin with, $\Gamma^*$ remains stable from DOY 51 to 120. From this last date, it is gradually increasing until DOY 181, occasionaly reaching high values, with a maximum of 46.279 $\mu mol.mol^{-1}$ at DOY 169. Since $\Gamma^*$ is only modelled from $T_{air}$ through a quadratic model, its fluctuations are due to the observed general increase of $T_{air}$ (cf. Figure 3.1). Next, the reflectance emitted at 760 nm (cf. Figure 3.10, C) gradually increased from DOY 60 to 110, reaching maximal value of 1, before declining to around 0.6 and finally dropping to 0.2. $R_{760}$ seems to be also affected by low $T_{air}$ values between DOY 90 and 100 but it can also be due to sensor malfunction additionally. NDVI, NIRv and $f_{APAR}$ have a bell-shaped evolution from DOY 70 to to 181 according to the development of the wheat crop canopy, as shown in Figure 3.11. The three parameters increased as of approximately DOY 70, certainly because of the substantial leaf development of the canopy, reaching a peak around DOY 120 and then steadily decreasing until DOY 181, as the crop became senescent.

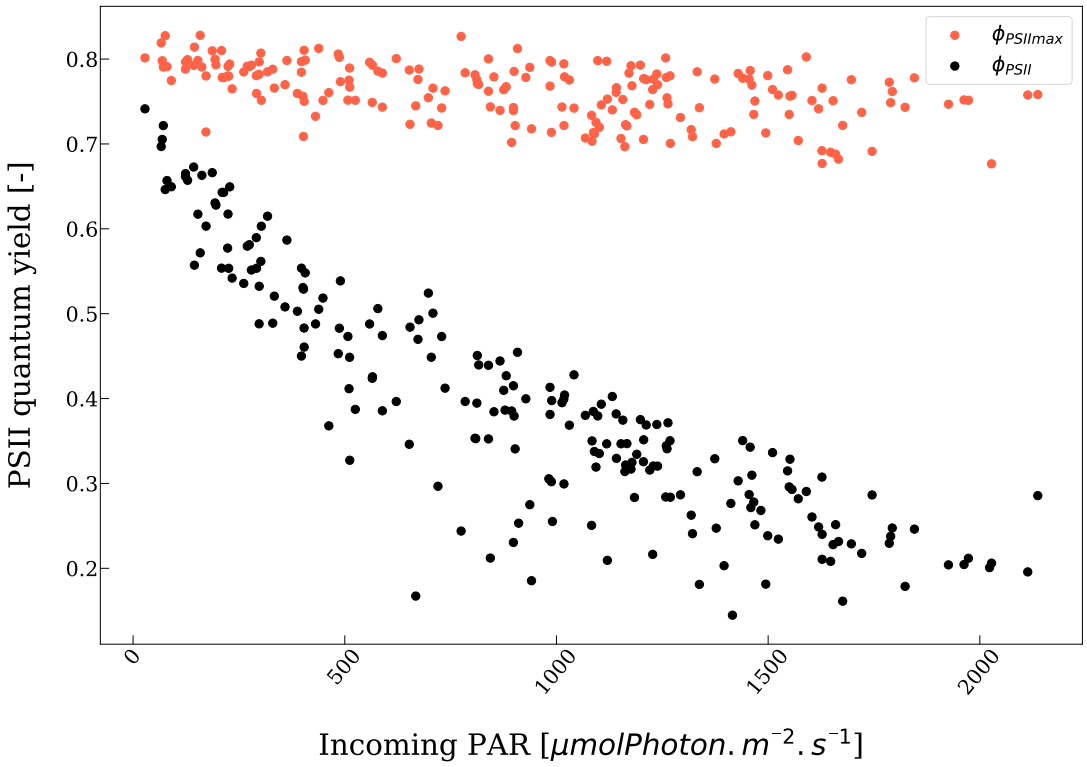


Figure 3.8: Evolution of observed photosystem II photochemical quantum yield ($\Phi_{PSII}$) and maximal photochemical quantum yield ($\Phi_{PSIImax}$) with respect to incoming PAR.

Low values of NIRv are observed between DOY 90 and 100 (cf. Figure 3.10, C). This is due to the $R_{760}$ dynamics observed over the study period (cf. Figure 3.10, C), since it is directly computed from it (see 2.6.2, page 16). Then for $f_{esc\_PC}$, computed from NIRv and $f_{APAR}$ (cf. Equation 2.16, page 16), there is a gradual rise from DOY 60 to 120 to a maximal value of 1 where plants are fully developed (cf. Figure 2.4). Afterwards, $f_{esc\_PC}$ steadily declined until approximately DOY 155 before plummeting to 0.2 at DOY 181. This last drop can be related to the beginning of the canopy senescence. A small decline of the values was observed between DOY 90 to 100, caused by the decrease NIRv during this period (cf. Figure 3.1). Compared to other studies, the overall evolution of $f_{esc\_PC}$ is quite similar even though maximal values reached are much higher, which can be due to a specific set up of the instrumentation and the wheat variety (Chang et al., 2021; Liu et al., 2022). Half-hourly $q_L$ values are retracing a diurnal behaviour with high values in the morning and at the end of the day and minimal values reached at midday. It is driven directly by daily variations of incoming PAR (Gu et al., 2019; Chang et al., 2021). Finally, an averaged $f_{PSII}$ value was used for the modelling of GPP because its temporal evolution is low in relative value (0.871, see Appendix A.4). Overall, the shape of the parameters evolution is close to what is observed in Liu et al. (2022)

## 3.4 GPP modelling performance and affecting factors

### 3.4.1 Comparison of observed and estimated GPP

Figure 3.12 shows the comparison between the modelled ($GPP_{SIF}$) and the observed ($GPP_{EC}$) for half hourly scale values. Their relationship is described by a significant positive linear correlation, with a relative mean squared error of 4.399 $\mu mol.m^{-2}.s^{-1}$. The model itself explains 40 % of the $GPP_{EC}$ variance ($R^2$-MLR = 0.410). Higher values of both GPP are found under high PAR values, which is consistent with the light response curve in Figure 3.5. However, the

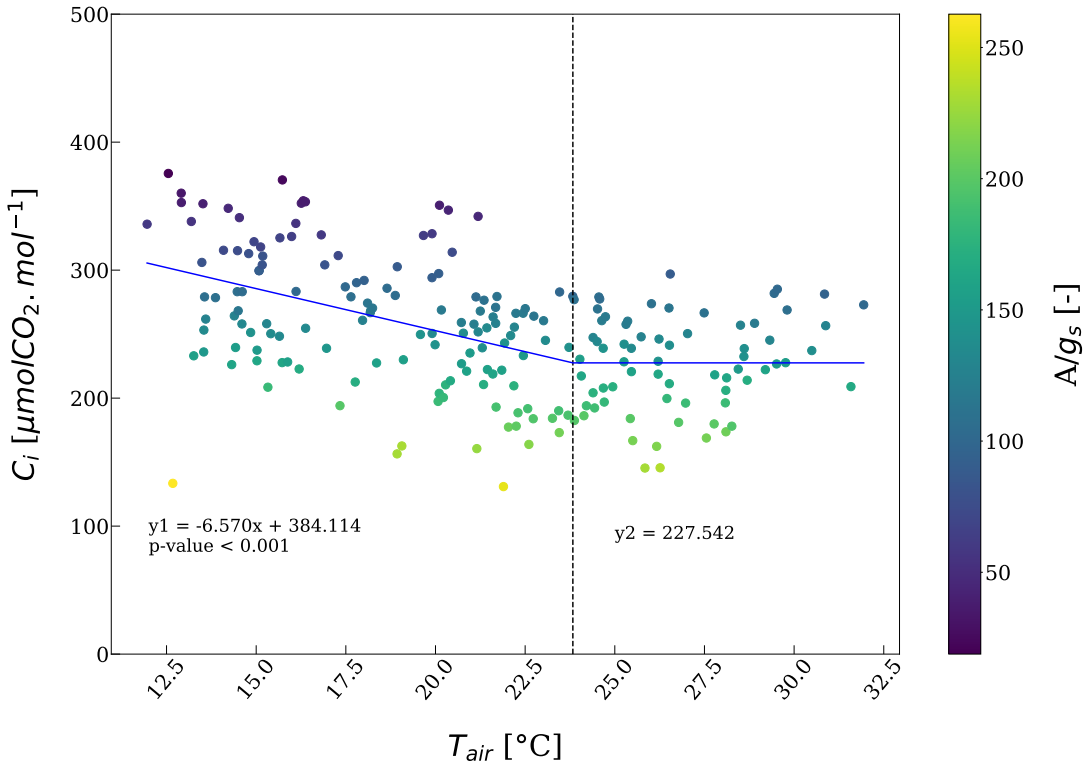


Figure 3.9: Dynamic of sub-stomatal $CO_2$ concentration ($C_i$) with respect to air temperature ($T_{air}$). For $T_{air}$ lower than 23.8 °C (corresponding to a $C_i$ of 227.542 $\mu mol.mol^{-1}$), a linear model is used to describe $C_i$ evolution, with the corresponding p-value. For air temperatures higher than this threshold, the model is the mean of the observed $C_i$ found in this part. This figure accounts for all the values of REW observed.

value of the slope of the linear relationship is 0.731 which indicates that the model does not correctly predict the sensibility of PAR. Besides, data points are quite dispersed around the 1:1 line. At the daily scale (cf. Figure 3.13), $R^2$-MLR is higher with a lower RMSE, showing that observed and estimated data are closer in average and indicating that the model has difficulties reproducing the diurnal cycle. These results are similar to Liu et al (2022) but they have found a stronger linear relationship between $GPP_{SIF}$ and $GPP_{EC}$ at half-hourly scale by using the MLR model on a wheat canopy, and an improved model performance at daily scale, which is consistent with Figure 3.13. The lower $R^2$-MLR of this study compared to Liu et al. (2022) could be explained by their distinct methodology. Although their study is based on the MLR model, NPQ and photochemical yield ($\Phi_P$) have been used instead of $q_L$ and $\Phi_{PSIImax}$, which can possibly impact the prediction performance. Moreover, in Liu et al. (2022), chloroplastic $CO_2$ concentration has been obtained from an iteration process, based notably on the net $CO_2$ assimilation rate measurements, while in our work, $C_i$, has been estimated only from air temperature. In addition, $k_{DF}$ has been fixed to 19, whereas in Liu et al. (2022), it has been set to 9. The latter seems to have a significant impact on the prediction since its value has been tuned (set to 9) to optimise the model performance. Now, regarding the reconstitution of total PSII broadband SIF, the measured SIF at 760 nm shows an almost similar temporal variation as in Liu et al. (2022), as it can bee seen in Appendix A.5. However, values of $f_{esc\_PC}$ were found higher from DOY 110 to 181, probably because of a quite smaller $f_{APAR}$ and higher NIRv. Gu et al. (2019) showed that higher $f_{esc\_PC}$ could modify the relationship between SIF and GPP. Finally, $f_{PSII}$ has been set to its mean value (0.871; Appendix A.4), while in Liu et al. (2022), it varies over the studied period staying under 0.7. All these differences, together with the climatic and environmental conditions, may influence the results, particularly the fact that the winter

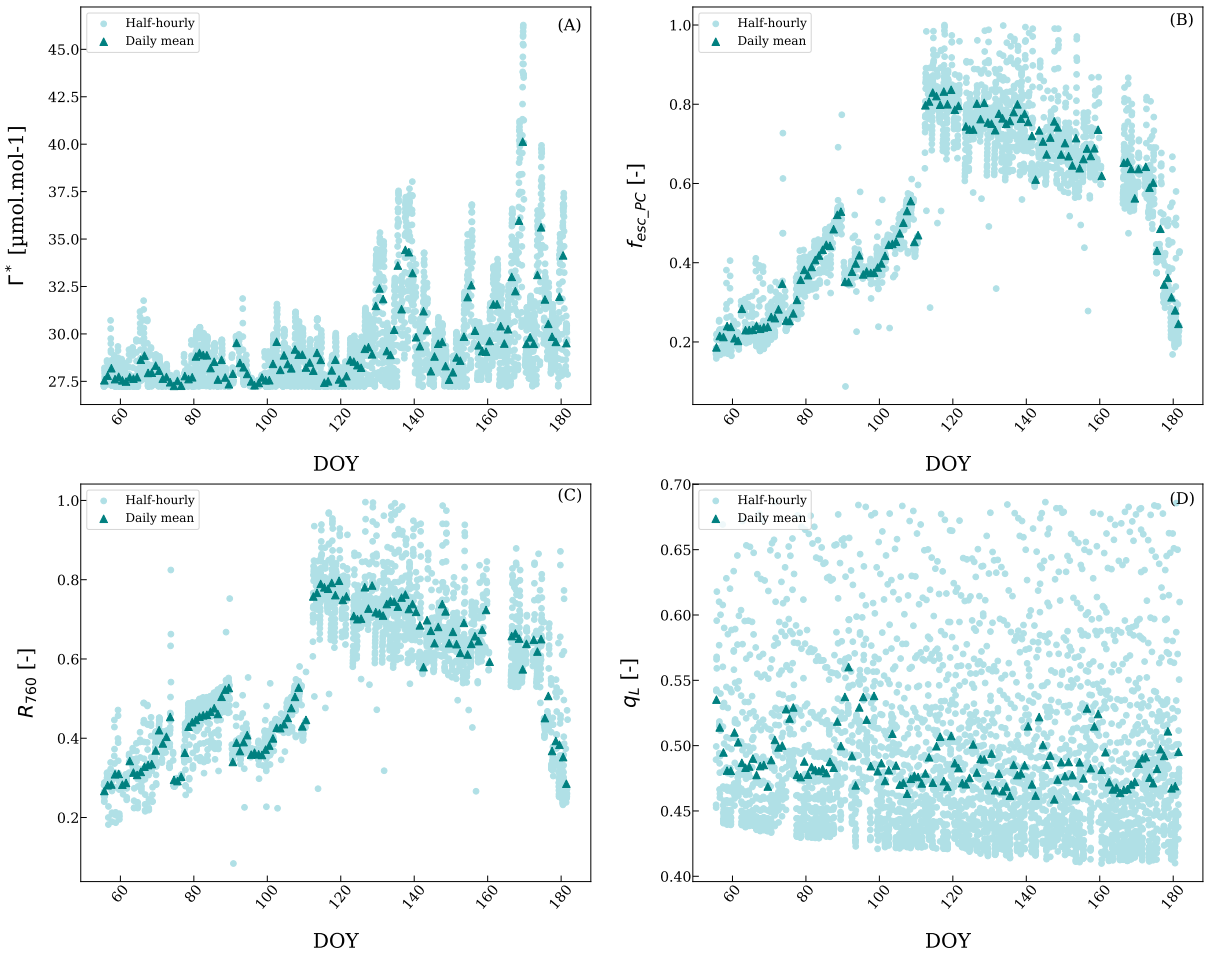


Figure 3.10: Evolution of the parameters used to estimate $GPP_{SIF}$ and $SIF_{TOT\_FULL\_PSII}$ from day of year (DOY) 51 to 181: (A) the chloroplastic $CO_2$ compensation point ($\Gamma^*$), (B) the escape probability of SIF photons from photosystem scale to canopy scale ($f_{esc\_PC}$), (C) the reflectance at 760 nm ($R_{760}$) and (D) the modelled fraction of open reaction centres from incoming PAR, ($q_L$). Light blue points indicate half-hourly estimated values and dark green triangles account for daily mean values. Only values corresponding to incoming irradiance higher than 20 $\mu molPhoton.m^{-2}.s^{-1}$ and absent precipitation are shown.

wheat canopy at Lonzée experienced an edaphic drought between DOY 120 and 181, while in Liu et al. (2022), irrigation was applied when the SWC was lower than the field capacity (60 %). A sensitivity analysis has been performed to assess the sensitivity of the model to $q_L$, $\Gamma^*$ and $C_i$ (cf. Equations 2.6 and 2.7, page 13). The results are summarised in Table 3.1 on page 33. The main factor affecting the MLR $R^2$ is $q_L$. Indeed, since it is directly multiplying SIF in the Equation 10, $q_L$ has a strong effect on J, given a certain SIF and PAR levels, and impacts the SIF-GPP relationship, as shown in Gu et al. (2019). Potentially, model predictions may be influenced by $\Gamma^*$ and $C_i$. According to Table 3.1, their variations only modified the model performance to a limited degree even though their combined fluctuations in Equation 2.7 (page 13) might affect the model performance. One should note that, as mentioned in section 2.5.1 (page 14), the presented model is valid when carbon assimilation is limited by the RuBP regeneration (Gu and Sun, 2014). Assuming this condition, the underestimation observed in Figures 3.12 and 3.13 might result from the use of the model at high PAR levels, when photosynthesis is only limited by Rubisco. Nevertheless, Liu et al. (2022) observed a strong linear relationship between estimated and observed GPP even at every PAR level. To better understand relatively poor predictions and to highlight the best using conditions of the MLR model, the relationship

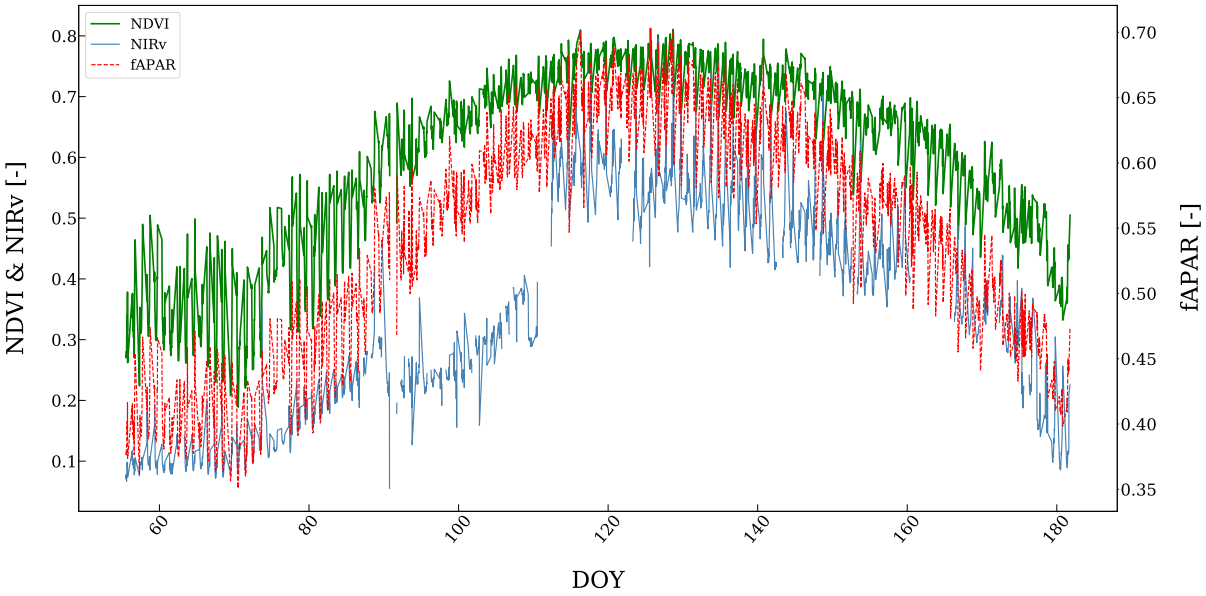


Figure 3.11: Evolution of daytime values of normalized difference vegetation index (NDVI), the product of NDVI with the reflectance at 760 nm (NIRv), and the fraction of PAR radiation absorbed by plants ($f_{APAR}$) from day of year (DOY) 51 to 181. Only values measured from 7.30 AM to 7.00 PM, accounting for incoming irradiance higher than 20 $\mu mol.m^{-2}.s^{-1}$ and non-rainy days are shown.

between SIF and GPP has been investigated with regard to phenological stages, REW and PAR levels.

### 3.4.2 SIF-GPP relationship

Different studies have shown that GPP is positively correlated with SIF, especially far-red SIF (Yang et al., 2015; Liu et al., 2016b; Goulas et al., 2017; Gu et al., 2019; Mohammed et al., 2019). Linear positive relationships have been observed for coarse temporal scales (Mohammed et al., 2019; Gao et al., 2021; Pierrat et al., 2022), under certain light conditions (Porcar-Castell et al., 2014; Zhang et al., 2016; Frankenberg and Berry, 2017; Gu et al., 2019) and, in some studies, for specific phenological stages of the vegetation (Goulas et al., 2017; Yang et al., 2018; Shen et al., 2022). Under drought stress conditions, different responses of SIF have been observed leading to a positive or negative relationship with GPP (Chen et al., 2022; Shen et al., 2022). Likewise, for heat and aerial drought stress, contradictory behaviours have been observed depending on the severity of the stress (Paul-Limoges et al., 2018; Wohlfahrt et al., 2018; Martini et al., 2022). Equally important, NPQ seems to play an important role in the relationship between fluorescence and photochemical quenching, even if the precise mechanism by which NPQ impacts the SIF-GPP relationship in unclear (Damm et al., 2010; Cendrero-Mateo et al., 2015; Yang et al., 2015; Paul-Limoges et al., 2018; Marrs et al., 2020; Porcar-Castell et al., 2021; Martini et al., 2022). The behaviour of $SIF_{TOT\_FULL\_PSII}$ with regards to both measured and predicted GPP for this study is shown at Figure 3.14. To begin with, measured GPP gradually increases until $SIF_{TOT\_FULL\_PSII}$ around 5 $\mu mol.m^{-2}.s^{-1}$ above which it is levelling out. It means that at this point, the increase in $SIF_{TOT\_FULL\_PSII}$ does not generate higher $GPP_{EC}$. On the contrary, $GPP_{SIF}$ is linearly increasing with $SIF_{TOT\_FULL\_PSII}$ and data points are less scattered. This is more noticeable at the daily scale. Although $GPP_{SIF}$ is directly computed from SIF, it demonstrates that the model does not reproduce the slight saturation that is observed with the measured GPP and thus might alter predictions. This difference between SIF relationships with both observed and predicted GPP has also been noted by Liu et al. (2022).

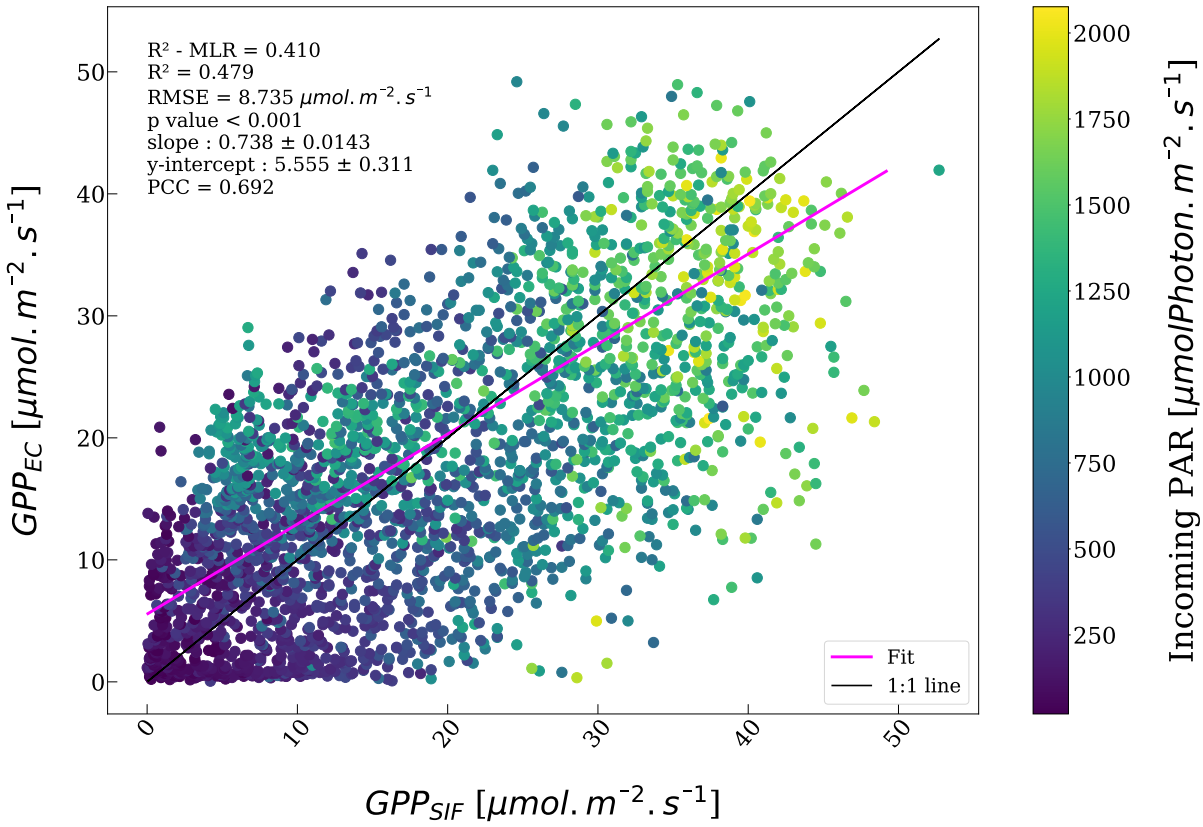


Figure 3.12: Comparison of GPP modeled by the MLR model from SIF measurements ($GPP_{SIF}$) and measured tower-based GPP ($GPP_{EC}$) at half-hourly scales. The $R^2$-MLR is the determination coefficient computed from measured and estimated values of GPP provided by the MLR model. The black line accounts for the 1:1 linear function. Only values measured accounting for incoming irradiance higher than 20 $\mu molPhoton.m^{-2}.s^{-1}$ and non-rainy days are shown.

### 3.4.3 Impacts of PAR on the SIF-GPP relationship

The $SIF_{TOT\_FULL\_PSII}$-$GPP_{EC}$ relationship for two PAR classes is shown at Figure 3.15. For PAR values higher than 1500 $\mu molPhoton.m^{-2}.s^{-1}$, the slope of the linear regression tends to zero and SIF explains a smaller proportion of the variability observed in $GPP_{EC}$ : the dynamic of both variables seems to become uncoupled. Indeed, SIF and GPP have different light responses (Porcar-Castell et al., 2014; Cendrero-Mateo et al., 2015; Gu et al., 2019). As stated before, GPP and SIF have in common the dependency on incoming PAR when this last is low. When light becomes not limiting anymore for photosynthesis processes, GPP saturates, as seen in Figure 3.5 because Rubisco limits the photosynthetic rate. Nevertheless, if SIF is not constrained by the same limiting factors, it will keep increasing, provided that the increase of NPQ is not sufficient to compensate for the saturation of carbon assimilation. More importantly, SIF seems to be strongly correlated with PAR, sometimes more than with GPP, which can potentially explain its increase at higher PAR (Yang et al., 2018; Gu et al., 2019). According to Zhang et al. (2016), who conducted a study on the Harvard forest, the loss of linearity between GPP and SIF as light intensity increases is due to the relationship between fluorescence ($\Phi_F$) and photochemical yield ($\Phi_P$) which can be either positive or negative given the situation. When light is limiting, carbon assimilation increases but $\Phi_P$ decreases, progressively leading to the GPP saturation. At the same time, $\Phi_F$ is negatively linked to $\Phi_P$ and rises because of the greater amount of energy available. Under high PAR, NPQ becomes dominant and $\Phi_F$ and $\Phi_P$ are positively correlated and decrease. These different light responses of $\Phi_F$ and $\Phi_P$ lead to the earlier saturation of

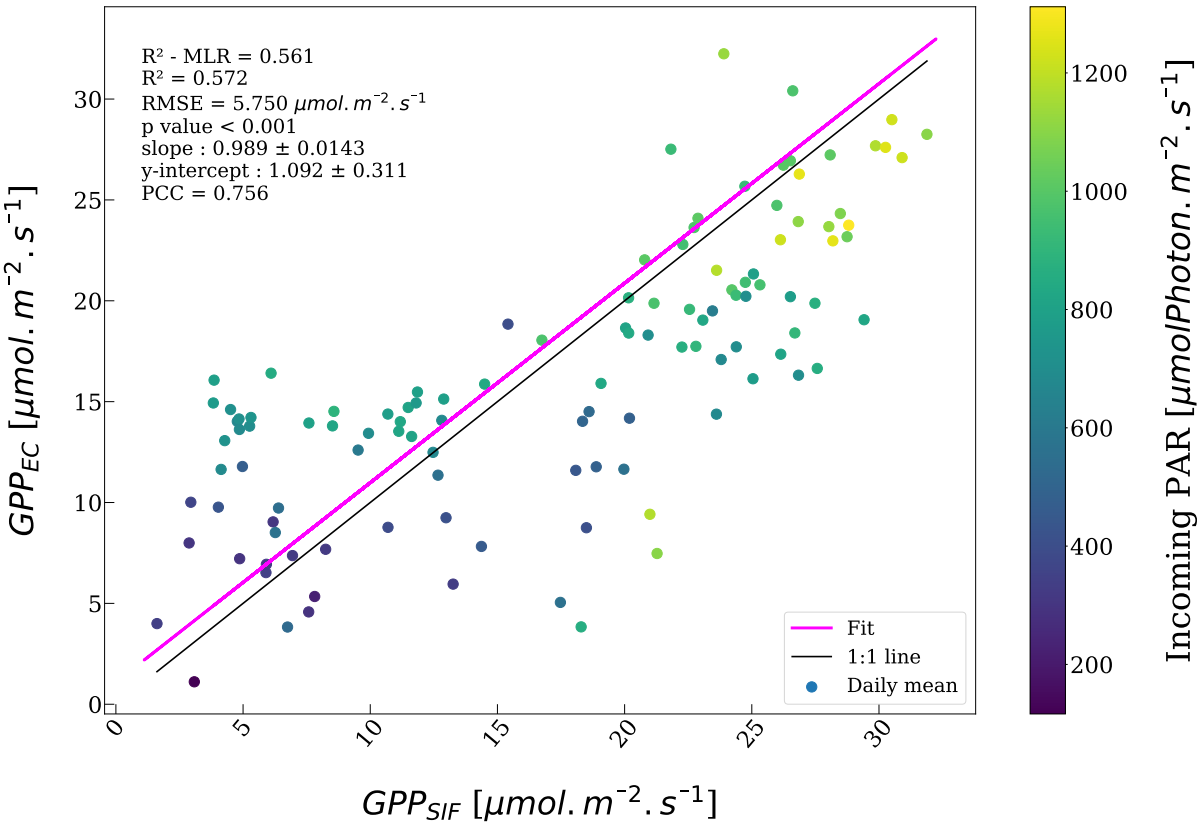


Figure 3.13: Comparison of GPP modeled thanks to the MLR model from SIF measurements ($GPP_{SIF}$) and measured tower-based GPP ($GPP_{EC}$) at daily scale. The $R^2$-MLR is the determination coefficient computed from measured and estimated values of GPP provided by the MLR model. The black line accounts for the 1:1 linear function. Only values measured from 7.30 AM to 7.00 PM, accounting for incoming irradiance higher than 20 $\mu molPhoton.m^{-2}.s^{-1}$ and non-rainy days are shown.

GPP compared to fluorescence (van der Tol et al., 2014; Cendrero-Mateo et al., 2015; Zhang et al., 2016; Porcar-Castell et al., 2021). This has not been verified due to a lack of data points. Besides, Gu et al. (2019) suggest that most of the SIF-GPP relations observed under natural conditions are linear because just a small fraction of the studied canopies (the leaves at the top) receive high intensity light during the day. Obviously, this is certainly what is observed in this case because the non-linear part is only partially observed. In the MLR model, $q_L$ should reproduce this photosynthesis saturation because it decreases and then stabilises with rising PAR (cf. Figure 3.7). Indeed, as shown by the sensitivity analysis, $q_L$ is the most impacting parameter on the model performance. Furthermore, as stated in Gu et al. (2019), $q_L$ is affecting the SIF-GPP relationship by modulating the rate of electron transport (J), thus leading to the non-linearity of the relationship. However, the decline of $q_L$ did not impact J as strongly as what is expected and J kept following SIF temporal dynamics (data not shown). Given these points and because Equation 2.7 is usually used only when carbon assimilation is limited by the RuBP regeneration, especially when this latter is itself limited by NADPH regeneration, these observations confirm that the MLR model should not be used for any other situation.

### 3.4.4 Potential effect of REW on the SIF-GPP relationship

Low values of REW ($< 0.4$) have been observed from DOY 120, after which light intensity begins to increase as well. Figure 3.16 illustrates the $GPP_{EC}$ as a function of $SIF_{TOT\_FULL\_PSII}$ with

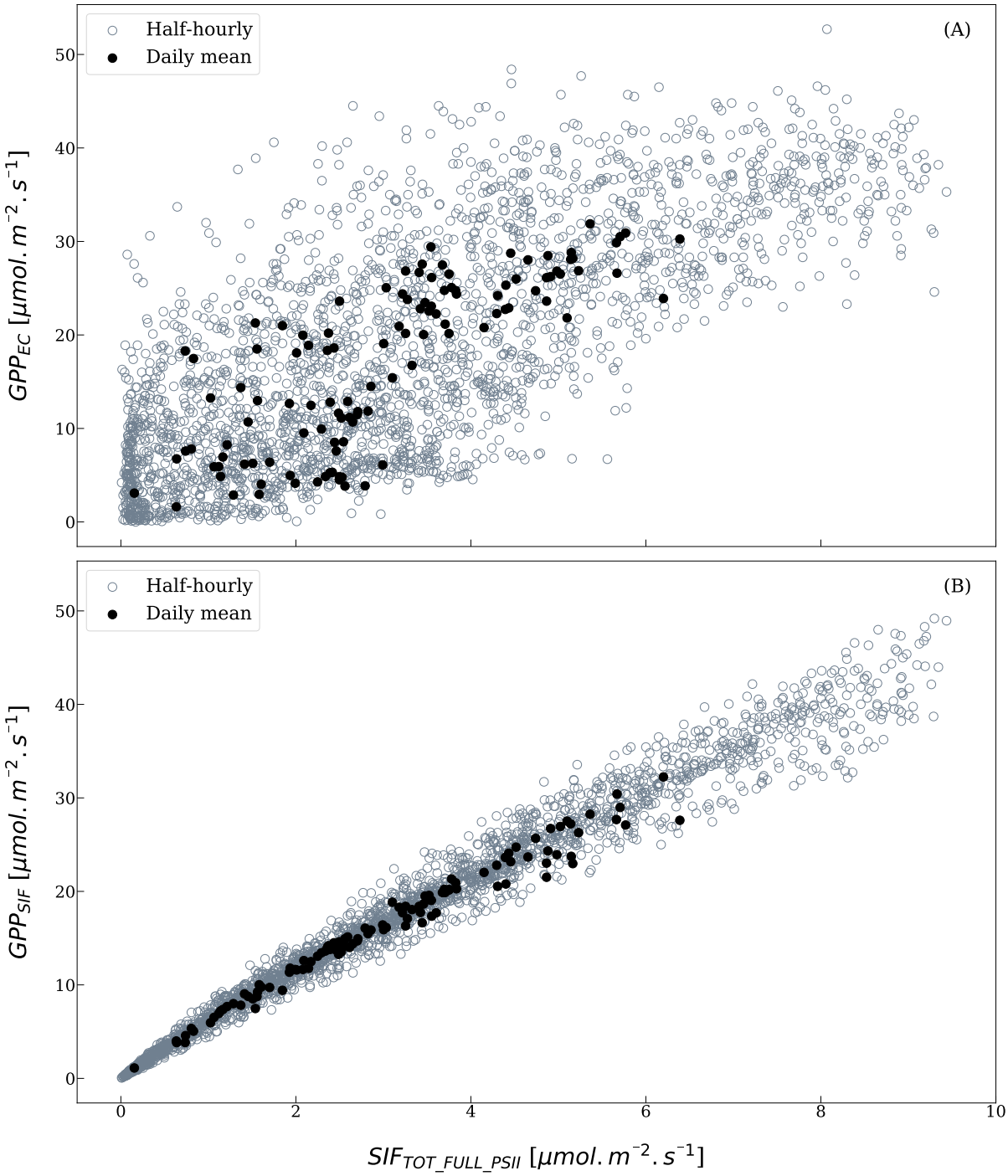


Figure 3.14: Dynamics of tower-based ($GPP_{EC}$) (A) and estimated ($GPP_{SIF}$) (B) gross primary production in function of total broadband SIF ($SIF_{TOT\_FULL\_PSII}$) from day of year (DOY) 51 to 181. Black dots represent daily mean values and blue ones half-hourly data. Only values accounting for incoming irradiance higher than 20 $\mu molPhoton.m^{-2}.s^{-1}$ and non-rainy days are shown.

Table 3.1: Mean values and $R^2$ characterising the linear regression and the MLR model resulting from the variations of $q_L$, $\Gamma^*$ and $C_i$.

| **Changes applied** | **Mean ± $\sigma$** | **$R^2$ of the MLR model** | **$R^2$ of the linear fit** |
|---|---|---|---|
| $q_L$ | | | |
| No change | 0.476 ± 0.0513 | 0.410 | 0.479 |
| + 20 % | 0.571 ± 0.0615 | 0.254 | 0.479 |
| - 20 % | 0.381 ± 0.0410 | 0.337 | 0.479 |
| $\Gamma^*$ | | | |
| No change | 29.323 ± 2.595 | 0.410 | 0.479 |
| + 20 % | 35.188 ± 3.114 | 0.401 | 0.469 |
| - 20 % | 23.458 ± 2.076 | 0.400 | 0.489 |
| $C_i$ | | | |
| No change | 295.389 ± 37.0185 | 0.410 | 0.479 |
| + 20 % | 354.466 ± 44.422 | 0.403 | 0.487 |
| - 20 % | 236.311 ± 29.615 | 0.396 | 0.466 |

regards to two REW classes. Although the parameters describing the two linear regressions are close, for REW $< 0.4$, the slope is lower, the intercept is higher and the $R^2$ indicates that $SIF_{TOT\_FULL\_PSII}$ is explaining somewhat less of $GPP_{EC}$ variability. Furthermore, their confidence intervals do not overlap each other, meaning that the two groups are relatively different. Compared to Figure 3.15, REW seems to affect less significantly the SIF-$GPP_{EC}$ relationship than PAR. This latter could have attenuated the effects of the edaphic drought, as it has already been observed in a study concerning winter wheat (Shen et al., 2022). Drought stress causes the decrease of $CO_2$ assimilation (Liu et al., 2016b; Gourlez de la Motte et al., 2020; Helm et al., 2020; Chen et al., 2022). However, it does not necessarily lead to a non-linear SIF-GPP relation. A study conducted on winter wheat showed that SIF was positively correlated to GPP under drought stress, especially during growing periods, and was thus a suitable indicator of drought-induced GPP anomalies (Shen et al., 2022). Conversely, a study conducted on maize showed that SIF increased compared to GPP under severe drought stress (Chen et al., 2021a). Indeed, measured SIF ($SIF_{TOC\_760}$) rises with REW (data not shown) which highlights the fact that both PAR and REW are affecting SIF intrinsically. To go into details, it has been shown that water stress caused an increase in NPQ, and that $\Phi_F$ shortly increased because of the decline of photochemical quantum yield under moderate stress conditions. In some cases, the NPQ rise prevents fluorescence from significantly varying or provokes its decrease, notably at canopy scale (Cendrero-Mateo et al., 2015; Helm et al., 2020; Jonard et al., 2020). Hence, these effects might participate in the observed beginning of non-linearity between $GPP_{EC}$ and $SIF_{TOT\_FULL\_PSII}$. However, some common reductions of $SIF_{TOT\_FULL\_PSII}$ and $GPP_{EC}$ are observed in Figure 3.6, for instance between DOY 140 and 160. Besides, the effect of the drought stress on $\Phi_{PSIImax}$ and $k_{DF}$ has been neglected since they were set to constant values (cf. section 2.5.1 on page 13). Generally speaking, this is certainly the interaction between different environmental factors that generated the non-linearity between $SIF_{TOT\_FULL\_PSII}$-$GPP_{EC}$ observed in Figure 3.14. Yet notwithstanding all this, it is important to note that none of the parameters, neither in the model (cf. Equations 2.6 & 2.7, 13), nor in the reconstitution of broadband SIF, directly take into account soil water content and its potential evolution for the determination of GPP modelled. It is however possible that some parameters, such as $q_L$, fluorescence intensities or,$C_i$, are impacted by water stress and thus take it into account indirectly in the GPP measured. Indeed, $C_i$ has shown to vary with soil moisture and $q_L$ can be impacted by stress (Janka et al., 2015; Liu et al., 2016b; Gu et al., 2019; Chang et al., 2021; Chen et al., 2022). Eventually, areal drought, occurring during the same period as the drought stress might have had a confounded

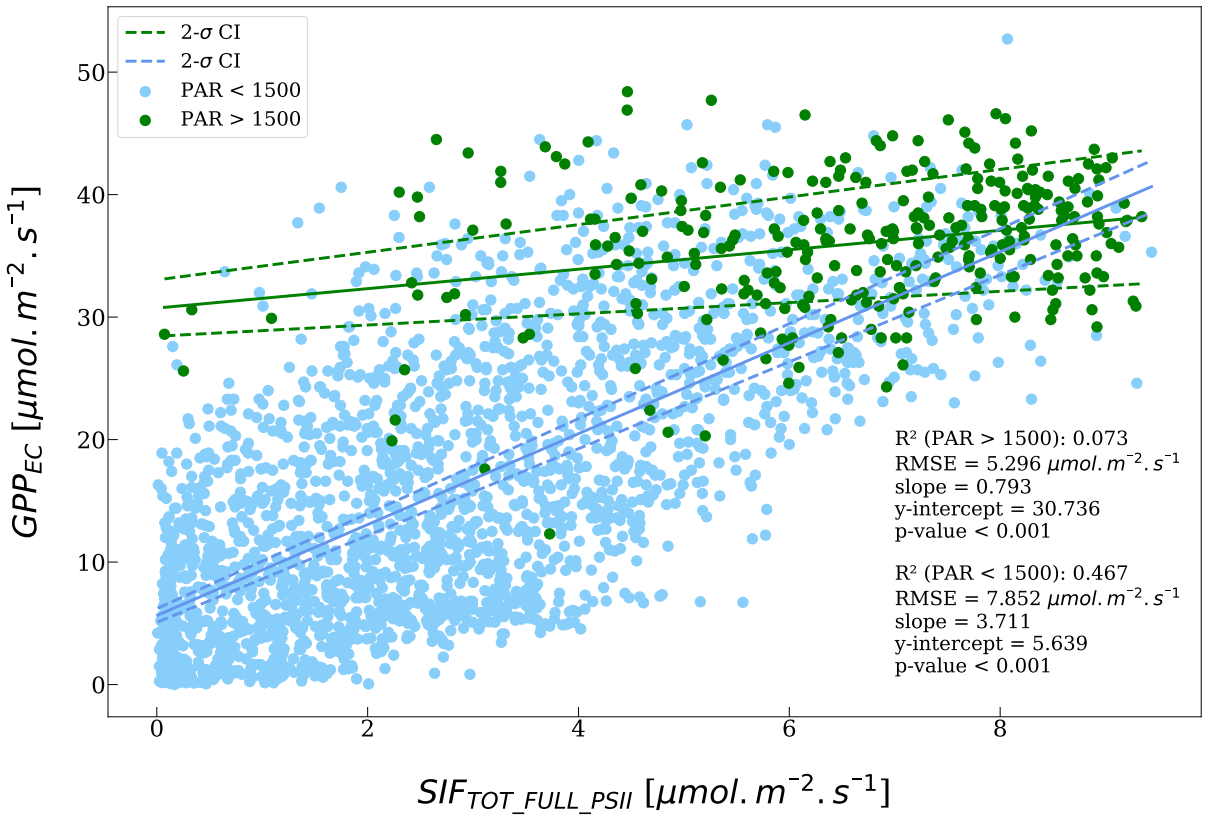


Figure 3.15: Measured tower-based GPP ($GPP_{EC}$) with regards to total broadband SIF emitted by PSII for the wheat canopy at half-hourly scale. Blue dots account for values corresponding to incoming PAR lower than the saturating value (1500 $\mu molPhoton.m^{-2}.s^{-1}$) while the green dots are values corresponding to PAR higher than the threshold. Dashed lines indicate confidence intervals for each fitted line with a confidence level of 95.45 %.

effect with low REW values and thus have influenced the SIF-GPP relationship. However, this hypothesis has not been investigated in this study.

### 3.4.5 Best conditions for using the model

As mentioned previously, phenological stages can affect the SIF-GPP relationship, notably for wheat (Goulas et al., 2017; Li et al., 2020; Shen et al., 2022). Regarding the MLR model, Liu et al. (2022) observed that the performance of the model was improved for dense canopy (NDVI > 0.6), even more under high PAR (PAR > 600 $\mu moPhotonl.m^{-2}.s^{-1}$). In the case of this study, $GPP_{SIF}$ has been compared to $GPP_{EC}$ under varying combined values of PAR, REW and GAI, with respectively, 1500 $\mu molPhoton.m^{-2}.s^{-1}$, 0.4, 6 and 2 as thresholds. The situation combining PAR lower than 1500 $\mu molPhoton.m^{-2}.s^{-1}$, REW higher than 0.4 and a GAI between 2 and 6 , provided a positive $R^2$-MLR (0.279) yet smaller than the one characterising the whole set of data (0.401) and the situation combing PAR and REW only (see Figure 3.17). Therefore, phenological stages seemed to not have a significant impact on the model performance. This could be due to the fact that $SIF_{TOT\_FULL\_PSII}$ is taken the canopy development into account through $f_{esc\_PC}$ (cf. Estimation of the total SIF emitted from PSII at 760 nm). In Figure 3.17, the comparison between $GPP_{EC}$-$GPP_{SIF}$ for different PAR and REW are illustrated. The relationships obtained are consistent with what has been observed for the SIF-GPP relationship in previous sections. Relatively poor performance of the MLR model ($R^2$-MLR < 0) was clearly observed at high PAR values, and at low REW values when light is limiting photosynthesis (PAR < 1500 $\mu molPhoton.m^{-2}.s^{-1}$). On the contrary, for REW values

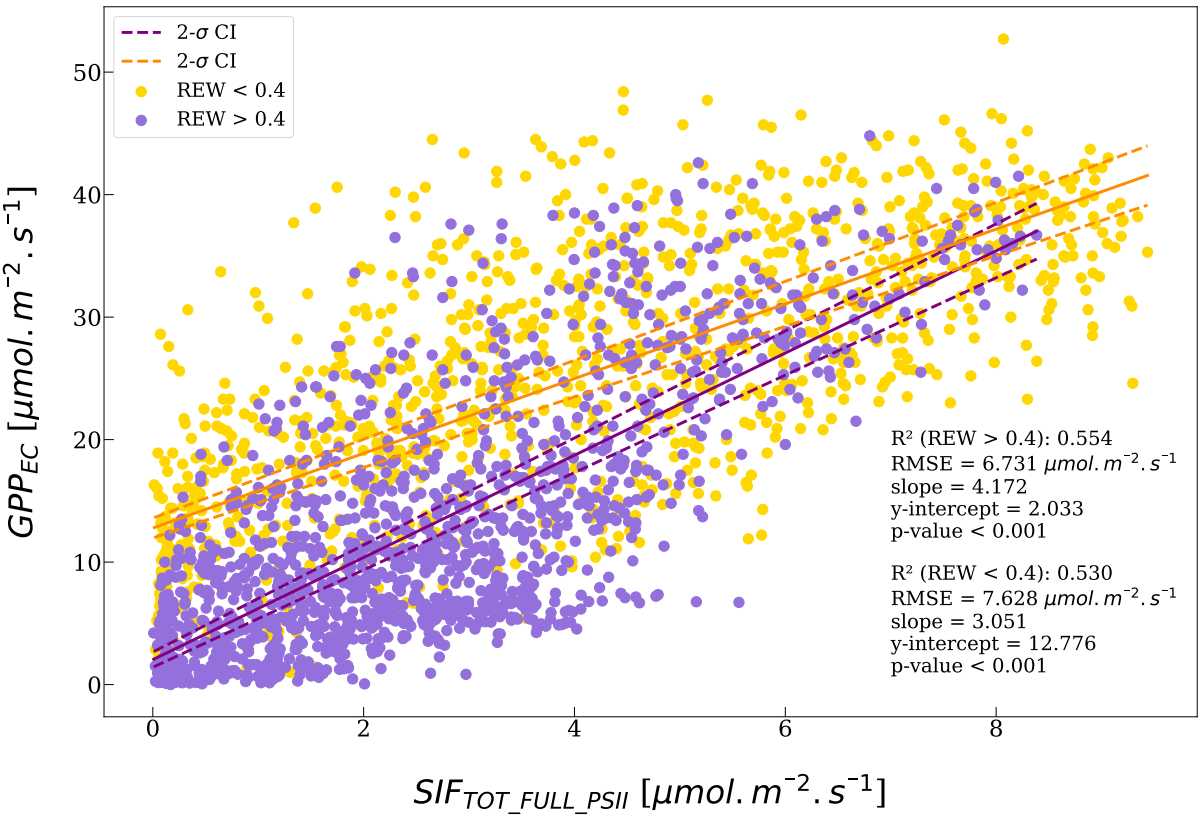


Figure 3.16: Measured tower-based GPP ($GPP_{EC}$) with regards to total broadband SIF emitted by PSII ($SIF_{TOT\_FULL\_PSII}$) for the wheat canopy at half-hourly scale. Yellow dots account for values corresponding to incoming relative extractable water (REW) lower than 0.4 while the purple dots are values corresponding to REW higher than the threshold. Dashed lines indicate confidence intervals for each fitted line with a confidence level of 95.45 %.

higher than 0.4, there is a moderate positive correlation between observed and predicted values, characterised by a linear regression of which slope is close to one, even though the $R^2$-MLR is smaller than the one describing the whole data set (0.321 compared to 0.401). Besides, compared to the situation D in Figure 3.17, data seemed slightly less scattered around the 1:1 line. This brings to light the potential impact of edaphic drought on the model performance. As can be seen from this figure, the best model performance is observed where photosynthesis is limited by the RuBP regeneration (PAR $<$ 1500 $\mu molPhoton.m^{-2}.s^{-1}$) and for REW higher than 0.4.

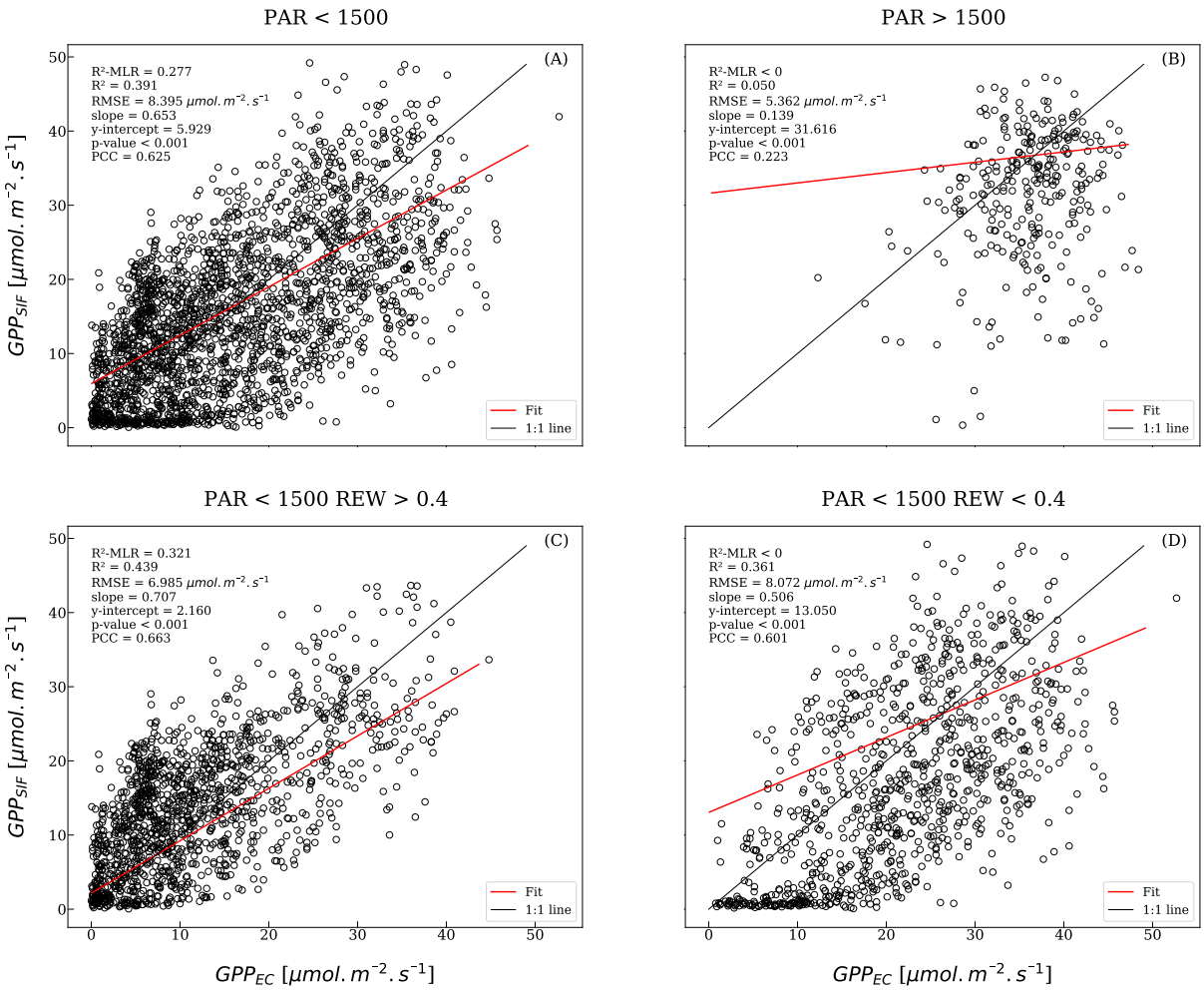


Figure 3.17: Comparison of modelled GPP ($GPP_{SIF}$) and measured GPP ($GPP_{EC}$) for four situations : (A) PAR values lower than 1500 $\mu molPhoton.m^{-2}.s^{-1}$, (B) PAR higher than 1500 $\mu molPhoton.m^{-2}.s^{-1}$, (C) PAR lower than 1500 $\mu molPhoton.m^{-2}.s^{-1}$ and REW higher than 0.4 and (D) PAR lower than 1500 $\mu molPhoton.m^{-2}.s^{-1}$ and REW lower than 0.4. PCC is the Pearson correlation coefficient computed between $GPP_{SIF}$ and $GPP_{EC}$.

# Chapter 4

# Conclusion

## 4.1 Method limitations

Different aspects of the modelling method in this study could be improved to enhance the model performance. Firstly, as mentioned in section 2.1.2 (page 8), the winter wheat canopy has been treated as a single layer. In reality, the model parameters have been determined and parametrized from leaf-level measurements on sunlit leaves located at the top of the canopy while the SIF signal measured at the top of the canopy comes from both sunlit and shaded leaves. Hence, this might have induced a potential bias in the model predictions. Indeed, for instance, Chang et al. (2021) showed that the vertical structure of the canopy has a significant impact on the diurnal response of $q_L$ to environmental factors and Liu et al. (2022) pointed out the influence of the vertical variability of NPQ. Nevertheless, for canopy-level measurements (FloX, EC), these impacts seem to be attenuated (Chang et al., 2021). Secondly, $q_L$ and NPQ have been estimated from models based only on PAR while they are actually affected by other environmental factors (Baker, 2008; Zivcak et al., 2014; Janka et al., 2015; Gu et al., 2019; Chang et al., 2021). The same conclusion applies to Ci which has only been modelled from air temperature. Last but not least, this present study has been conducted under natural conditions. As a result, the effects of incoming PAR and drougth stress on the SIF-GPP relationship and on the MLR model have been confounded and difficult to separate from each other. Therefore, studies under controlled conditions with light intensity and soil water content varying independently are needed.

## 4.2 Conclusion

Firstly, concerning the SIF-GPP relationship, a coupling between measured SIF and GPP dynamics have been observed over the study period, both driven by the evolution of the incoming PAR. This supports the fact that SIF represents an interesting indicator to estimate GPP, as suggested by many studies. However, for winter wheat canopy and the specific climatic conditions observed in this study, the performance of the MLR model was found to be quite weaker at half-hourly scale than at the daily scale. In reality, the SIF-GPP relationship, underlying the modelling of GPP, was only correctly reproduced under certain environmental conditions. Among them, incoming light was found to be the main impacting factor for the SIF-GPP relationship. Indeed, under low light intensities, the observed positive correlation between SIF and GPP highlighted the fact that using the rate of the linear electron transport J to predict GPP is only relevant when photosynthesis is limited by light intensity, which is in agreement with the assumption linked to the FvCB model included in the MLR model (cf. Equation 2.7, page 13). Then, SIF and GPP tend to be positively linearly linked under high values of soil water content. Besides, no significant effect of phenological stages have been observed on the model performance. Secondly, the evolution of model parameters with canopy development and incoming light are consistent with what has already been described in the literature. In particular, a first attempt of parametrizations of non-photochemical quenching and the fraction of open reaction centres from incoming light has been performed. In conclusion, the MLR model offers great opportunities to mechanistically model photosynthesis for winter wheat under temperate maritime climate. Nonetheless, further studies are needed to improve its performances and to parametrize more accurately its parameters, notably regarding vertical canopy structure. Besides, experiments under controlled conditions may help to bring to light the impacts of environmental factors on the model and the parameters dynamics. Overall, to expand the use of this model to larger scales, it needs to be applied and assessed under varying climatic conditions and for different plant species, all the more under this context of global climate change.

# Bibliography


Aasen, H., Van Wittenberghe, S., Sabater Medina, N., Damm, A., Goulas, Y., Wieneke, S., Hueni, A., Malenovský, Z., Alonso, L., Pacheco-Labrador, J., Cendrero-Mateo, M.P., Tomelleri, E., Burkart, A., Cogliati, S., Rascher, U., Mac Arthur, A., 2019. Sun-Induced Chlorophyll Fluorescence II: Review of Passive Measurement Setups, Protocols, and Their Application at the Leaf to Canopy Level. Remote Sensing 11, 927. URL: https://www.mdpi.com/2072-4292/11/8/927, doi:10.3390/rs11080927. number: 8 Publisher: Multidisciplinary Digital Publishing Institute.

Ahmad, P., 2016. Water Stress and Crop Plants: A Sustainable Approach. John Wiley & Sons. Google-Books-ID: 2lRRDAAAQBAJ.

Allan, R., Pereira, L., Smith, M., 1998. Crop evapotranspiration-Guidelines for computing crop water requirements-FAO Irrigation and drainage paper 56. volume 56.

Aubinet, M., Moureaux, C., Bodson, B., Dufranne, D., Heinesch, B., Suleau, M., Vancutsem, F., Vilret, A., 2009. Carbon sequestration by a crop over a 4-year sugar beet/winter wheat/seed potato/winter wheat rotation cycle. Agricultural and Forest Meteorology 149, 407–418. URL: https://www.sciencedirect.com/science/article/pii/S0168192308002475, doi:10.1016/j.agrformet.2008.09.003.

Aubinet, M., Vesala, T., Papale, D., 2012. Eddy Covariance: A Practical Guide to Measurement and Data Analysis. Springer Netherlands, Dordrecht. URL: http://link.springer.com/10.1007/978-94-007-2351-1, doi:10.1007/978-94-007-2351-1.

Baker, N.R., 2008. Chlorophyll Fluorescence: A Probe of Photosynthesis In Vivo. Annu. Rev. Plant Biol. 59, 89–113. URL: https://www.annualreviews.org/doi/10.1146/annurev.arplant.59.032607.092759, doi:10.1146/annurev.arplant.59.032607.092759.

Beer, C., Reichstein, M., Tomelleri, E., Ciais, P., Jung, M., Carvalhais, N., Rödenbeck, C., Arain, M.A., Baldocchi, D., Bonan, G.B., Bondeau, A., Cescatti, A., Lasslop, G., Lindroth, A., Lomas, M., Luyssaert, S., Margolis, H., Oleson, K.W., Roupsard, O., Veenendaal, E., Viovy, N., Williams, C., Woodward, F.I., Papale, D., 2010. Terrestrial Gross Carbon Dioxide Uptake: Global Distribution and Covariation with Climate. Science 329, 834–838. URL: https://www.science.org/doi/10.1126/science.1184984, doi:10.1126/science.1184984. publisher: American Association for the Advancement of Science.

Belgium, I., . ICOS Belgium : Lonzée. URL: https://www.icos-belgium.be/ESLonzee.php#Lonzee.

Bernacchi, C.J., Singsaas, E.L., Pimentel, C., Portis Jr, A.R., Long, S.P., 2001. Improved temperature response functions for models of Rubisco-limited photosynthesis. Plant, Cell & Environment 24, 253–259. URL: https://onlinelibrary.wiley.com/doi/abs/10.1111/j.1365-3040.2001.00668.x, doi:10.1111/j.1365-3040.2001.00668.x. _eprint: https://onlinelibrary.wiley.com/doi/pdf/10.1111/j.1365-3040.2001.00668.x.

Buysse, P., Bodson, B., Debacq, A., De Ligne, A., Heinesch, B., Manise, T., Moureaux, C., Aubinet, M., 2017. Carbon budget measurement over 12 years at a crop production site in the silty-loam region in Belgium. Agricultural and Forest Meteorology 246, 241–255. URL: https://linkinghub.elsevier.com/retrieve/pii/S0168192317302204, doi:10.1016/j.agrformet.2017.07.004.

Campbell Scientific, I., 2016. EnviroSCAN Soil Water Content Profile Probes Intruction manual .

Cendrero-Mateo, M.P., Carmo-Silva, A.E., Porcar-Castell, A., Hamerlynck, E.P., Papuga, S.A., Moran, M.S., 2015. Dynamic response of plant chlorophyll fluorescence to light, water and nutrient availability. Functional Plant Biol. 42, 746. URL: http://www.publish.csiro.au/?paper=FP15002, doi:10.1071/FP15002.

Chang, C.Y., Wen, J., Han, J., Kira, O., LeVonne, J., Melkonian, J., Riha, S.J., Skovira, J., Ng, S., Gu, L., Wood, J.D., Näthe, P., Sun, Y., 2021. Unpacking the drivers of diurnal dynamics of sun-induced chlorophyll fluorescence (SIF): Canopy structure, plant physiology, instrument configuration and retrieval methods. Remote Sensing of Environment 265, 112672. URL: https://www.sciencedirect.com/science/article/pii/S0034425721003928, doi:10.1016/j.rse.2021.112672.

Chen, F., Wang, H., Zhao, F., Wang, R., Qi, Y., Zhang, K., Zhao, H., Tang, G., Yang, Y., 2022. The Response Mechanism and Threshold of Spring Wheat to Rapid Drought. Atmosphere 13. doi:10.3390/atmos13040596.

Chen, J., Liu, X., Du, S., Ma, Y., Liu, L., 2021a. Effects of Drought on the Relationship Between Photosynthesis and Chlorophyll Fluorescence for Maize. IEEE Journal of Selected Topics in Applied Earth Observations and Remote Sensing 14, 11148–11161. doi:10.1109/JSTARS.2021.3123111. conference Name: IEEE Journal of Selected Topics in Applied Earth Observations and Remote Sensing.

Chen, Y., Zhao, Q., Le, Y., Zhu, Z., Yan, Q., 2021b. Comparison of Solar-Induced Chlorophyll Fluorescence and Light Use Efficiency Models for Gross Primary Productivity Estimation on Three Mid-latitude Grassland Sites in North America. PFG - Journal of Photogrammetry, Remote Sensing and Geoinformation Science 89, 549–562. doi:10.1007/s41064-021-00171-y.

Damm, A., Elbers, J., Erler, A., Gioli, B., Hamdi, K., Hutjes, R., Kosvancova, M., Meroni, M., Miglietta, F., Moersch, A., Moreno, J., Schickling, A., Sonnenschein, R., Udelhoven, T., Van Der LINDEN, S., Hostert, P., Rascher, U., 2010. Remote sensing of sun-induced fluorescence to improve modeling of diurnal courses of gross primary production (GPP). Global Change Biology 16, 171–186. URL: https://onlinelibrary.wiley.com/doi/abs/10.1111/j.1365-2486.2009.01908.x, doi:10.1111/j.1365-2486.2009.01908.x. _eprint: https://onlinelibrary.wiley.com/doi/pdf/10.1111/j.1365-2486.2009.01908.x.

De Cannière, S., Herbst, M., Vereecken, H., Defourny, P., Jonard, F., 2021. Constraining water limitation of photosynthesis in a crop growth model with sun-induced chlorophyll fluorescence. Remote Sensing of Environment 267, 112722. URL: https://linkinghub.elsevier.com/retrieve/pii/S0034425721004429, doi:10.1016/j.rse.2021.112722.

Dongsansuk, A., Lütz, C., Neuner, G., 2013. Effects of temperature and irradiance on quantum yield of PSII photochemistry and xanthophyll cycle in a tropical and a temperate species. Photosynthetica 51, 13–21. URL: https://doi.org/10.1007/s11099-012-0070-2, doi:10.1007/s11099-012-0070-2.

Dusenge, M.E., Duarte, A.G., Way, D.A., 2019. Plant carbon metabolism and climate change: elevated CO2 and temperature impacts on photosynthesis, photorespiration and respiration. New Phytologist 221, 32–49. URL: https://onlinelibrary.wiley.com/doi/abs/10.1111/nph.15283, doi:10.1111/nph.15283. _eprint: https://onlinelibrary.wiley.com/doi/pdf/10.1111/nph.15283.

United Nations Department of Economic and Social Affairs, P.D., 2022. World Population Prospects 2022: Summary of Results. Technical Report. New york.

Endo, T., Uebayashi, N., Ishida, S., Ikeuchi, M., Sato, F., 2014. Light energy allocation at PSII under field light conditions: How much energy is lost in NPQ-associated dissipation? Plant Physiology and Biochemistry 81, 115–120. URL: https://www.sciencedirect.com/science/article/pii/S0981942814000977, doi:10.1016/j.plaphy.2014.03.018.

Fakhet, D., Morales, F., Jauregui, I., Erice, G., Aparicio-Tejo, P.M., González-Murua, C., Aroca, R., Irigoyen, J.J., Aranjuelo, I., 2021. Short-Term Exposure to High Atmospheric Vapor Pressure Deficit (VPD) Severely Impacts Durum Wheat Carbon and Nitrogen Metabolism in the Absence of Edaphic Water Stress. Plants 10, 120. URL: https://www.mdpi.com/2223-7747/10/1/120, doi:10.3390/plants10010120. number: 1 Publisher: Multidisciplinary Digital Publishing Institute.

FAO, 2021. The impact of disasters and crises on agriculture and food security: 2021. FAO. URL: http://www.fao.org/documents/card/en/c/cb3673en, doi:10.4060/cb3673en.

FAO, 2022. Crop Prospects and Food Situation #1, March 2022. FAO. URL: http://www.fao.org/documents/card/en/c/cb8893en, doi:10.4060/cb8893en.

Farquhar, G.D., von Caemmerer, S., Berry, J.A., 1980. A biochemical model of photosynthetic CO2 assimilation in leaves of C3 species. Planta 149, 78–90. URL: https://doi.org/10.1007/BF00386231, doi:10.1007/BF00386231.

Feng, H., Xu, T., Liu, L., Zhou, S., Zhao, J., Liu, S., Xu, Z., Mao, K., He, X., Zhu, Z., Chai, L., 2021. Modeling Transpiration with Sun-Induced Chlorophyll Fluorescence Observations via Carbon-Water Coupling Methods. Remote Sensing 13, 804. URL: https://www.mdpi.com/2072-4292/13/4/804, doi:10.3390/rs13040804.

Fischer, E.M., Knutti, R., 2015. Anthropogenic contribution to global occurrence of heavy-precipitation and high-temperature extremes. Nature Clim Change 5, 560–564. URL: http://www.nature.com/articles/nclimate2617, doi:10.1038/nclimate2617.

FORUM, F., 2009. Global Forum on Food Security and Nutrition : Global agriculture towards 2050.

Frankenberg, C., Berry, J., 2017. Solar Induced Chlorophyll Fluorescence: Origins, Relation to Photosynthesis and Retrieval, in: Reference Module in Earth Systems and Environmental Sciences. doi:10.1016/B978-0-12-409548-9.10632-3. journal Abbreviation: Reference Module in Earth Systems and Environmental Sciences.

Galmés, J., Aranjuelo, I., Medrano, H., Flexas, J., 2013. Variation in Rubisco content and activity under variable climatic factors. Photosynth Res 117, 73–90. URL: https://doi.org/10.1007/s11120-013-9861-y, doi:10.1007/s11120-013-9861-y.

Gao, H., Liu, S., Lu, W., Smith, A., Valbuena, R., Yan, W., Wang, Z., Xiao, L., Peng, X., Li, Q., Feng, Y., McDonald, M., Pagella, T., Liao, J., Wu, Z., Zhang, G., 2021. Global analysis of the relationship between reconstructed solar-induced chlorophyll fluorescence (Sif) and gross primary production (gpp). Remote Sensing 13. doi:10.3390/rs13142824.

Gielen, B., Acosta, M., Altimir, N., Buchmann, N., Cescatti, A., Ceschia, E., Fleck, S., Hörtnagl, L., Klumpp, K., Kolari, P., Lohila, A., Loustau, D., Marańon-Jimenez, S., Manise, T., Matteucci, G., Merbold, L., Metzger, C., Moureaux, C., Montagnani, L., Nilsson, M.B., Osborne, B., Papale, D., Pavelka, M., Saunders, M., Simioni, G., Soudani, K., Sonnentag, O., Tallec, T., Tuittila, E.S., Peichl, M., Pokorny, R., Vincke, C., Wohlfahrt, G., 2018. Ancillary vegetation measurements at ICOS ecosystem stations. International Agrophysics 32, 645–664. URL: http://archive.sciendo.com/INTAG/intag.2017.32.issue-4/intag-2017-0048/intag-2017-0048.pdf, doi:10.1515/intag-2017-0048.

Gonsamo, A., Chen, J.M., 2018. 3.11 - Vegetation Primary Productivity, in: Liang, S. (Ed.), Comprehensive Remote Sensing. Elsevier, Oxford, pp. 163–189. URL: https://www.sciencedirect.com/science/article/pii/B9780124095489105354, doi:10.1016/B978-0-12-409548-9.10535-4.

Goulas, Y., Fournier, A., Daumard, F., Champagne, S., Ounis, A., Marloie, O., Moya, I., 2017. Gross Primary Production of a Wheat Canopy Relates Stronger to Far Red Than to Red Solar-Induced Chlorophyll Fluorescence. Remote Sensing 9, 97. URL: https://www.mdpi.com/2072-4292/9/1/97, doi:10.3390/rs9010097. number: 1 Publisher: Multidisciplinary Digital Publishing Institute.

Gu, L., Han, J., Wood, J.D., Chang, C.Y., Sun, Y., 2019. Sun-induced Chl fluorescence and its importance for biophysical modeling of photosynthesis based on light reactions. New Phytol 223, 1179–1191. URL: https://onlinelibrary.wiley.com/doi/10.1111/nph.15796, doi:10.1111/nph.15796.

Gu, L., Sun, Y., 2014. Artefactual responses of mesophyll conductance to CO2 and irradiance estimated with the variable J and online isotope discrimination methods. Plant, Cell & Environment 37, 1231–1249. URL: https://onlinelibrary.wiley.com/doi/abs/10.1111/pce.12232, doi:10.1111/pce.12232. _eprint: https://onlinelibrary.wiley.com/doi/pdf/10.1111/pce.12232.

Guanter, L., Zhang, Y., Jung, M., Joiner, J., Voigt, M., Berry, J.A., Frankenberg, C., Huete, A.R., Zarco-Tejada, P., Lee, J.E., Moran, M.S., Ponce-Campos, G., Beer, C., Camps-Valls, G., Buchmann, N., Gianelle, D., Klumpp, K., Cescatti, A., Baker, J.M., Griffis, T.J., 2014. Global and time-resolved monitoring of crop photosynthesis with chlorophyll fluorescence. Proceedings of the National Academy of Sciences 111, E1327–E1333. URL: https://www.pnas.org/doi/abs/10.1073/pnas.1320008111, doi:10.1073/pnas.1320008111. publisher: Proceedings of the National Academy of Sciences.

Hall, D.O., Rao, K.K., 1999. Photosynthesis. Studies in biology. 6th ed ed., Cambridge University Press, Cambridge, UK ; New York.

Hansen, S., Jensen, H.E., Nielsen, N.E., Svendsen, H., 1991. Simulation of nitrogen dynamics and biomass production in winter wheat using the Danish simulation model DAISY. Fertilizer Research 27, 245–259. URL: https://doi.org/10.1007/BF01051131, doi:10.1007/BF01051131.

Helm, L.T., Shi, H., Lerdau, M.T., Yang, X., 2020. Solar-induced chlorophyll fluorescence and short-term photosynthetic response to drought. Ecol Appl 30. URL: https://onlinelibrary.wiley.com/doi/10.1002/eap.2101, doi:10.1002/eap.2101.

Horton, P., 2013. Dynamic Behavior of Photosystem II Light Harvesting, in: Lennarz, W.J., Lane, M.D. (Eds.), Encyclopedia of Biological Chemistry (Second Edition). Academic Press, Waltham, pp. 178–183. URL: https://www.sciencedirect.com/science/article/pii/B9780123786302001651, doi:10.1016/B978-0-12-378630-2.00165-1.

Huang, G., Yang, Y., Zhu, L., Peng, S., Li, Y., 2021. Temperature responses of photosynthesis and stomatal conductance in rice and wheat plants. Agricultural and Forest Meteorology 300, 108322. URL: https://www.sciencedirect.com/science/article/pii/S0168192321000058, doi:10.1016/j.agrformet.2021.108322.

ICOS, . ICOS Belgium. URL: https://www.icos-belgium.be/ESLonzee.php.

IRM, a. IRM - Vague de chaleur. URL: https://www.meteo.be/fr/infos/dico-meteo/vague-de-chaleur.

IRM, b. Statistiques climatiques des communes belges, Gembloux. Technical Report. URL: www.meteo.be.

Janka, E., Körner, O., Rosenqvist, E., Ottosen, C.O., 2015. Using the quantum yields of photosystem II and the rate of net photosynthesis to monitor high irradiance and temperature stress in chrysanthemum (Dendranthema grandiflora). Plant Physiology and Biochemistry 90, 14–22. URL: https://www.sciencedirect.com/science/article/pii/S0981942815000509, doi:10.1016/j.plaphy.2015.02.019.

Jiang, P., Cai, F., Zhao, Z.Q., Meng, Y., Gao, L.Y., Zhao, T.H., 2018. Physiological and Dry Matter Characteristics of Spring Maize in Northeast China under Drought Stress. Water 10, 1561. URL: http://www.mdpi.com/2073-4441/10/11/1561, doi:10.3390/w10111561.

Jonard, F., De Cannière, S., Brüggemann, N., Gentine, P., Short Gianotti, D., Lobet, G., Miralles, D., Montzka, C., Pagán, B., Rascher, U., Vereecken, H., 2020. Value of sun-induced chlorophyll fluorescence for quantifying hydrological states and fluxes: Current status and challenges. Agricultural and Forest Meteorology 291, 108088. URL: https://linkinghub.elsevier.com/retrieve/pii/S0168192320301908, doi:10.1016/j.agrformet.2020.108088.

Kasajima, I., Takahara, K., Kawai-Yamada, M., Uchimiya, H., 2009. Estimation of the Relative Sizes of Rate Constants for Chlorophyll De-excitation Processes Through Comparison of Inverse Fluorescence Intensities. Plant and Cell Physiology 50, 1600–1616. URL: https://academic.oup.com/pcp/article-lookup/doi/10.1093/pcp/pcp102, doi:10.1093/pcp/pcp102.

Katul, G., Manzoni, S., Palmroth, S., Oren, R., 2010. A stomatal optimization theory to describe the effects of atmospheric CO2 on leaf photosynthesis and transpiration. Ann Bot 105, 431–442. URL: https://www.ncbi.nlm.nih.gov/pmc/articles/PMC2826246/, doi:10.1093/aob/mcp292.

Kirschbaum, M.U.F., 2004. Direct and Indirect Climate Change Effects on Photosynthesis and Transpiration. Plant Biol (Stuttg) 6, 242–253. URL: http://www.thieme-connect.de/DOI/DOI?10.1055/s-2004-820883, doi:10.1055/s-2004-820883. publisher: Georg Thieme Verlag Stuttgart KG · New York.

Kramer, D.M., Johnson, G., Kiirats, O., Edwards, G.E., 2004. New Fluorescence Parameters for the Determination of QA Redox State and Excitation Energy Fluxes. Photosynthesis Research 79, 209. URL: https://doi.org/10.1023/B:PRES.0000015391.99477.0d, doi:10.1023/B:PRES.0000015391.99477.0d.

Köppen, W., 1884. Die Wärmezonen der Erde, nach der Dauer der heissen, gemässigten und kalten Zeit und nach der Wirkung der Wärme auf die organische Welt betrachtet. Meteorol. Z. 1, 215–226.

Li, J., Zhang, Y., Gu, L., Li, Z., Li, J., Zhang, Q., Zhang, Z., Song, L., 2020. Seasonal variations in the relationship between sun-induced chlorophyll fluorescence and photosynthetic capacity from the leaf to canopy level in a rice crop. Journal of Experimental Botany 71, 7179–7197. URL: https://academic.oup.com/jxb/article/71/22/7179/5903319, doi:10.1093/jxb/eraa408.

Li, X., Xiao, J., 2022. TROPOMI observations allow for robust exploration of the relationship between solar-induced chlorophyll fluorescence and terrestrial gross primary production. Remote Sensing of Environment 268, 112748. URL: https://www.sciencedirect.com/science/article/pii/S0034425721004685, doi:10.1016/j.rse.2021.112748.

LI-COR Biosciences, I., 2011. Using the LI-6400 / LI-6400XT Portable Photosynthesis System.

Liang, S., Wang, J., 2020. Chapter 15 - Estimate of vegetation production of terrestrial ecosystem, in: Advanced Remote Sensing (Second Edition). Academic Press, pp. 581–620. URL: https://www.sciencedirect.com/science/article/pii/B9780128158265000155, doi:10.1016/B978-0-12-815826-5.00015-5.

Liu, E.K., Mei, X.R., Yan, C.R., Gong, D.Z., Zhang, Y.Q., 2016a. Effects of water stress on photosynthetic characteristics, dry matter translocation and WUE in two winter wheat genotypes. Agricultural Water Management 167, 75–85. URL: https://www.sciencedirect.com/science/article/pii/S0378377415301979, doi:10.1016/j.agwat.2015.12.026.

Liu, L., Liu, X., Guan, L., 2016b. Uncertainties in linking solar-induced chlorophyll fluorescence to plant photosynthetic activities, pp. 4414–4417. doi:10.1109/IGARSS.2016.7730150.

Liu, Z., Zhao, F., Liu, X., Yu, Q., Wang, Y., Peng, X., Cai, H., Lu, X., 2022. Direct estimation of photosynthetic CO2 assimilation from solar-induced chlorophyll fluorescence (SIF). Remote Sensing of Environment 271, 112893. URL: https://linkinghub.elsevier.com/retrieve/pii/S0034425722000074, doi:10.1016/j.rse.2022.112893.

Marrs, J.K., Reblin, J.S., Logan, B.A., Allen, D.W., Reinmann, A.B., Bombard, D.M., Tabachnik, D., Hutyra, L.R., 2020. Solar-Induced Fluorescence Does Not Track Photosynthetic Carbon Assimilation Following Induced Stomatal Closure. Geophysical Research Letters 47, e2020GL087956. URL: https://onlinelibrary.wiley.com/doi/abs/10.1029/2020GL087956, doi:10.1029/2020GL087956. _eprint: https://onlinelibrary.wiley.com/doi/pdf/10.1029/2020GL087956.

Martini, D., Sakowska, K., Wohlfahrt, G., Pacheco-Labrador, J., van der Tol, C., Porcar-Castell, A., Magney, T.S., Carrara, A., Colombo, R., El-Madany, T.S., Gonzalez-Cascon, R., Martín, M.P., Julitta, T., Moreno, G., Rascher, U., Reichstein, M., Rossini, M., Migliavacca, M., 2022. Heatwave breaks down the linearity between sun-induced fluorescence and gross primary production. New Phytologist 233, 2415–2428. URL: https://onlinelibrary.wiley.com/doi/abs/10.1111/nph.17920, doi:10.1111/nph.17920. _eprint: https://onlinelibrary.wiley.com/doi/pdf/10.1111/nph.17920.

Mathur, S., Agrawal, D., Jajoo, A., 2014. Photosynthesis: Response to high temperature stress. Journal of Photochemistry and Photobiology B: Biology 137, 116–126. URL: https://www.sciencedirect.com/science/article/pii/S1011134414000190, doi:10.1016/j.jphotobiol.2014.01.010.

Mauder, M., Foken, T., Aubinet, M., Ibrom, A., 2021. Eddy-Covariance Measurements, in: Foken, T. (Ed.), Springer Handbook of Atmospheric Measurements. Springer International Publishing, Cham. Springer Handbooks, pp. 1473–1504. URL: https://doi.org/10.1007/978-3-030-52171-4_55, doi:10.1007/978-3-030-52171-4_55.

Meier, U., 2018. Growth stages of mono- and dicotyledonous plants: BBCH Monograph. URL: https://www.openagrar.de/receive/openagrar_mods_00042351, doi:10.5073/20180906-074619.

Meroni, M., Rossini, M., Guanter, L., Alonso, L., Rascher, U., Colombo, R., Moreno, J., 2009. Remote sensing of solar-induced chlorophyll fluorescence: Review of methods and applications. Remote Sensing of Environment 113, 2037–2051. URL: https://linkinghub.elsevier.com/retrieve/pii/S003442570900162X, doi:10.1016/j.rse.2009.05.003.

Moene, A.F., Dam, J.C.v., 2014. Transport in the atmosphere-vegetation-soil continuum. Cambridge University Press, New York, NY.

Mohammed, G.H., Colombo, R., Middleton, E.M., Rascher, U., van der Tol, C., Nedbal, L., Goulas, Y., Pérez-Priego, O., Damm, A., Meroni, M., Joiner, J., Cogliati, S., Verhoef, W., Malenovský, Z., Gastellu-Etchegorry, J.P., Miller, J.R., Guanter, L., Moreno, J., Moya, I., Berry, J.A., Frankenberg, C., Zarco-Tejada, P.J., 2019. Remote sensing of solar-induced chlorophyll fluorescence (SIF) in vegetation: 50 years of progress. Remote Sensing of Environment 231, 111177. URL: https://www.sciencedirect.com/science/article/pii/S0034425719301816, doi:10.1016/j.rse.2019.04.030.

Moreno, J.F., Asner, G.P., Bach, H., Belenguer, T., Kneubühler, M., Schaepman, M.E., 2006. FLuorescence EXplorer (FLEX): an optimised payload to map vegetation photosynthesis from space URL: https://www.zora.uzh.ch/id/eprint/77951, doi:10.5167/UZH-77951. publisher: ARC Aerospace Research Central.

Gourlez de la Motte, L., Beauclaire, Q., Heinesch, B., Cuntz, M., Foltýnová, L., Šigut, L., Kowalska, N., Manca, G., Ballarin, I.G., Vincke, C., Roland, M., Ibrom, A., Lousteau, D., Siebicke, L., Neiryink, J., Longdoz, B., 2020. Non-stomatal processes reduce gross primary productivity in temperate forest ecosystems during severe edaphic drought. Phil. Trans. R. Soc. B 375, 20190527. URL: https://royalsocietypublishing.org/doi/10.1098/rstb.2019.0527, doi:10.1098/rstb.2019.0527.

Moya, I., Camenen, L., Evain, S., Goulas, Y., Cerovic, Z.G., Latouche, G., Flexas, J., Ounis, A., 2004. A new instrument for passive remote sensing: 1. Measurements of sunlight-induced chlorophyll fluorescence. Remote Sensing of Environment 91, 186–197. URL: https://www.sciencedirect.com/science/article/pii/S0034425704000756, doi:10.1016/j.rse.2004.02.012.

Paul-Limoges, E., Damm, A., Hueni, A., Liebisch, F., Eugster, W., Schaepman, M.E., Buchmann, N., 2018. Effect of environmental conditions on sun-induced fluorescence in a mixed forest and a cropland. Remote Sensing of Environment 219, 310–323. URL: https://www.sciencedirect.com/science/article/pii/S0034425718304735, doi:10.1016/j.rse.2018.10.018.

Perkins, S.E., Alexander, L.V., 2013. On the Measurement of Heat Waves. Journal of Climate 26, 4500–4517. URL: https://journals.ametsoc.org/view/journals/clim/26/13/jcli-d-12-00383.1.xml, doi:10.1175/JCLI-D-12-00383.1. publisher: American Meteorological Society Section: Journal of Climate.

Pierrat, Z., Magney, T., Parazoo, N.C., Grossmann, K., Bowling, D.R., Seibt, U., Johnson, B., Helgason, W., Barr, A., Bortnik, J., Norton, A., Maguire, A., Frankenberg, C., Stutz, J., 2022. Diurnal and Seasonal Dynamics of Solar-Induced Chlorophyll Fluorescence, Vegetation Indices, and Gross Primary Productivity in the Boreal Forest. Journal of Geophysical Research: Biogeosciences 127, e2021JG006588. URL: https://

onlinelibrary.wiley.com/doi/abs/10.1029/2021JG006588, doi:10.1029/2021JG006588. _eprint: https://onlinelibrary.wiley.com/doi/pdf/10.1029/2021JG006588.

Porcar-Castell, A., Malenovský, Z., Magney, T., Van Wittenberghe, S., Fernández-Marín, B., Maignan, F., Zhang, Y., Maseyk, K., Atherton, J., Albert, L.P., Robson, T.M., Zhao, F., Garcia-Plazaola, J.I., Ensminger, I., Rajewicz, P.A., Grebe, S., Tikkanen, M., Kellner, J.R., Ihalainen, J.A., Rascher, U., Logan, B., 2021. Chlorophyll a fluorescence illuminates a path connecting plant molecular biology to Earth-system science. Nat. Plants 7, 998–1009. URL: https://www.nature.com/articles/s41477-021-00980-4, doi:10.1038/s41477-021-00980-4.

Porcar-Castell, A., Tyystjärvi, E., Atherton, J., van der Tol, C., Flexas, J., Pfündel, E.E., Moreno, J., Frankenberg, C., Berry, J.A., 2014. Linking chlorophyll a fluorescence to photosynthesis for remote sensing applications: mechanisms and challenges. Journal of Experimental Botany 65, 4065–4095. URL: https://academic.oup.com/jxb/article-lookup/doi/10.1093/jxb/eru191, doi:10.1093/jxb/eru191.

Reed, D.W., 1969. Isolation and Composition of a Photosynthetic Reaction Center Complex from Rhodopseudomonas spheroides. Journal of Biological Chemistry 244, 4936–4941. URL: https://www.sciencedirect.com/science/article/pii/S0021925818942936, doi:10.1016/S0021-9258(18)94293-6.

Ritchie, R.J., 2008. Fitting light saturation curves measured using modulated fluorometry. Photosynth Res 96, 201–215. URL: https://doi.org/10.1007/s11120-008-9300-7, doi:10.1007/s11120-008-9300-7.

Rogers, A., Medlyn, B.E., Dukes, J.S., Bonan, G., von Caemmerer, S., Dietze, M.C., Kattge, J., Leakey, A.D.B., Mercado, L.M., Niinemets, U., Prentice, I.C., Serbin, S.P., Sitch, S., Way, D.A., Zaehle, S., 2017. A roadmap for improving the representation of photosynthesis in Earth system models. New Phytologist 213, 22–42. URL: https://onlinelibrary.wiley.com/doi/abs/10.1111/nph.14283, doi:10.1111/nph.14283. _eprint: https://onlinelibrary.wiley.com/doi/pdf/10.1111/nph.14283.

Sage, R.F., Kubien, D.S., 2007. The temperature response of C3 and C4 photosynthesis. Plant, Cell & Environment 30, 1086–1106. URL: https://onlinelibrary.wiley.com/doi/abs/10.1111/j.1365-3040.2007.01682.x, doi:10.1111/j.1365-3040.2007.01682.x. _eprint: https://onlinelibrary.wiley.com/doi/pdf/10.1111/j.1365-3040.2007.01682.x.

Schmidhuber, J., Tubiello, F.N., 2007. Global food security under climate change. Proceedings of the National Academy of Sciences 104, 19703–19708. URL: https://www.pnas.org/doi/abs/10.1073/pnas.0701976104, doi:10.1073/pnas.0701976104. publisher: Proceedings of the National Academy of Sciences.

Serôdio, J., Lavaud, J., 2011. A model for describing the light response of the nonphotochemical quenching of chlorophyll fluorescence. Photosynth Res 108, 61–76. URL: https://doi.org/10.1007/s11120-011-9654-0, doi:10.1007/s11120-011-9654-0.

Sharkey, T.D., Bernacchi, C.J., Farquhar, G.D., Singsaas, E.L., 2007. Fitting photosynthetic carbon dioxide response curves for C3 leaves. Plant, Cell & Environment 30, 1035–1040. URL: https://onlinelibrary.wiley.com/doi/abs/10.1111/j.1365-3040.2007.01710.x, doi:10.1111/j.1365-3040.2007.01710.x. _eprint: https://onlinelibrary.wiley.com/doi/pdf/10.1111/j.1365-3040.2007.01710.x.

Shen, Q., Lin, J., Yang, J., Zhao, W., Wu, J., 2022. Exploring the potential of spatially downscaled solar-induced chlorophyll fluorescence to monitor drought effects on gross primary

production in winter wheat. IEEE Journal of Selected Topics in Applied Earth Observations and Remote Sensing , 1–1doi:10.1109/JSTARS.2022.3148393. conference Name: IEEE Journal of Selected Topics in Applied Earth Observations and Remote Sensing.

Shewry, P.R., 2009. Wheat. Journal of Experimental Botany 60, 1537–1553. URL: https://doi.org/10.1093/jxb/erp058, doi:10.1093/jxb/erp058.

Statbel, 2022. Les superficies de pommes de terre et de maïs grain sont en forte baisse; le froment d'hiver et l'épeautre augmentent | Statbel. URL: https://statbel.fgov.be/fr/nouvelles/les-superficies-de-pommes-de-terre-et-de-mais-grain-sont-en-forte-baisse-le-froment.

Taiz, L., Zeiger, E., Møller, I.M., Murphy, A.S., 2015. Plant physiology and development. Sixth edition ed., Sinauer Associates, Inc., Publishers, Sunderland, Massachusetts.

van der Tol, C., Berry, J.A., Campbell, P.K.E., Rascher, U., 2014. Models of fluorescence and photosynthesis for interpreting measurements of solar-induced chlorophyll fluorescence. Journal of Geophysical Research: Biogeosciences 119, 2312–2327. URL: https://onlinelibrary.wiley.com/doi/abs/10.1002/2014JG002713, doi:10.1002/2014JG002713. _eprint: https://onlinelibrary.wiley.com/doi/pdf/10.1002/2014JG002713.

van der Tol, C., Verhoef, W., Rosema, A., 2009. A model for chlorophyll fluorescence and photosynthesis at leaf scale. Agricultural and Forest Meteorology 149, 96–105. URL: https://www.sciencedirect.com/science/article/pii/S0168192308002049, doi:10.1016/j.agrformet.2008.07.007.

Turner, D.P., Urbanski, S., Bremer, D., Wofsy, S.C., Meyers, T., Gower, S.T., Gregory, M., 2003. A cross-biome comparison of daily light use efficiency for gross primary production. Global Change Biology 9, 383–395. URL: https://onlinelibrary.wiley.com/doi/abs/10.1046/j.1365-2486.2003.00573.x, doi:10.1046/j.1365-2486.2003.00573.x. _eprint: https://onlinelibrary.wiley.com/doi/pdf/10.1046/j.1365-2486.2003.00573.x.

UG, J.H.D., 2022. The Fluorescence Box, a hyperspectral instrument for unattended observation of sun-induced chlorophyll fluorescence and reflectance. Manual for Installation and Operation.

Urban, J., Ingwers, M., McGuire, M.A., Teskey, R.O., 2017. Stomatal conductance increases with rising temperature. Plant Signaling & Behavior 12, e1356534. URL: https://doi.org/10.1080/15592324.2017.1356534, doi:10.1080/15592324.2017.1356534. publisher: Taylor & Francis _eprint: https://doi.org/10.1080/15592324.2017.1356534.

Urban, O., Hlaváčová, M., Klem, K., Novotná, K., Rapantová, B., Smutná, P., Horáková, V., Hlavinka, P., Škarpa, P., Trnka, M., 2018. Combined effects of drought and high temperature on photosynthetic characteristics in four winter wheat genotypes. Field Crops Research 223, 137–149. URL: https://www.sciencedirect.com/science/article/pii/S0378429017314727, doi:10.1016/j.fcr.2018.02.029.

Weston, D.J., Bauerle, W.L., 2007. Inhibition and acclimation of C3 photosynthesis to moderate heat: a perspective from thermally contrasting genotypes of Acer rubrum (red maple). Tree Physiology 27, 1083–1092. URL: https://doi.org/10.1093/treephys/27.8.1083, doi:10.1093/treephys/27.8.1083.

Wohlfahrt, G., Gerdel, K., Migliavacca, M., Rotenberg, E., Tatarinov, F., Müller, J., Hammerle, A., Julitta, T., Spielmann, F.M., Yakir, D., 2018. Sun-induced fluorescence and gross primary productivity during a heat wave. Sci Rep 8, 14169. URL: https://www.nature.com/articles/s41598-018-32602-z, doi:10.1038/s41598-018-32602-z. number: 1 Publisher: Nature Publishing Group.

Wohlfahrt, G., Klumpp, K., Soussana, J.F., 2012. Eddy Covariance Measurements over Grasslands, in: Aubinet, M., Vesala, T., Papale, D. (Eds.), Eddy Covariance: A Practical Guide to Measurement and Data Analysis. Springer Netherlands, Dordrecht. Springer Atmospheric Sciences, pp. 333–344. URL: https://doi.org/10.1007/978-94-007-2351-1_13, doi:10.1007/978-94-007-2351-1_13.

Wutzler, T., Lucas-Moffat, A., Migliavacca, M., Knauer, J., Sickel, K., Šigut, L., Menzer, O., Reichstein, M., 2018. Basic and extensible post-processing of eddy covariance flux data with REddyProc. Biogeosciences 15, 5015–5030. URL: https://bg.copernicus.org/articles/15/5015/2018/, doi:10.5194/bg-15-5015-2018. publisher: Copernicus GmbH.

Yamamoto, H.Y., Bugos, R.C., David Hieber, A., 1999. Biochemistry and Molecular Biology of the Xanthophyll Cycle, in: Frank, H.A., Young, A.J., Britton, G., Cogdell, R.J. (Eds.), The Photochemistry of Carotenoids. Springer Netherlands, Dordrecht. Advances in Photosynthesis and Respiration, pp. 293–303. URL: https://doi.org/10.1007/0-306-48209-6_16, doi:10.1007/0-306-48209-6-16.

Yamasaki, T., Yamakawa, T., Yamane, Y., Koike, H., Satoh, K., Katoh, S., 2002. Temperature Acclimation of Photosynthesis and Related Changes in Photosystem II Electron Transport in Winter Wheat. Plant Physiology 128, 1087–1097. URL: https://doi.org/10.1104/pp.010919, doi:10.1104/pp.010919.

Yamori, W., Hikosaka, K., Way, D.A., 2014. Temperature response of photosynthesis in C3, C4, and CAM plants: temperature acclimation and temperature adaptation. Photosynth Res 119, 101–117. URL: https://doi.org/10.1007/s11120-013-9874-6, doi:10.1007/s11120-013-9874-6.

Yang, K., Ryu, Y., Dechant, B., Berry, J.A., Hwang, Y., Jiang, C., Kang, M., Kim, J., Kimm, H., Kornfeld, A., Yang, X., 2018. Sun-induced chlorophyll fluorescence is more strongly related to absorbed light than to photosynthesis at half-hourly resolution in a rice paddy. Remote Sensing of Environment 216, 658–673. URL: https://www.sciencedirect.com/science/article/pii/S0034425718303353, doi:10.1016/j.rse.2018.07.008.

Yang, X., Tang, J., Mustard, J.F., Lee, J.E., Rossini, M., Joiner, J., Munger, J.W., Kornfeld, A., Richardson, A.D., 2015. Solar-induced chlorophyll fluorescence that correlates with canopy photosynthesis on diurnal and seasonal scales in a temperate deciduous forest. Geophysical Research Letters 42, 2977–2987. URL: https://onlinelibrary.wiley.com/doi/abs/10.1002/2015GL063201, doi:10.1002/2015GL063201. _eprint: https://onlinelibrary.wiley.com/doi/pdf/10.1002/2015GL063201.

Zha, T.S., Wu, Y.J., Jia, X., Zhang, M.Y., Bai, Y.J., Liu, P., Ma, J.Y., Bourque, C.P.A., Peltola, H., 2017. Diurnal response of effective quantum yield of PSII photochemistry to irradiance as an indicator of photosynthetic acclimation to stressed environments revealed in a xerophytic species. Ecological Indicators 74, 191–197. URL: https://www.sciencedirect.com/science/article/pii/S1470160X16306641, doi:10.1016/j.ecolind.2016.11.027.

Zhang, Y., Guanter, L., Berry, J.A., van der Tol, C., Yang, X., Tang, J., Zhang, F., 2016. Model-based analysis of the relationship between sun-induced chlorophyll fluorescence and gross primary production for remote sensing applications. Remote Sensing of Environment 187, 145–155. URL: https://linkinghub.elsevier.com/retrieve/pii/S0034425716303893, doi:10.1016/j.rse.2016.10.016.

Zhao, F., Guo, Y., Verhoef, W., Gu, X., Liu, L., Yang, G., 2014. A Method to Reconstruct the Solar-Induced Canopy Fluorescence Spectrum from Hyperspectral Measurements. Remote Sensing 6, 10171–10192. URL: https://www.mdpi.com/2072-4292/6/10/10171,

doi:10.3390/rs61010171. number: 10 Publisher: Multidisciplinary Digital Publishing Institute.

Zivcak, M., Brestic, M., Kalaji, H.M., Govindjee, 2014. Photosynthetic responses of sun- and shade-grown barley leaves to high light: is the lower PSII connectivity in shade leaves associated with protection against excess of light? Photosynth Res 119, 339–354. URL: https://doi.org/10.1007/s11120-014-9969-8, doi:10.1007/s11120-014-9969-8.

# Appendix A

# Appendix

## A.1 Band conversion ratio

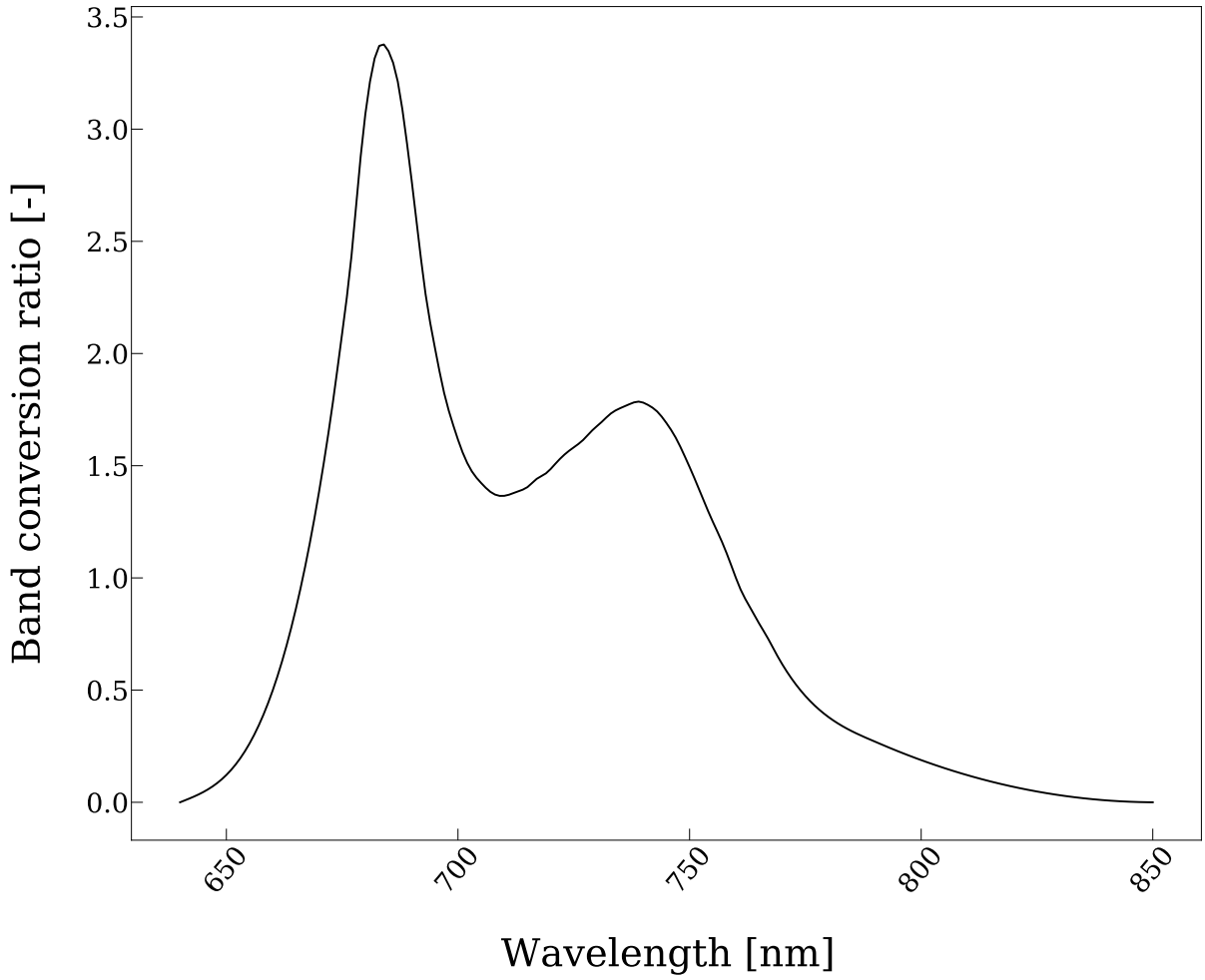


Figure A.1: Band conversion ratio evolution over the fluorescence emission band : from 640 to 850 nm.

## A.2 Daily variations

Evolution of the hourly mean of measured GPP ($GPP_{EC}$), broadband SIF emitted by all the leaves of the canopy, related to PSII ($SIF_{TOT\_FULL\_PSII}$) and incoming photosynthetically active radiation (PAR). Hourly means have been computed from the whole data set from day of year (DOY) 51 to 181. PCC is the Pearson correlation coefficient between hourly mean values of $GPP_{EC}$ and $SIF_{TOT\_FULL\_PSII}$. Only values accounting for incoming irradiance higher than 20 $\mu molPhoton.m^{-2}.s^{-1}$ and non-rainy days are shown.

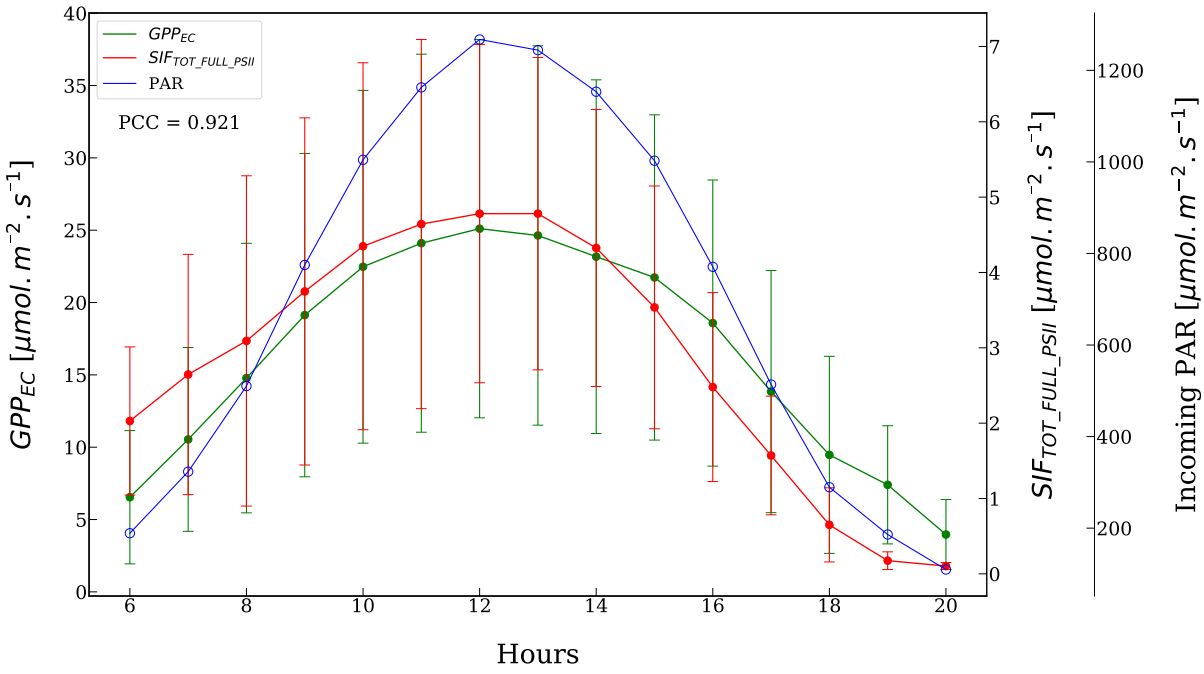


Figure A.2: Daily variations of tower-based measured GPP, total broadband SIF emitted from PSII, and incoming PAR from DOY 51 to 181.

## A.3 Non-photochemical quenching modelling

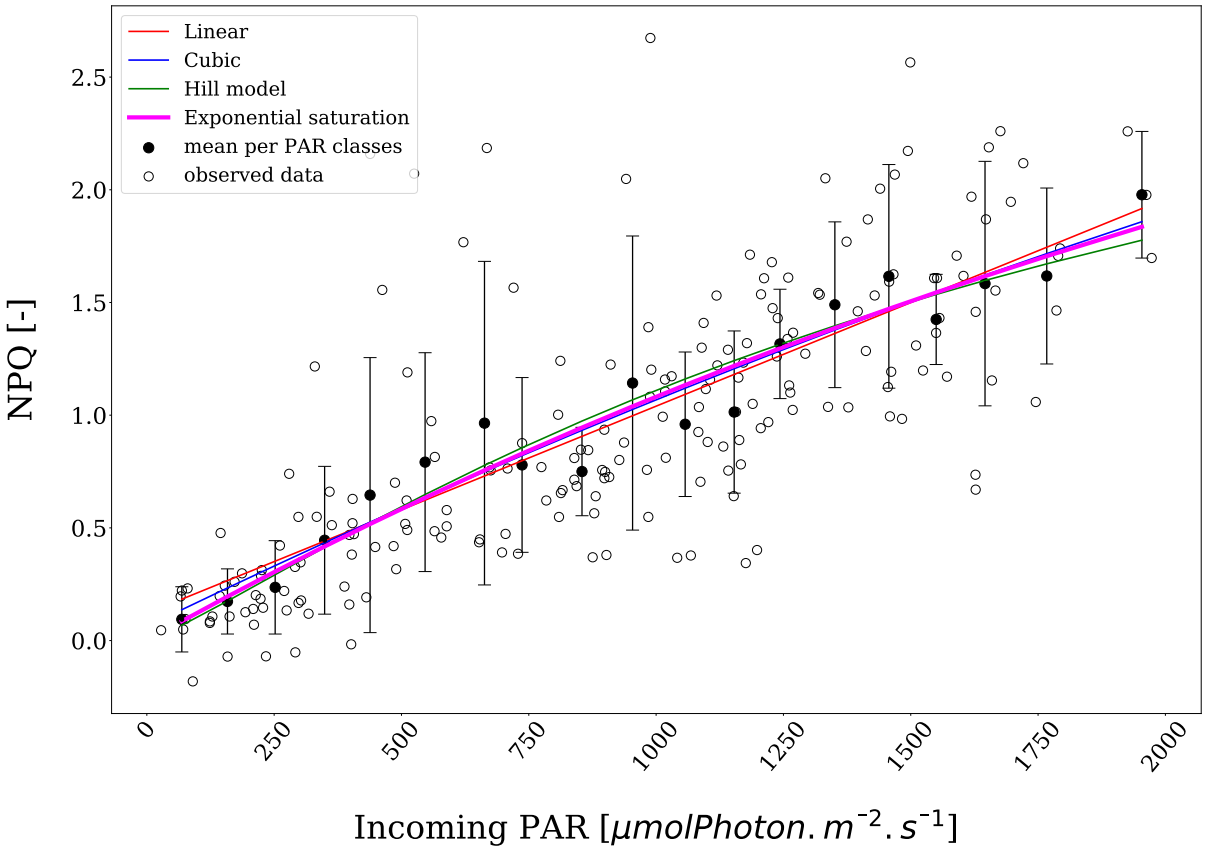


Figure A.3: Evolution of NPQ with the incoming PAR. Empty dots represent punctual measurements done with the LI-6400XT Portable Photosynthesis System and black dots are NPQ averages per PAR classes, with twelve classes of 100 $\mu molPhoton.m^{-2}.s^{-1}$ width. Linear and cubic models are shown as well as the Hill model proposed by Serôdio and Lavaud (2011) and the exponential saturation model proposed by Ritchie (2008).

## A.4 Quality assessment of the parametrization of $q_L$ and NPQ from PAR

Each model has been compared to an intercept-model only (with the mean of observed data as parameter) thanks to a F-test by considering a 95 % confidence level. $\sigma$ is the standard deviation of each fitted parameter.

Table A.1: Parameters assessing the quality of the parametrization of NPQ and $q_L$ from PAR.

| Model | Parameter | value | $\sigma$ | $R^2$ | AICc | RMSE [-] | p-value |
|---|---|---|---|---|---|---|---|
| **NPQ** | | | | | | | |
| **Linear** | slope<br>intercept | 9.194<br>0.121 | 0.000<br>0.061 | 0.943 | -71.217 | 0.126 | $< 0.001$ |
| **Cubic** | a<br>b<br>c | 0.000<br>0.001<br>0.062 | 0.000<br>0.000<br>0.093 | 0.946 | -68.788 | 0.123 | $< 0.001$ |
| **Hill model** | n<br>NPQmax<br>E50 | 1.177<br>3.553<br>1953.880 | 0.340<br>2.196<br>6.528 | 0.940 | -67.025 | 0.129 | $< 0.001$ |
| **Exponential saturation** | NPQmax<br>k | 3.945<br>0.000 | 1.488<br>0.000 | 0.945 | -71.839 | 0.124 | $< 0.001$ |
| $q_L$ | | | | | | | |
| **Linear** | slope<br>intercept | 0.000<br>0.545 | 0.000<br>0.012 | 0.790 | -133.502 | 0.024 | $< 0.001$ |
| **Cubic** | a<br>b<br>c | 0.000<br>0.000<br>0.570 | 0.000<br>0.000<br>0.016 | 0.833 | -134.586 | 0.022 | $< 0.001$ |
| **Power Law** | amplitude<br>exponent | 0.959<br>-0.111 | 0.075<br>0.012 | 0.820 | -137.843 | 0.023 | $< 0.001$ |
| **Chang model** | amplitude<br>exponent<br>constant | 0.197<br>-0.001<br>0.389 | 0.023<br>0.001<br>0.028 | 0.848 | -136.419 | 0.021 | $< 0.001$ |

## A.5 Temporal evolution of $f_{PSII}$

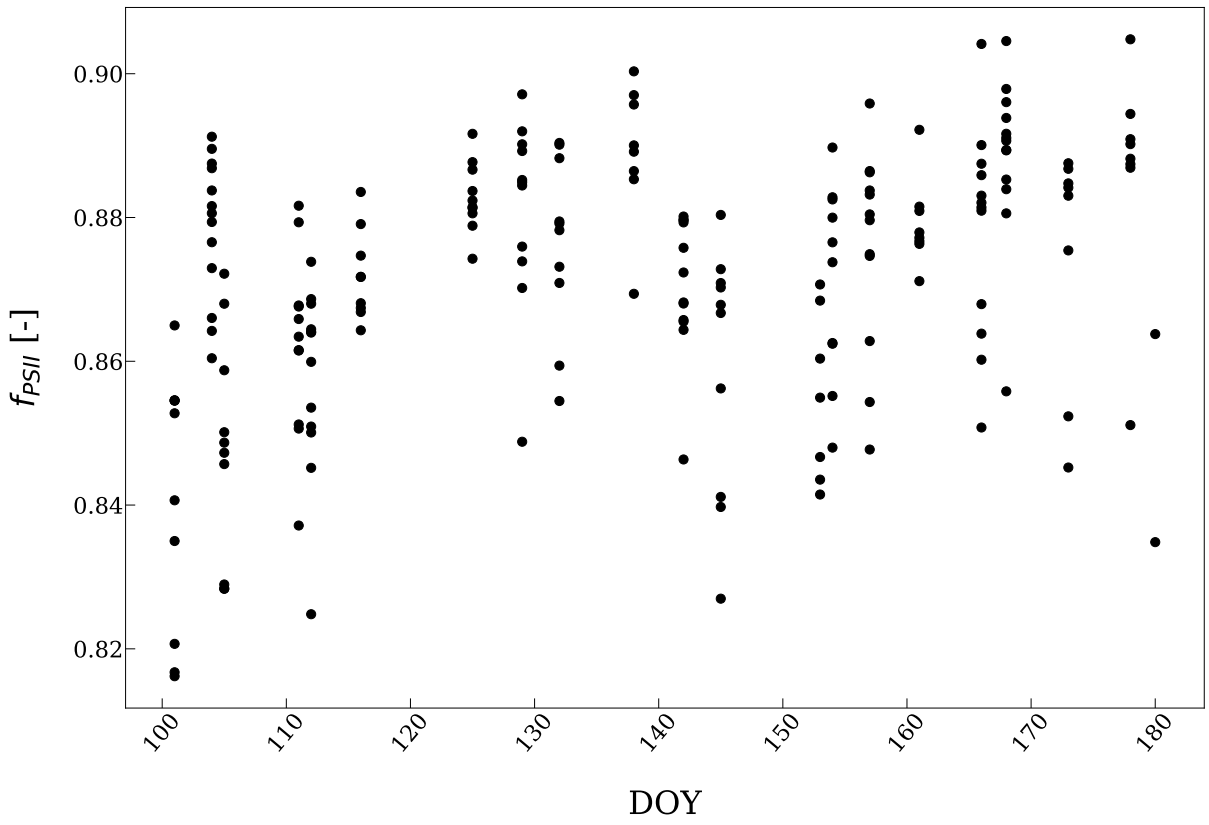


Figure A.4: Temporal evolution of the coefficient $f_{PSII}$, deduced from manual fluorescence measurements (Equation 2.12), from day of year (DOY) 101 to 180.

## A.6 Temporal evolution of narrowband SIF measured at the top of the canopy

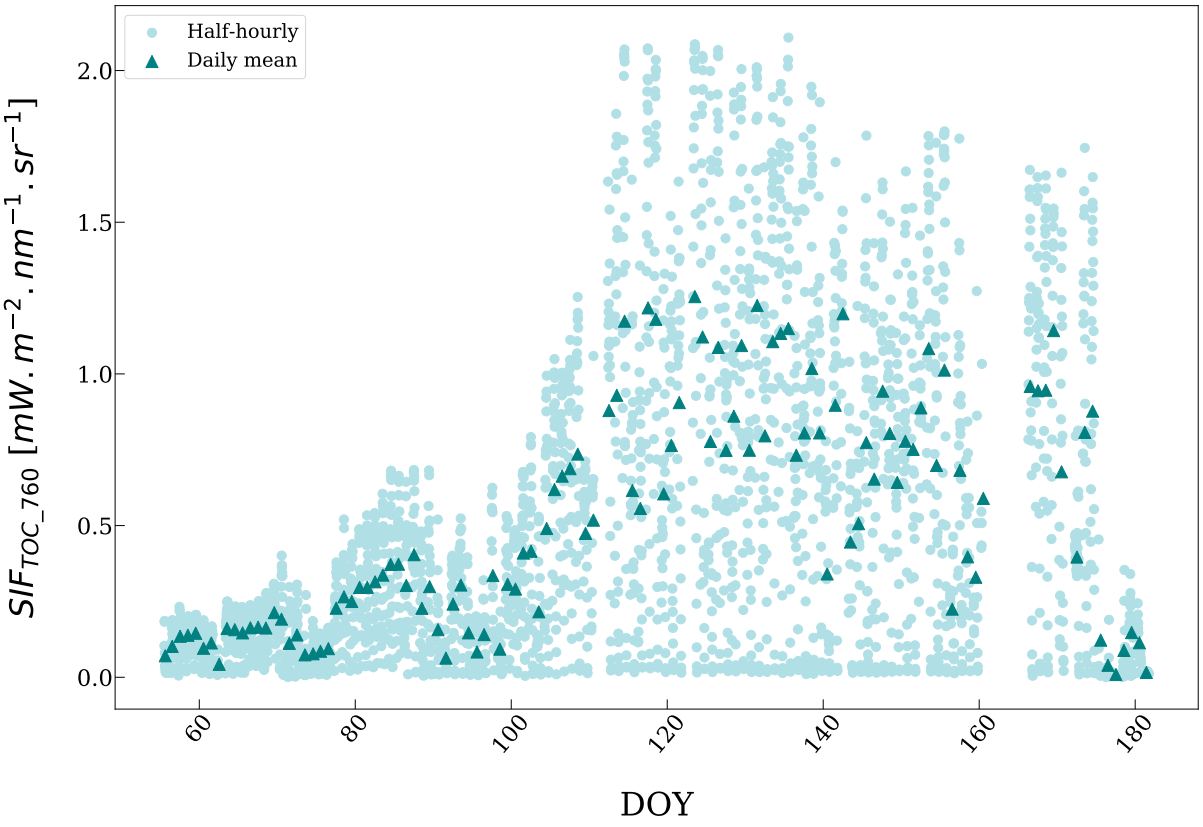


Figure A.5: Evolution of the measured SIF (760 nm) at the top of the canopy ($SIF_{TOC\_760}$) from day of year (DOY) 51 to 181. Light blue dots account for half-hourly observations while dark blue triangles represent daily means.